공학박사 학위논문

Hetero Structured Single Wall Carbon NanoTubes for Solution-Processed Field Effect Transistors

이종구조 단일벽 탄소나노튜브를 적용한
용액공정 전계효과 트랜지스터

2018년 2월

서울대학교 대학원
재료공학부
박 노 활

Hetero Structured
Single Wall Carbon NanoTubes
for Solution-Processed
Field Effect Transistors

지도 교수 김 장 주

이 논문을 공학박사 학위 논문으로 제출함

2018년 2월

서울대학교 대학원

재료공학부

박 노 활

박노활의 공학박사 학위논문을 인준함

2018 년 2월

위 원 장 _____ 윤 재 륜 _____ (인)

부위원장 _____ 김 장 주 _____ (인)

위 원 _____ 서 용 석 _____ (인)

위 원 _____ 장 지 영 _____ (인)

위 원 _____ 노 용 영 _____ (인)

Abstract

Hetero Structured Single Wall Carbon NanoTubes for Solution-Processed Field Effect Transistors

Noh-Hwal Park
Department of Materials Science and Engineering
The Graduate School
Seoul National University

In recent years, the demand for flexible/stretchable devices for the rapid spread of mobile devices such as smartphones and wearable devices have increased. The semiconductor layer for the stretchable devices requires high mechanical properties together with excellent charge carrier mobility and a random network structure. Also a solution process is required for a large-area and low cost application. Single wall carbon nanotubes (SWNT) are one of the suitable materials for stretchable devices because they are solutions processed, have random network structure when they form films, exhibit high carrier mobility and excellent mechanical properties. However, they have both metallic and semi-conductivity properties in the synthesis,

so it is necessary to sort off only the semiconducting properties from the SWNTs. There have been several ways to separate this mixture, but they usually result in low purity and yield. We tried to solve this issue.

In Chapter 1, we will introduce basic transistors knowledge such as transistor's history, the operating principles, characteristic parameters, and type of tfts. Also we will introduce basic SWNT knowledge include Carbon allotropes, electric band structure of SWNT, and synthesis method of single wall carbon nanotubes.

In Chapter 2, we sort off high-purity semiconducting single-walled carbon nanotubes (s-SWNT) by polymer wrapping method. We demonstrate the selection of s-SWNTs in SWNTs grown by the high pressure carbon mono oxide (HiPCO) process using poly-9,9-di-n-octyl-fluorenyl-2,7-diyl (PFO) and poly (3-dodecylthiophene-2, 5-diyl) (P3DDT), the wrapping polymer was used poly (9, 9-di-n-dodecylfluorene) (PFDD) for plasma discharge process (PD).We analyzed the purity, concentration and random network surface with Ultraviolet-visible spectroscopy, Raman spectroscopy, Atomic force microscope, Field emission scanning electron microscopy, and Transmission electron microscopy. Based on the UV-vis-NIR absorption spectra, Raman spectroscopy, and electrical parameter of the resulting devices, the purity of s-SWNT in P3DDT-HiPCO is estimated to be > 99% and the purity of s-SWNT in PFDD-PD is estimated 98-99%.

In Chapter 3, we will talk about method, we fabricated transistors by using high purity s-SWNTs ink. The P3DDT-HiPCO transistors show high on/off ratio, but

low mobility, while the PFDD-PD exhibit high mobility with high off current level. A hetero structure system was adopted to solve these challenges. And by this way, we achieved a hole mobility of 7 cm^2/VS and on/off ratio of 1.5×10^7. And $FeCl_3$-doping hetero structure system, we achieved a hole mobility of over than 100 cm^2/VS (V_d = -20V) and on/off ratio of 10^6 (V_d=-5V).

Keyword: Single Wall Carbon NanoTubes, Thin film transistor, Stretchable device, Polymer wrapping method, High pressure carbon monoxide, Plasma discharge carbon nanotube, Solution process, Doping

Student Number: 2007 - 30804

Contents

List of Figures

Chapter 1. Introduction

We are now living in a world of advanced display technology flood including TV, PC monitors, tablet PC, mobile phones, smart watches, virtual reality (VR), etc. Since the invention of the first cathode ray tube by Karl Ferdinad in 1897, the display industry has expanded rapidly. As the display technology advances, progress in the performance of transistors is also required. Thin film transistors (TFTs) have lower performance than single crystalline silicon FETs, but are capable of large area processes such as to be deposited on glass substrates. In particular, as displays have developed from CRT to FPD (mainly LCD), TFTs (a-Si: H TFT) have been applied as the key element (switching element for on and off state) for pixel control. Higher performance TFTs are needed due to higher display specifications (high resolution, large area, high frequency) required in the market.

In recent years, the demand for flexible/stretchable devices for the rapid spread of mobile devices. Organic electronics such as organic light emitting diode (OLED), organic photovoltaic (OPV) and organic thin film transistors (OTFTs) been researched due to their promising potential for application in low-cost, large-area and flexible device[1, 2] as shown in Fig1.1. In order to apply TFTs in active-matrix OLEDs, the minimum requirements for the field-effect mobility and the on/off ratio are 5–10 cm^2 V^{-1} s^{-1}[3] and 10^6,respectively, to avoid unnecessary power consumption and to guarantee maximum brightness contrast for each pixel[4]. OTFTs, amorphous oxide TFT and Carbon nanotube TFTs (CNTFET) are strong candidates.

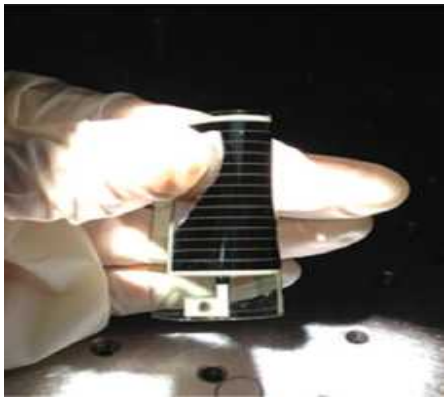

OPVs

OLEDs

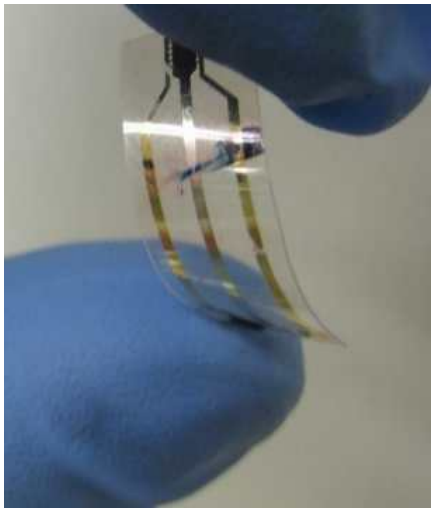

OTFTs

Fig. 1. 1 Flexible organic electronic devices: organic photovoltaic (OPVs), organic light emitting diodes (OLEDs), and organic thin film transistors (OTFTs)

Thin film transistor

Weimer suggested and evolved the concept of forming a transistor by means of semiconductor thin film fabrication from cadmium sulfide in 1962 [5]. LeComber showed a TFT based on amorphous silicon (a-Si: H) that was formed the thin film at a relatively lower temperature. in 1975[6]. Thereafter, in the 1980s, Kudo et al reported OTFTs on glass and plastic foil[7]. Due to the low mobility of the organic active layers, OTFTs cannot compete the performance of field-effect transistors based on single-crystalline inorganic semi-conductors which have nobilities about several orders of magnitude higher[8]. OTFTs are not proper for use in applications demanding high switching speeds. However, the processing characteristics and shown performance of OTFTs indicate that they can be competitive for existing or novel thin-film-transistor applications demanding large-area coverage, structural flexibility, low-temperature processing, and, especially, low cost. Heretofore, tremendous efforts have been made to intensify the performance of OTFTs. Nomuat et al demonstrate flexible amorphous In-Ga-Zn-O TFTs in 2004[9]. The advantage of oxide semiconductor materials is that they use conventional semiconducting method.

Operating principles

A TFT is formed with a layered structural design consisting of a semiconductor, an insulator, and three electrode including the source, drain, and gate. Source

terminal can act as the charge injection electrode, drain terminal can act as the charge extraction electrode, and gate electrode controls the conductivity of the channel. Fig1.2 shows the principles of operation regimes of the field-effect transistors and corresponding current voltage characteristics. TFTs operate as voltage-controlled current source. When bias is applied to the gate electrode, the channel is formed near the semiconductor/insulator interface. Upon applying a suitable drain to source potential, carriers move through the active layer. When the drain voltage increases substantially and approaches VG values the channel becomes pinch of ($V_{DS}=V_G-V_{TH}$) the current saturates due to form depletion region.

Characteristic parameters

There are several electrical parameters including field dependent mobility (μ), threshold voltage (V_{th}), on/off ratio (I_{On}/I_{Off}), and sub-threshold slope (SS) for transistor. These parameters are affected by device geometry, active layer material, structural dimensions, and morphology of the semiconductor. Demand conditions for a superior transistor are high mobility, low threshold voltage, large on/off ratio, and sharp sub-threshold slope.

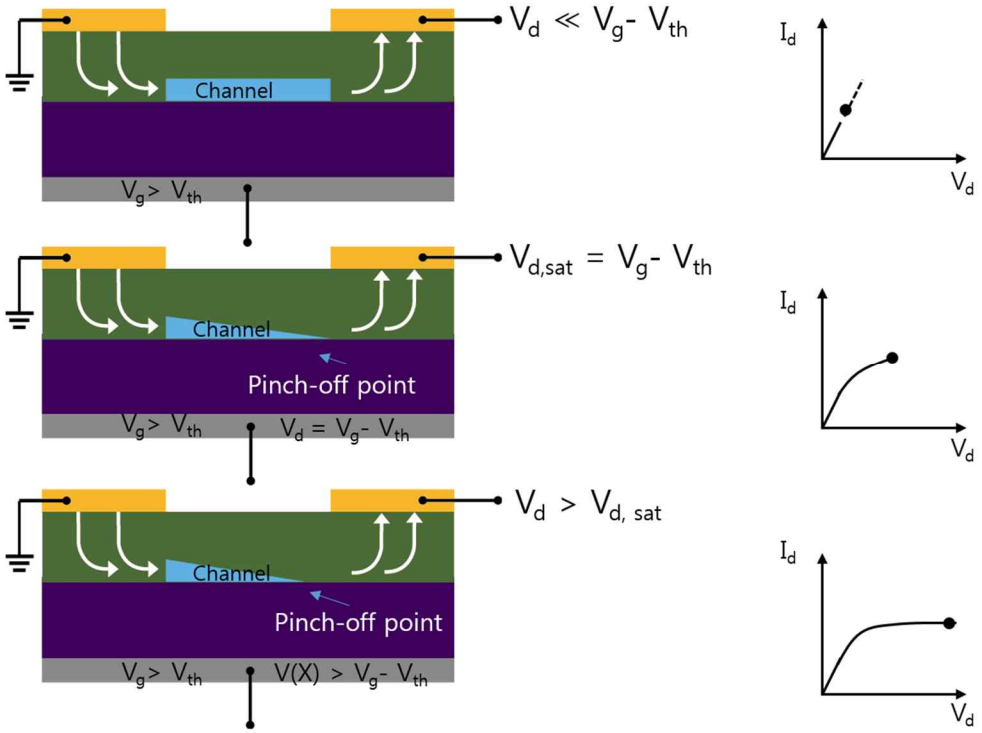

Fig. 1. 2 The principles of operating regimes of field-effect transistors and corresponding current voltage characteristics[10].

The mobility of a transistor is characterized as the average charge carrier drift velocity per unit electric field ($cm^2V^{-1}s^{-1}$). It is a crucial parameter in determining the processing speed of a device. High mobility is an important factor in obtaining a large on-current that is essentially required for many applications. Threshold voltage is the minimum gate voltage required for accumulating the charge carriers at the semiconductor / dielectric interface to form a conducting path between the source and the drain. It decides the switching behavior of a device and shows an intensive dependence on the channel length, doping concentration, dielectric constant of the insulator, and the thicknesses of the active and dielectric layers[11]. On/off ratio is the ratio of the current in accumulation mode to the current in the depletion mode. There are several key factors including a high dielectric constant of the insulator, a thin layer of a semiconductor, and low doping concentration in creating a large difference between the on and off current[12]. A sub-threshold slope (SS) is a ratio of change in the gate bias to the change in the drain current in logarithmic scale. SS is a key parameter that determines an efficient switching properties of the device. It is a measure of impurity concentration, interface state, and trap density that influence the switching properties. The quality of active layer affects this slope substantially[13]. SS of a TFT is closely related to the mobility enhancement for carrier hopping. Lower trap density show in a sharp slope which leads to better switching performance[14]. Fig 1.3 shows a typical plot of output and transfer curves. In p-type semiconductor, when a negative bias is applied, the accumulation mode was formed on the active / dielectric layer interface.

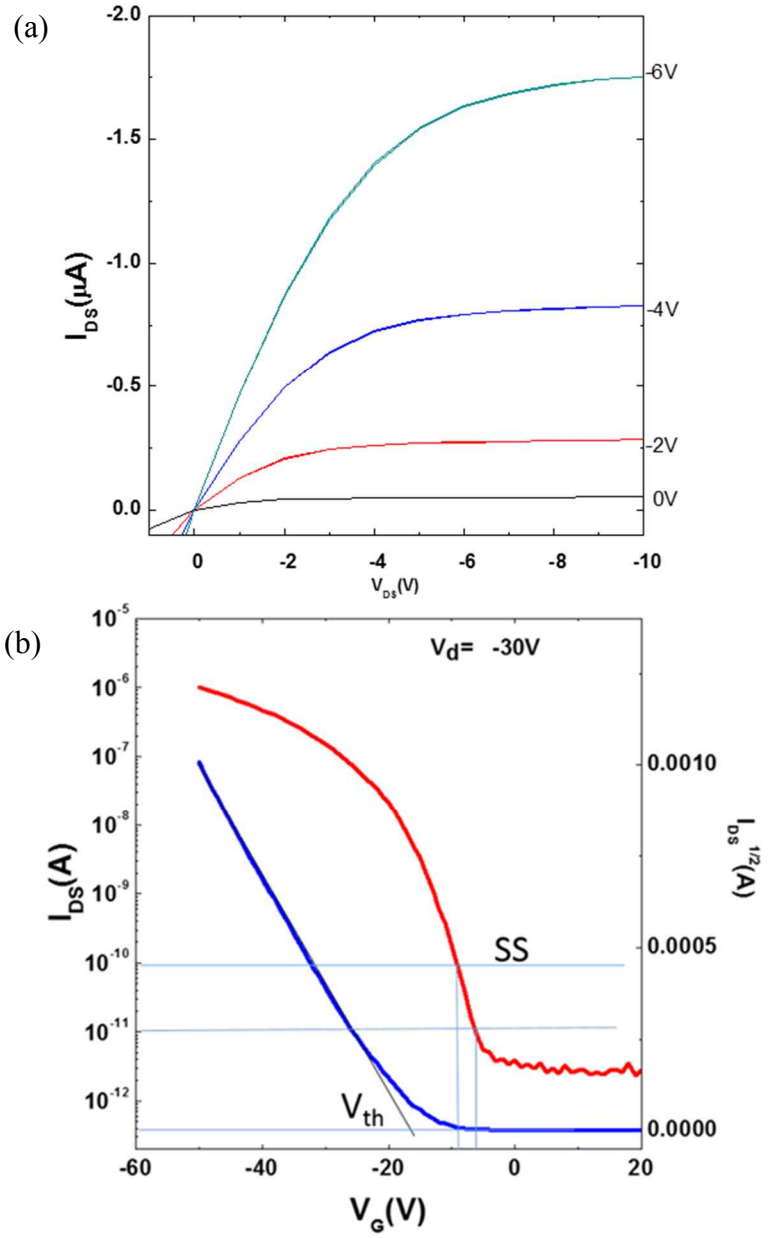

Fig. 1. 3 The output (a) and transfer curves (b) of FET

At low V_D (linear regime), I_D increase linearity with V_D and is determined from the following eq:

$$I_D = \frac{WC_i}{L}\mu\left((V_G - V_{th})V_D - \frac{V_D^2}{2}\right)$$

where L is the channel length, W is the channel width, C_i is the capacitance per unit area of the insulating layer, V_{th} is the threshold voltage, and μ is the field effect mobility, respectively.

In the linear regime with VDS << VG, eq can be simplified to

$$I_D = \frac{WC_i}{L}\mu(V_G - V_{th})V_D$$

The linear mobility can be calculated from the trans-conductance,

$$g_m = \left(\frac{\partial I_D}{\partial V_G}\right)_{V_D=const} = \frac{W\ C_i}{L}\mu V_D$$

by plotting I_D versus V_G at a constant low V_D and equating the value of the slope of this plot to g_m.

For saturation regime (V_D >V_G), the I_D does not increase and saturates due to the pinch off effect. The I_D is calculated as

$$I_D = \frac{W\ C_i}{2L}\mu(V_G - V_T)^2$$

The saturation mobility can be calculated from the slope of the plot of $|I_D|^{1/2}$ versus V_G.

Type of TFTs

Different material structures induce different mobility. Amorphous TFTs use amorphous silicon as the material of active layer. Amorphous silicon TFTs using hit wire chemical vapor deposition (HWCVD) method reported field effect mobility of 4.7$cm^2V^{-1}s^{-1}$[15] but they have large leakage current upon exposure to light and they are unstable under stress conditions[16]. Oxide TFTs use oxide as the material of the active layer. ZnO is a wide band gap semiconductor, its mobility was higher than amorphous semiconductors[17], it can be used conventional semiconducting method but it has low electrical stability[18]. Fig 1.4 show mobility development of oxide TFTs[19].

The performance of an OTFTs depend on the material of the active layer, insulator and electrodes. Organic semiconductors are classified into the conducting polymers and small molecules. Pentacene is the most widely used p-type organic semiconductor due to high hole mobility, good chemical stability, orderly formation in thin film structure, and good interface with Au source electrode[20], but operating voltage is too high (V_d = 100V).

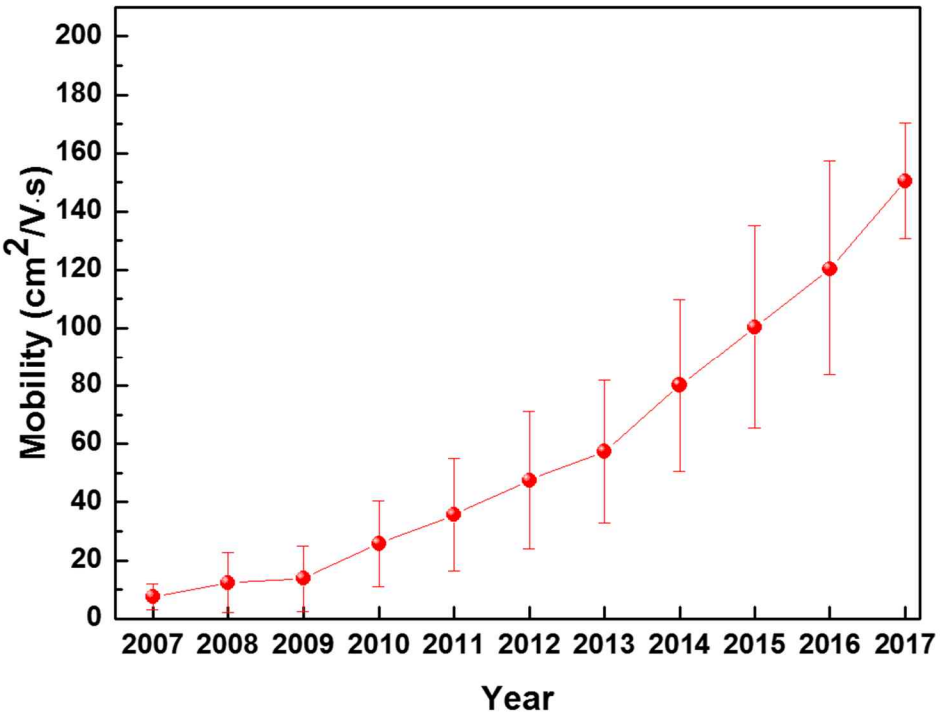

Fig. 1. 4 Mobility progress of oxide thin film transistors[19].

A single-crystal organic transistors have many advantages including of high mobility, reproducibility due to substantial reduction in the structural disorder of the OSC. They show an intensive dependence on the temperature due to weak intermolecular overlapping of the electronic orbitals[21]. P3HT shows low mobility but is, nevertheless, suitable for fabricating through solution process[22]. Fig 1.5 and Fig 1.6 shows chemical structures of different p-type and n-type organic materials. Many researcher groups have tried chemical doping[23, 24], rational molecular design [25] and synthesis for active layer and dielectric layer in order to improve their performance[26, 27]. Especially, Z.Bao et al demonstrated OTFTs hole mobility up to 43 $cm^2 V^{-1} s^{-1}$ (25 $cm^2 V^{-1} s^{-1}$ on average) in 2013. They aligned meta-stable structure of 2,7-dioctyl[1]benzothieno[3,2b][1]-benzothiophene (C8-BTBT) and polystyrene by using an off-centre spin-coating method[28]. Fig 1.7 shows mobility growth for organic semiconductors.

CNTFETs use semiconducting single wall carbon nanotubes (s-SWNT) as the material of the active layer. Dekker et al demonstrated the first CNTTFT in 1998 [29]. For individual nanotubes TFT, they show the high charge carrier nobilities and their excellent electrostatic properties sub 10 nm gate length transistors[30]. For flexible/ stretchable devices, SWNT TFTs exhibit random network via using solution process fabrication. The density of nanotubes are higher than the percolation limit (>10 SWNT/μm) to ensure high on current in a field-effect transistor[31].

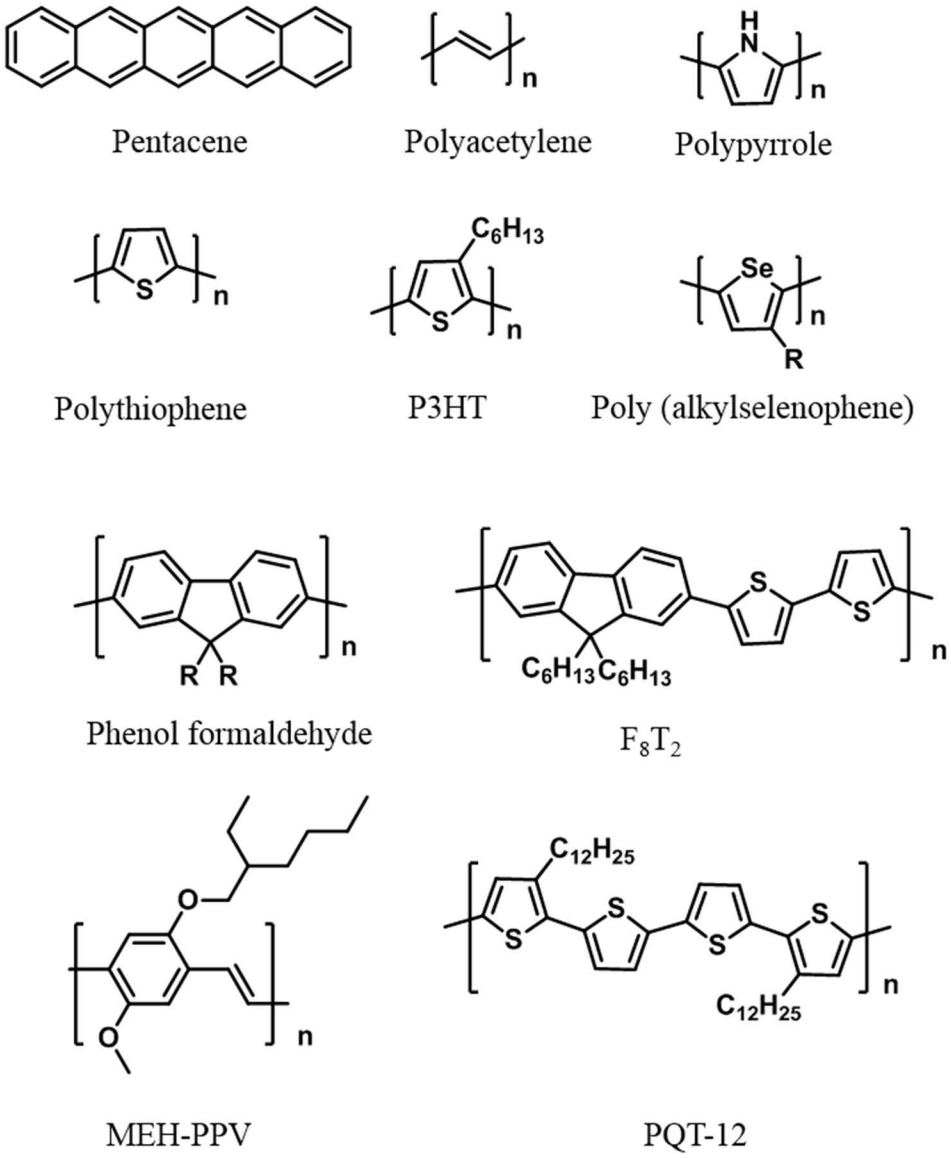

Fig. 1. 5 Chemical structures of p-type small molecules and polymer semiconductors

C60 Fullerene

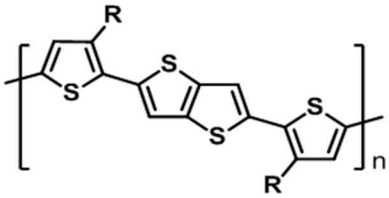

PBTTT

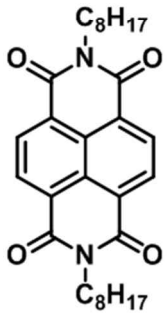

F15-NTCDI

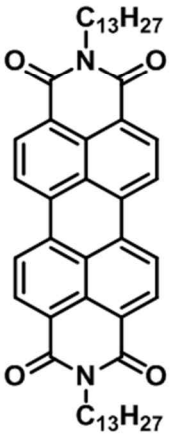

PTCDIC13H27

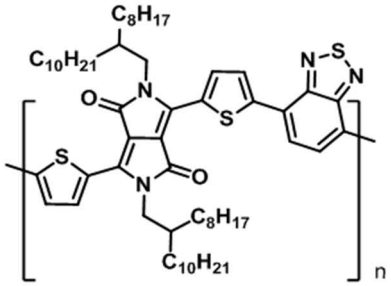

PDPP-TNT

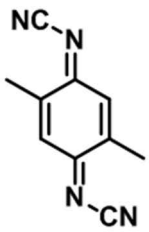

Dimethyldicyanoquinone-diimine

Fig. 1. 6 Chemical structures of n-type small molecules and polymer semiconductors

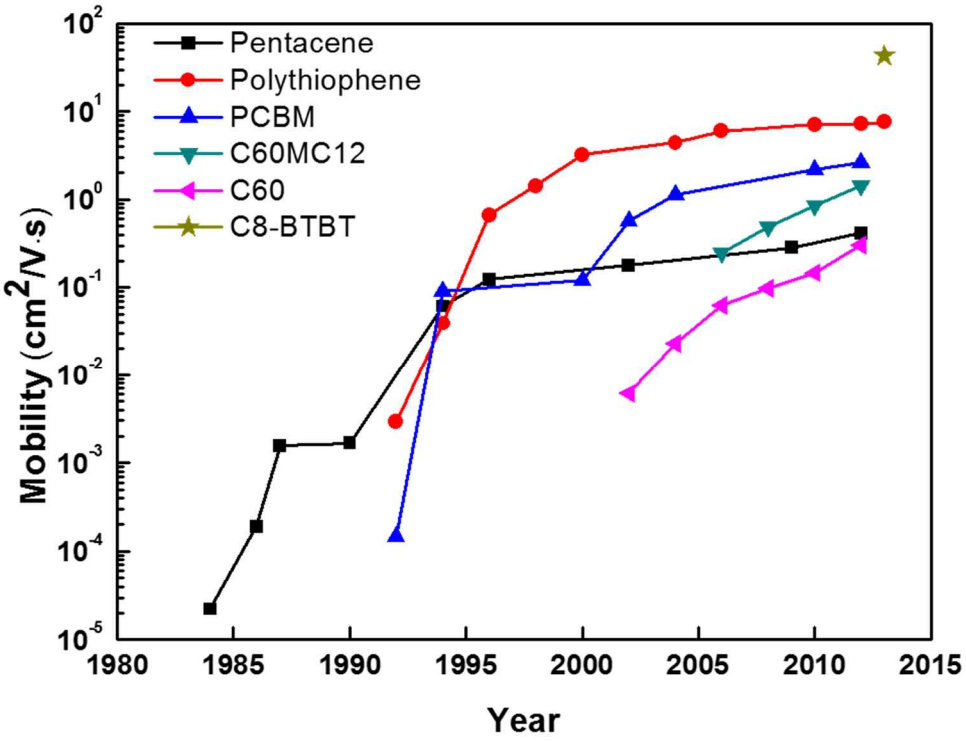

Fig. 1. 7 Mobility progress of organic semiconductors[28, 32]

L. Malenfant reported that same linear density of SWNT show different mobility (5-43 $cm^2V^{-1}s^{-1}$) as shown in the Fig.1.8[33]. This result implies that difference of mobility is not attributed to SWNT linear density, but also SWNT-SWNT junction, surface contamination and SWNT purity. Also presence of a wrapping polymer in the SWNT reduces the probability of charges tunneling among the SWNTs and contributes to the resistance of the SWNT network and the presence of metallic nanotube lead to high carrier mobility and low on/off ratios[34]. The diameter and the length of the CNTs obtained by the synthesis method of the SWNTs are different. Commercial SWNTs including CoMoCat, HiPCO, Plasma discharge, and Arc discharge are widely used. The four SWNT sources with the largest band gap (smallest diameter) are expected to increase mobility as the band gap decreases. This is expected to be due to a decrease in the average band gap of the SWNTs, fewer heat carriers, and an increase in the band gap variation of the individual SWNTs, which increases the tunneling barrier among the different chirality SWNTs. Recently, research on Tuball with a large diameter has been carried out[34]. Fig 1.9 show on/off ratio versus mobility for SWNT TFTs [35-54].

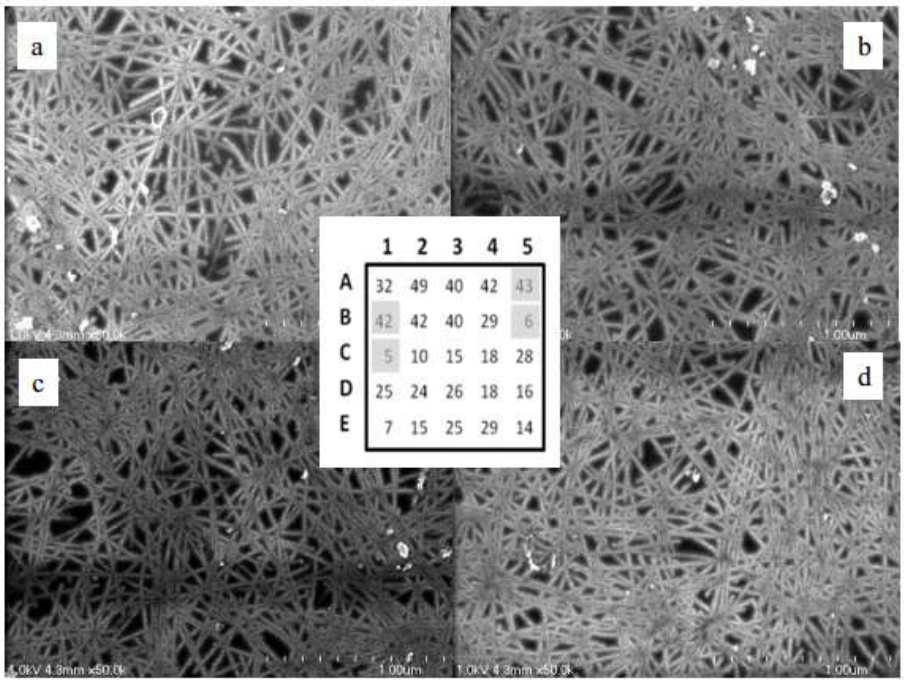

Fig. 1. 8 SEM images of the nanotube networks formed in devices (a) A5 mobility of 43 $cm^2 V^{-1} s^{-1}$, (b) B1 mobility 42 $cm^2 V^{-1} s^{-1}$ (c) B5 mobility of 6 $cm^2 V^{-1} s^{-1}$ and (d) C1 mobility of 5 $cm^2 V^{-1} s^{-1}$ and the layout of the 25 devices on the single chip and their corresponding mobility values (inset)

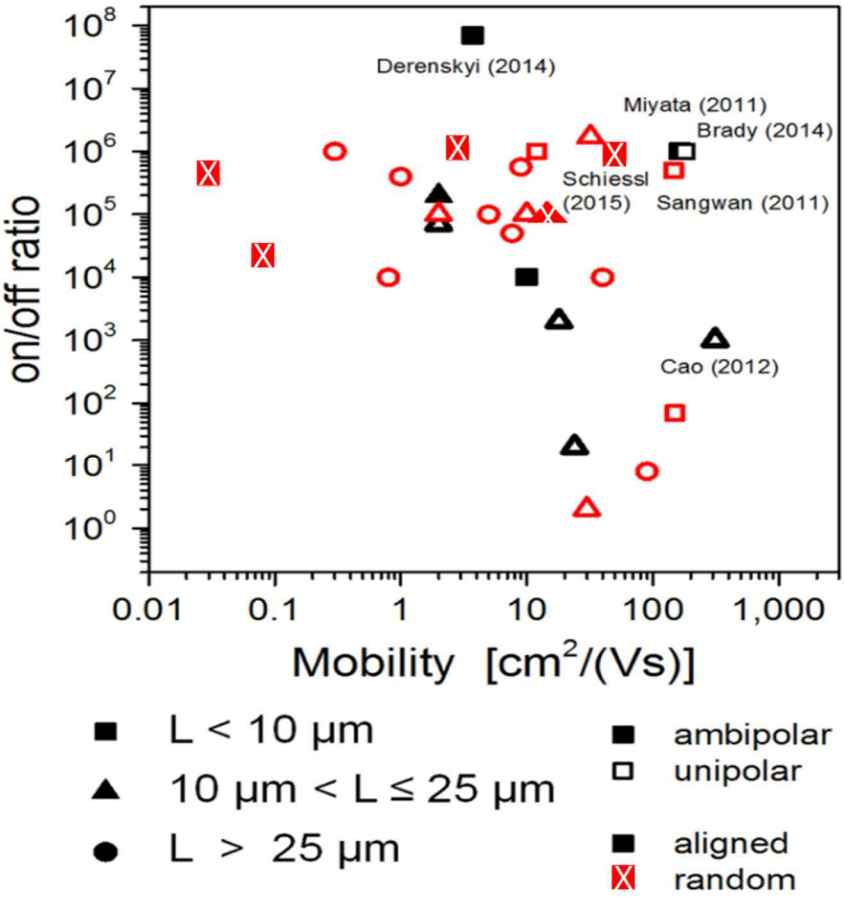

Fig. 1. 9 Mobility and on/off ratio map for SWNT TFTs [35-54]

Carbon allotropes

Carbon, the common material we use since ancient times, has become very for industry, and is closely related to an advanced technology and its every field. The carbon nano tubes (CNTs) are allotropes of carbon with a cylindrical shaped nanostructures and they have unique properties that are valuable for nanotechnology, electronics, optics and other fields of materials science and technology. The family of carbon are diamond, graphite, carbon nanotubes and fullerene. Diamond is composed of sp^3 carbon atoms, and is the hardest natural material with Mohs hardness of 10 and is applied as an industrial polishing and cutting tool. Figure 1.10 shows crystal structures of different carbon allotropes. Graphite consists of pure sp^2 hybridized carbon atoms, and has a layered-planar structure. The carbon atoms are arranged layer by layer in a hexagonal lattice with a lattice parameter of 1.42 Å, and the distance between planes is 3.35 Å. Graphite is used in industry for lubrication. Graphene is composed of pure sp^2 hybridized atoms, and has one carbon atom-thick planar sheet forming a honeycomb crystal lattice.[55] Graphene is considered as the mother of all graphitic forms, and it is the basic structural element of some carbon allotropes. The Graphene can be wrapped up into 0D (C_{60}), rolled into 1D (carbon nanotubes) and stacked into 3D (graphite). Graphene has high electronic quality, it is used in integrated circuits, solar cells, ultra-capacitors and thin film transistors. It is also used as transparent conducting electrodes in many other device. The C_{60} Nano spheres are formed by 60 carbon atom with each carbon atom covalently bonded to three adjacent carbon atoms.[56]

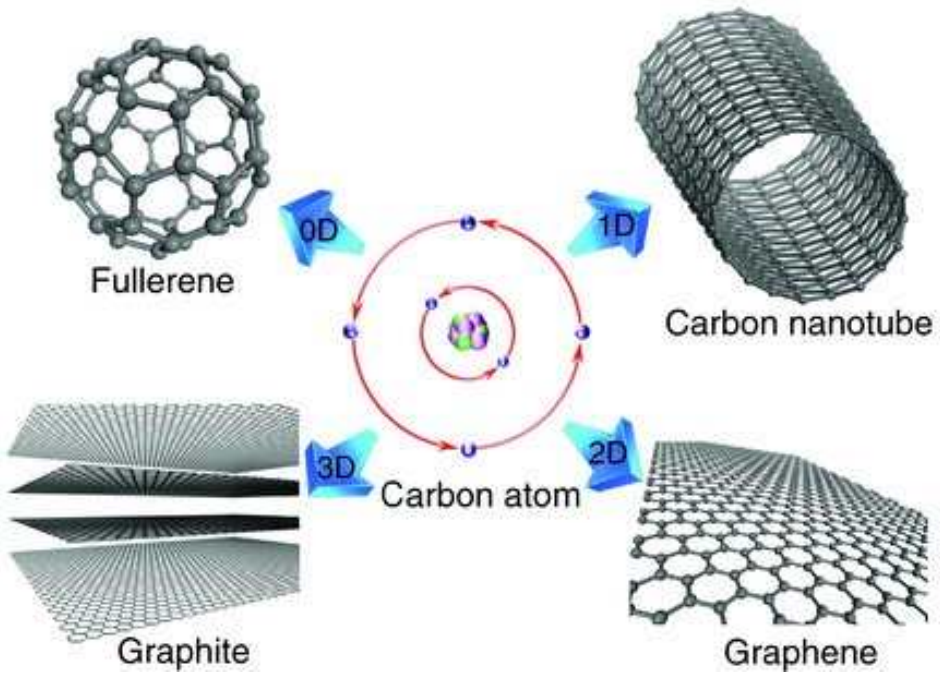

Fig. 1. 10 Crystal structures of different carbon allotropes[57]

The diameter is around 1 nm, the hardness is greater than that of diamond, and it is a promising material for the applications as polymer fillers to increase mechanical strength.

The CNTs are high aspect ratio hollow pipes, and exist due to hybridize sp^2 of C atoms. They are beneficial for principally stretchable devices because large aspect ratios enable good stretch ability of the SWNT network and high modulus warrant excellent durability. Rolling up a Graphene sheet causes differences between the three bonds. Figure 1.11 shows structure of SWNTs[58]. In the case of zigzag nanotubes, the orientation bonds are the same at the nonzero angle to the axis of the cylinder, but different from oriented bonds in the axial direction, unaffected when rolling Graphene strips. Due to the armchair the orienting bonds are not identical at the nonzero angle around the cylinder, and the nanotubes differing in orientation in the circumferential. Due to the armchair the orienting bonds are not identical at the nonzero angle around the cylinder, and the nanotubes differing in orientation in the circumferential direction. All three bonds are slightly different from other chiral nanotubes[58, 59]. Through the individual tubes in the bundle, they are fascinated by their nearest neighbors van der Waals interaction with a typical distance between a certain nanotubes.

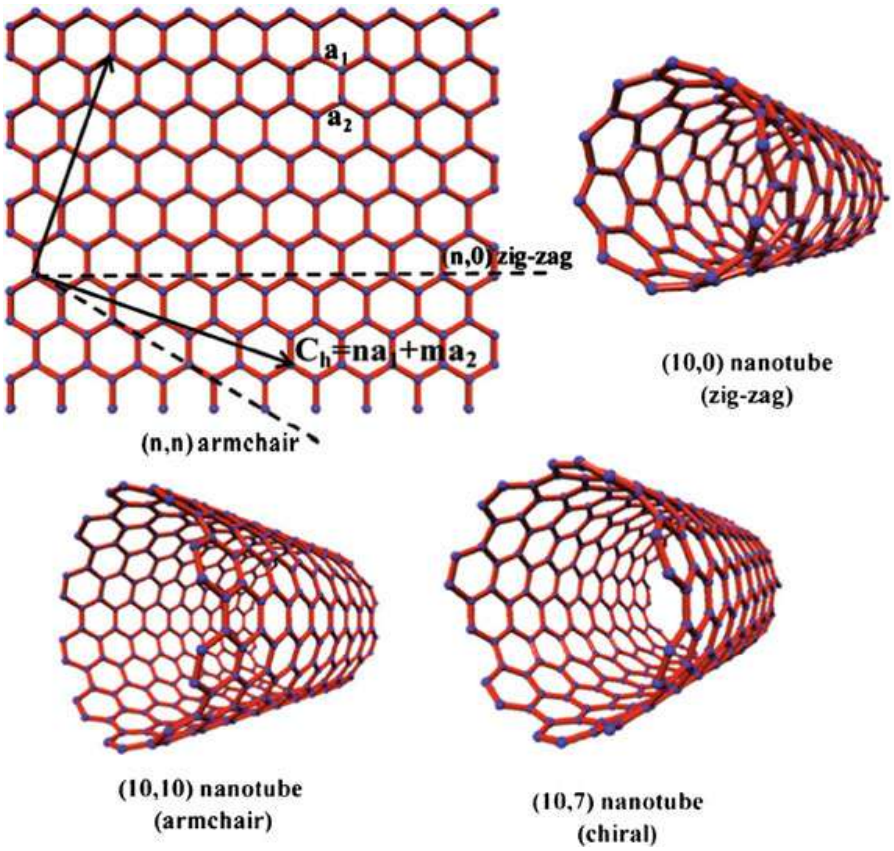

Fig. 1. 11 Structures of SWNTs[58].

The Electronic Band Structure of SWNTs

In real space, the lattice structure of Graphene is hexagonal arrangement of carbon atoms. Fig 1.12 shows the lattice structure of Graphene in real space[60]. The Carbon atoms (atomic number 6) have four valence electrons in 2s, $2p_x$, $2p_y$ and $2p_z$ atomic orbitals. In case of carbon atoms form Graphene, three atomic orbitals, 2s, $2p_x$, and $2p_y$, are hybridized into three sp^2 orbitals in the same plane while the $2p_z$ orbital remains perpendicular to other orbitals. The hybridized orbitals are responsible for σ bonds between the adjacent carbon atoms and the $2p_z$ orbital results in π bonds out of the plane of Graphene. The electrons (holes) near the Fermi level determined electrical transport properties, these electrons (holes) have access to the unoccupied (occupied) states. The grapheme's band structure derived from π orbital can be calculated by the tight-binding model[61]

Due to find the band structure of the Graphene π orbitals, first, we try to find the solutions of the Schrödinger equation

Eq 1.1

$$H\Psi = E\Psi$$

Where H is the Hamiltonian, Ψ is the total wave function, and E is the electrons energy in the π orbitals of graphene.

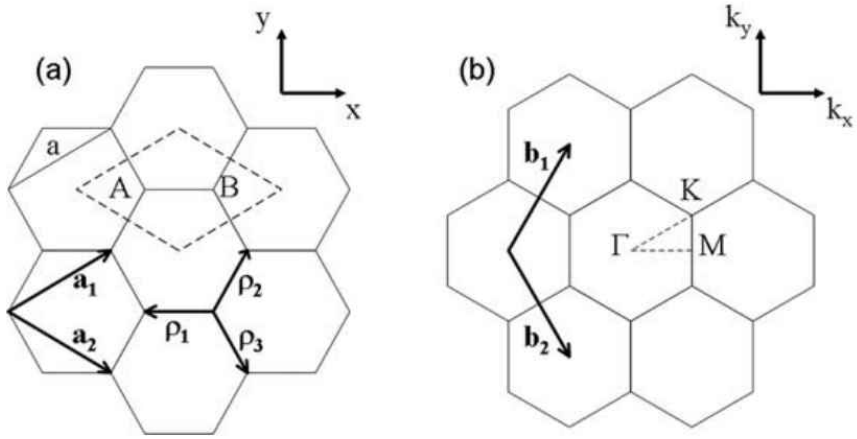

Fig. 1. 12 Crystal structures of carbon allotropes (a) Graphene lattice in real space, unit cell is displayed as a dashed rhombus with two carbon atoms (A and B). Unit vectors, $a_1$and a_2, with length "a", are shown. Vectors ρ_j connect nearest neighbor carbon atoms. (b) Reciprocal space representation of a Graphene lattice with two unit vectors b_1 and b_2. High-symmetry points Γ, K, M) in a Brillouin zone, are also shown[60]

For instance of periodic system as in Graphene, the total wave function is constructed from a linear combination of Bloch function u_i. We considered only the π orbitals that originate from the $2p_z$ orbital of each carbon atom. Bloch function u_i for each atom can be constructed from $2p_z$ orbitals of atoms A and B as

Eq 1.2

$$u_{A(B)} = \frac{1}{\sqrt{N}} \sum_{A(B)} e^{\boldsymbol{k}\, r_{A(B)}} X\left(r - r_{A(B)}\right)$$

Where X(r) is the orbital $2p_z$ wave function for an isolated carbon atom

Then, Ψ in Eq. (1.1) can be used as follows:

Eq 1.3

$$\Psi = C_A u_A + C_B u_B$$

By substituting Eq. (1.3) into (1.1), the Schrödinger equation can be fined solution to in a matrix form as follows:

Eq 1.4

$$\begin{pmatrix} H_{AA} & H_{AB} \\ H_{BA} & H_{BB} \end{pmatrix} \begin{pmatrix} C_A \\ C_B \end{pmatrix} = E \quad \begin{pmatrix} S_{AA} & S_{AB} \\ S_{BA} & S_{BB} \end{pmatrix} \begin{pmatrix} C_A \\ C_B \end{pmatrix}$$

Here,

Eq 1.5

$$H_{ij} = \langle u_i | H | u_j \rangle , S_{ij} = \langle u_i | u_j \rangle$$

For briefness, the overlap between $2p_z$ wave functions of different atoms are abandoned, i.e., $S_{AB}=S_{BA}=0$. We can also see that $S_{AA}=S_{BB}=1$ (normalized),

then Eq. (1.4) is simplified to

Eq 1.6

$$\begin{pmatrix} H_{AA} - E & H_{AB} \\ H_{BA} & H_{BB} - E \end{pmatrix} \begin{pmatrix} C_A \\ C_B \end{pmatrix} = \begin{pmatrix} 0 \\ 0 \end{pmatrix}$$

This is matrix equation has a significant solution when

Eq 1.7

$$\begin{vmatrix} H_{AA} - E & H_{AB} \\ H_{BA} & H_{BB} - E \end{vmatrix} - - - (eq\,.1.7)$$

we can consider that $H_{AA}=H_{BB}$ by symmetry of the Graphene lattice (atoms A and B are not distinguishable) and $H_{AB}=H_{BA}^{*}$. Then, Eq. (1.7) leads to the solution

Eq 1.8

$$\mathrm{E} = H_{AA} \mp |H_{AB}|$$

Eq 1.9

$$H_{AA} = \frac{1}{\sqrt{N}} \sum_{A} \quad \sum_{A^*} e^{\boldsymbol{k}\,(r_A - r_{A^*})} \int X^*\ (r - r_A) H\, X\ (r - r_{A^*}) d\tau$$

If we cogitate the nearest neighbors, we demand to evaluate eq 1.9 for each atom A (B) with three nearest neighbor B (A) atoms.

Eq 1.10

$$H_{AA} = \int X^*\ (r - r_A) H X\, (r - r_{AA^*}) d\tau = E_0$$

Eq 1.11

$$H_{AB} = \frac{1}{\sqrt{N}} \sum_{A} \quad \sum_{B} e^{\boldsymbol{k}\,(r_A - r_B)} \int X^*\ (r - r_A) H\, X\ (r - r_B) d\tau$$

$$= \frac{1}{\sqrt{N}} \sum_{i} e^{\boldsymbol{k}\,\rho_i} \int X^*\ (r) H\, X\ (r - \rho_i) d\tau$$

Where ρ_i is a vector connecting atom A to its three nearest neighbor B atoms.

Eq 1.12

$$H_{AB} = \left(e^{\boldsymbol{K}\,\rho_1} + e^{\boldsymbol{K}\,\rho_2} + e^{\boldsymbol{K}\,\rho_3}\ \right) \int X^*(r) H X(r-\rho_1) d\tau$$

$$= \gamma_0 (e^{-ik_x} \mathrm{a}\, a/\sqrt{3} + 2e^{-ik_x\, a}/2\sqrt{3} \cos\left(\frac{k_y a}{2}\right)$$

γ_0 is often indicated as the tight-binding integral or transfer integral which measures the strength of exchange interaction between nearest neighbor atoms. (1.10) and (1.12), the energy distribution in Eq. (1.8) can be calculated as follows

Eq 1.13

$$\mathrm{E} = E_0 \mp \gamma_0 (1 + 4\cos\left(\frac{\sqrt{3}k_x a}{2}\right)\cos\left(\frac{k_y a}{2}\right) + 4\cos^2(\frac{k_y a}{2}))^{1}/_{2}$$

In Eq. (1.13), negative sign means valence bands of Graphene formed by bonding π orbitals. The density of states (DOS) in Graphene can be derived from the energy diffusion relation and we found to be zero at the Fermi level.[62, 63] The incline of the conic shape dispersion near K points is related to the Fermi velocity of electrons in Graphene, V_F=8×10^5 m/s [63], as follows:

Eq 1.14

$$\left.\frac{dE}{dk}\right|_K = \frac{\sqrt{3}}{2} \mathrm{a}\gamma_0 = \hbar v_f$$

The electronic structure of a SWNT is derived from that of 2D Graphene using periodic boundary conditions. The wave vectors allied with the direction normal to the tube axis become quantized. The wave vectors along the tube axis

remain continuous assuming an infinite tube length. Therefore, relations of the energy dispersion are cross zone of those of 2D Graphene. Graphene is a zero-energy gap semiconductor with the p and p*-states being degenerate by symmetry in the K-points. If a specific (n, m)-nanotube the cutting line moves through a K point, the 1D energy bands have a zero energy gap and therefore are measured as being metallic in first approximation. All metallic CNTs satisfy the equation

Eq 1.15

$$(n - m) = 3q$$

with q is an integer. All armchair (n, n) and zigzag (n, 0)-CNTs are metallic when n is a multiple of three. This equation also suggests that one-third of SWNTs show metallic property. In addition, the finite curvature of the SWNT results in the mixing of p/r bonding and p*/r* anti-bonding states leading to a movement of the Graphene band pass from the K-point. Small energy gaps in the order of meV are introduced in metallic SWNTs except for the symmetrical achiral (n, n) armchair SWNTs. Therefore, SWNTs satisfying (n-3) =3q are regarded as quasi metallic or tiny-gap semiconductor if n = m. Fig.1.13 shows electronic density of state of 3, 2, 1 and 0 D[64, 65]. The DOS of semiconducting SWNTs (s-SWNTs) is zero at the Fermi level (EF) positioned at E = 0, but non-zero for metallic SWNTs (m-SWNTs). Due to the 1D nature of the nanotubes, the DOS becomes singular by

folding the 2D energy bands of the Graphene layer into the 1D bands of the SWNT with an increasing energy separation at decreasing number of energy bands. As a result, prickles in the DOS of 1D materials arise (van Hove singularities, vHS) which govern the optical properties of SWNTs. The band gap decreases from smaller to larger diameter SWNTs, while being independent on the chiral angle[66].

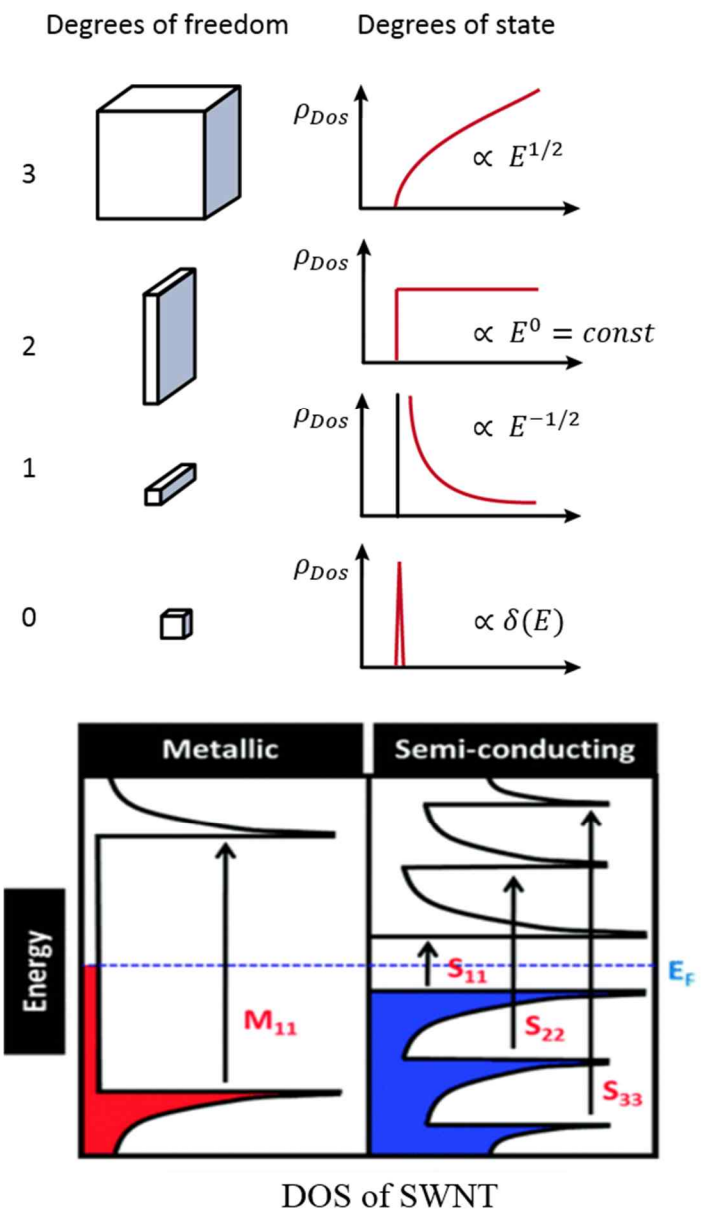

Fig. 1. 13 Schematic diagram of electronic density of state of 3, 2, 1 and 0 D.[64, 66]

Synthesis of Single Wall Carbon Nanotubes

SWNTs are synthesized by several methods. It is high temperature and low temperature method. There is a difference in length thickness difference between CNTs according to the synthesis method. Iijima used the method to synthesize MWCNTs in the carbon soot of graphite electrodes using arc-discharge method in 1991. Fig 1.14 (upper) show set up of arc discharge method. It is produced under high current [67]and it was first established to synthesize carbon nano-onions.[68] During this process, the carbon contained in the negative electrode sublimates because of the high discharge temperature. Iijima used the method to synthesize MWCNTs in the carbon soot of graphite electrodes. Bulk quantities of MWCNTs can be produced by this method under suitable arc-evaporation conditions. After adding catalysts, SWNTs were also produced and sometimes even in large quantities. The arc discharge SWNTs have very few structural defects and are quite straight and good crystallinity. A high pressure carbon monoxide (HiPCO) process as shown in Fig. 1. 14 (lower), it was synthesized in high pressure (30-50 atm) high temperature (900-1100 ℃) with iron catalysts, could produce high purity SWNTs (97%).

$$\mathrm{CO} + \mathrm{CO} \longrightarrow \mathrm{C}\ (\mathrm{SWNTs}) + CO_2$$

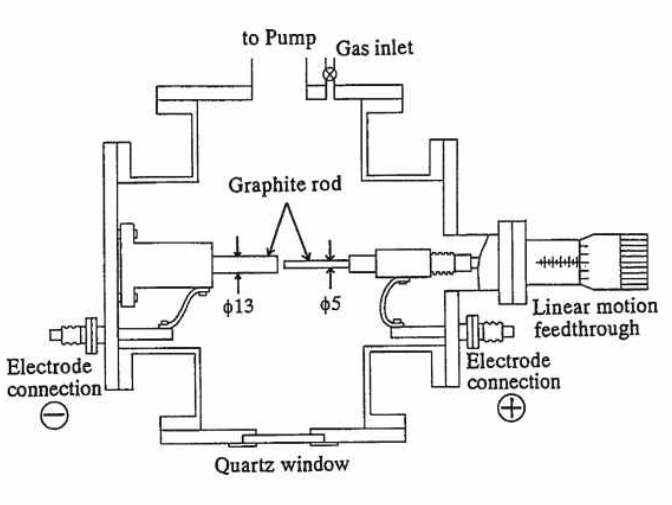

Arc discharge

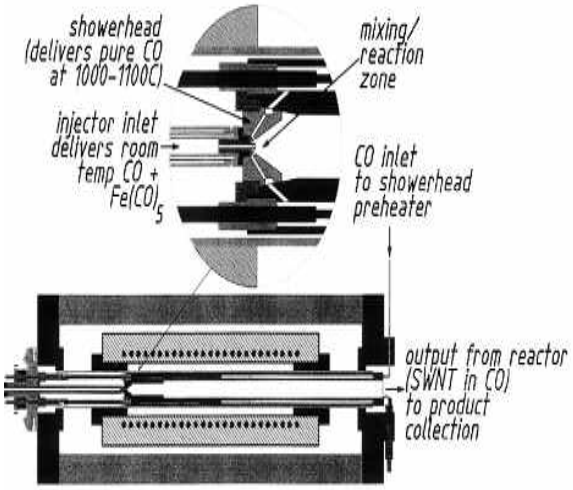

HiPCO process

Fig. 1. 14 Set up of arc discharge techniques and HiPCO process

Smalley et al reported the synthesis of CNTs by laser vaporization[69]. Figure 1. 11(upper) shows laser vaporization tool[70]. Laser is used to vaporize a graphite target in an oven at 1200℃. A hot vapor spiral forms, then swells and cools quickly. During the vaporized sorts cool, small carbons condense to form larger bunches including fullerenes. Catalyst particles convert that highly coated with a carbon layer that they did not absorb and the nanotube growing stops.

Fig 1.15 (lower) shows Plasma discharge process. Plasma discharge used commercial carbon black powder and metal catalysts including mixtures of nickel, yttrium oxide and cobalt. These feedstock materials were introduced axially through the water-cooled probe located at the center of the plasma torch. The SWNT was synthesized at 40 kW and a 500 torr pressure. To forming plasma, a mixture of argon and helium gases was used and transfer of the feedstock materials. They have impurities according to soot materials, amorphous carbon, graphitic carbon particles, and catalysts. SWNTs diameter of Arc discharge, HiPCO, Laser ablation and Plasma discharge are 1.2~1.7, 0.8~1.2, 1.0~1.4, and 1.2~1.6 nm, respectively. Due to different diameter and length, they showed different electronic characteristics as shown in Fig 1.16[34].

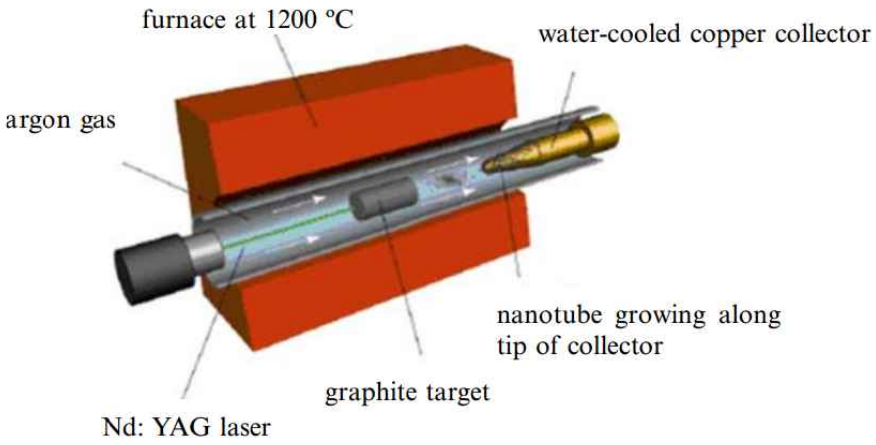

Laser ablation

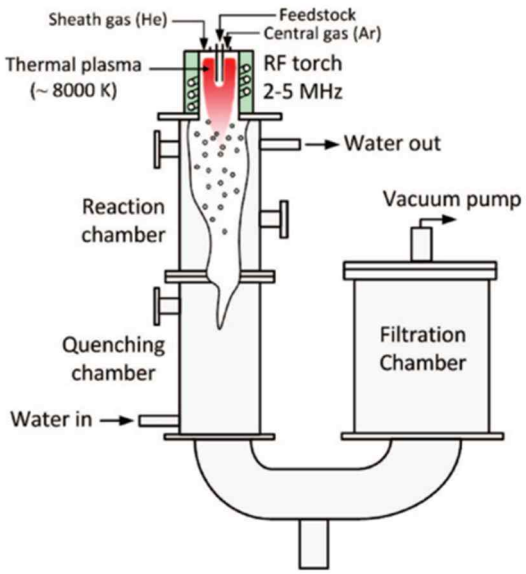

Plasma discharge

Fig. 1. 15 Set up of a laser ablation apparatus[70] and Plasma discharge process[71]

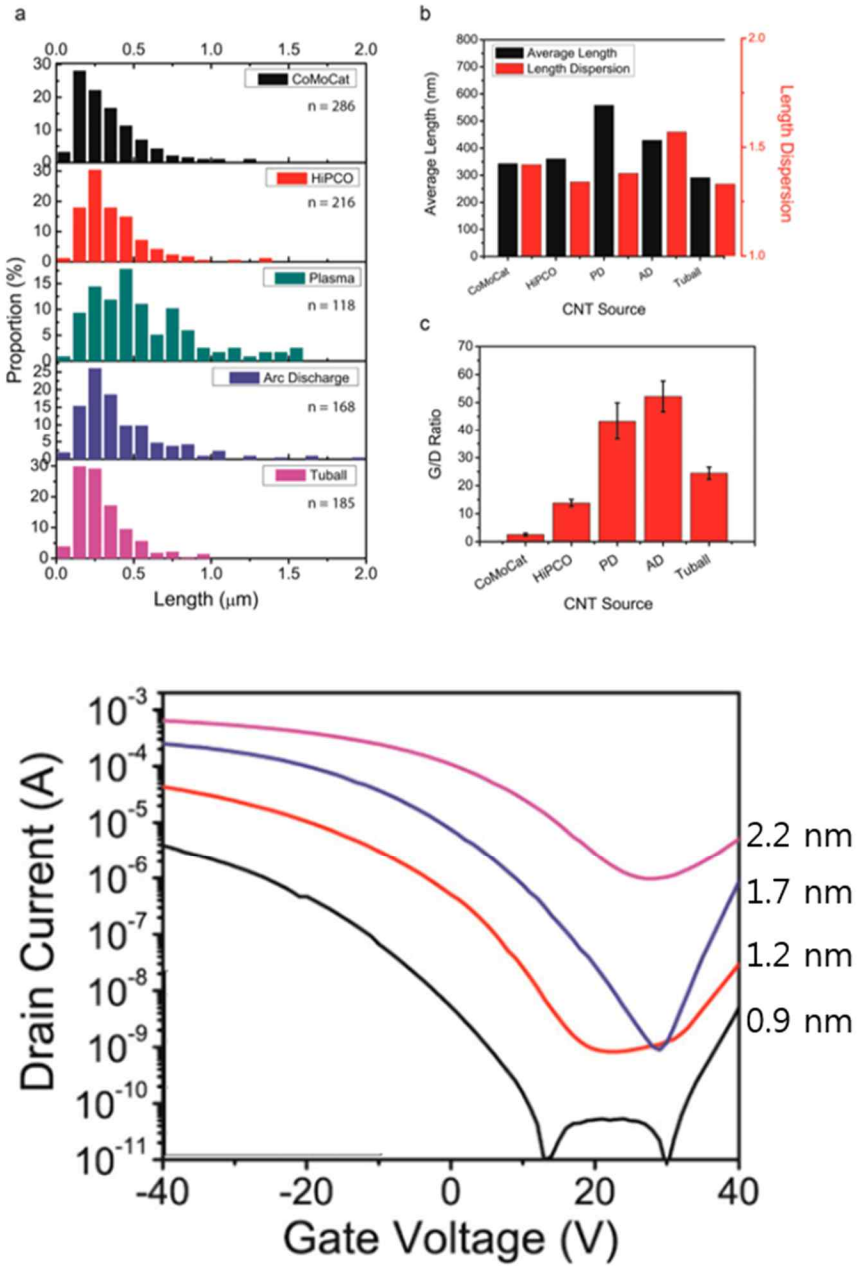

Fig. 1. 16 SWNT length histograms and transfer curves for different SWNT sources[34]

Outline of this thesis

In this thesis, solution-processed thin film transistors is investigated based on single wall carbon nanotubes with hetero structured.

We sort off high-purity semiconducting single-walled carbon nanotubes by polymer wrapping method. We show the selection of s-SWNTs in SWNTs grown by the high pressure carbon mono oxide (HiPCO) process using poly-9,9-di-n-octyl-fluorenyl-2,7-diyl (PFO) and poly (3-dodecylthiophene-2, 5-diyl) (P3DDT), the wrapping polymer was used poly (9, 9-di-n-dodecylfluorene) (PFDD) for plasma discharge process (PD) SWNT. We analyzed the purity, concentration and random network surface with Ultraviolet-visible spectroscopy, Raman spectroscopy, Atomic force microscope, Field emission scanning electron microscopy, and Transmission electron microscopy. (Chapter 2)

We fabricated transistors by using high purity semiconducting SWNTs ink. We demonstrate new patterning process, the patterned transistor, the leakage was under 10^{-11} A level. The P3DDT-HiPCO transistors show high on/off ratio, but low mobility, while the PFDD-PD exhibit high mobility with high off current level. A hetero structure system was adopted to solve these challenges. And by this way, we achieved a hole mobility of 7 cm^2/VS and on/off ratio of 1.5×10^7. And $FeCl_3$-doping hetero structure system, we achieved a hole mobility of over than 100 cm^2/VS (V_d = -20V) and on/off ratio of 10^6 (V_d=-5V). (Chapter 3)

Chapter 2 Polymer wrapped s-SWNTs

Introduction

Nowadays, with the popularization of mobile devices, the demand for flexible devices is increasing. Single wall carbon nanotubes have random network structure when they form films, exhibit high carrier mobility and excellent mechanical properties, which makes them a one of the suitable materials for flexible devices. However, they have both metallic and semi-conductive properties in the synthesis, so it is necessary to sort only the semiconducting properties. There have been several ways to separate this mixture[72-75].(Fig2.1) Density Gradient Ultracentrifugation (DGU) uses density difference the buoyant of SWNT by the use of surfactants such as sodium dodecyl sulfate (SDS) and sodium chlorate (SC). Idixanol or sucrose are utilized as a density gradient medium. After DGU, colored layers appear in solution due to the different densities. Small diameter SWNT have larger density than small diameter species.

Gel Chromatography is another method to sort off s-SWNTs according to their size difference. SWNTs are dispersed in surfactant (SDS SC)) and embedded in an alkyl dextran based gel. This is an effective alternative to sort off SWNTs according to their diameter, length and electronic type sorting of SWNTs for large scale, although can only to separate small diameters SWNTs.

DNA can be attached to SWNT via $\pi - \pi$ stacking with helical structures. By tuning

the structure and sequence of DNA. This can achieve efficient isolation and selection of a broad range of SWNTs species. Similarly to DNA wrapping, polymer chains bind a helical conformation around SWNTs due to the interaction between the π-conjugated polymer chains and the side walls of nanotubes around SWNTs. Polyfluorene derivatives, P3DDT and conducting polymer were used.

Polymer dispersion method has advantages of high-throughput, high yield, and low cost Many group have been reported that a polyfluorene (PFO)-based conjugated polymer to selectively individualize SWNTs[74]. Bao group separated s-SWNTs by using different the alkyl side chain lengths, configurations, and density of side chains of regioregular poly (3-alkylthiophene)s[76] and recently reported literature, one type of supramolecular polymer was able to selectively disperse s-SWNTs from commercial SWNTs with different diameter distributions..[34]

Here we demonstrate the selection of s-SWNTs in SWNTs grown by the high pressure carbon mono oxide (HiPCO) process using poly-9,9-di-n-octyl-fluorenyl-2,7-diyl (PFO) and poly (3-dodecylthiophene-2, 5-diyl) (P3DDT). In case SWNTs grown by the plasma discharge process (PD), the wrapping polymer was used poly (9, 9-di-n-dodecylfluorene) (PFDD). The UV-vis-NIR absorption spectra of PFO-HiPCO and P3DDT-HiPCO show the intensity of the peaks s-SWNTs increases in the range between 1000 nm and 1500 nm. The purity of s-SWNTs in PFO-HiPCO, P3DDT-HiPCO sample is estimated over 99% based on the absorption spectra, Raman spectroscopy. UV-vis-NIR absorption spectra display the reduction of the polymer peaks under 400 nm (PFDD) for PFDD-PD (P3DDT). Raman spectra

illustrates PFDD warped PD (PFDD-PD) contains a small amount of metallic SWNT. The purity of PFDD-PD is evaluated by using comparison of the absorption peak ratio. Atomic force microscope (AFM) exhibits that the both s-SWNTs networks form well-percolated morphology.

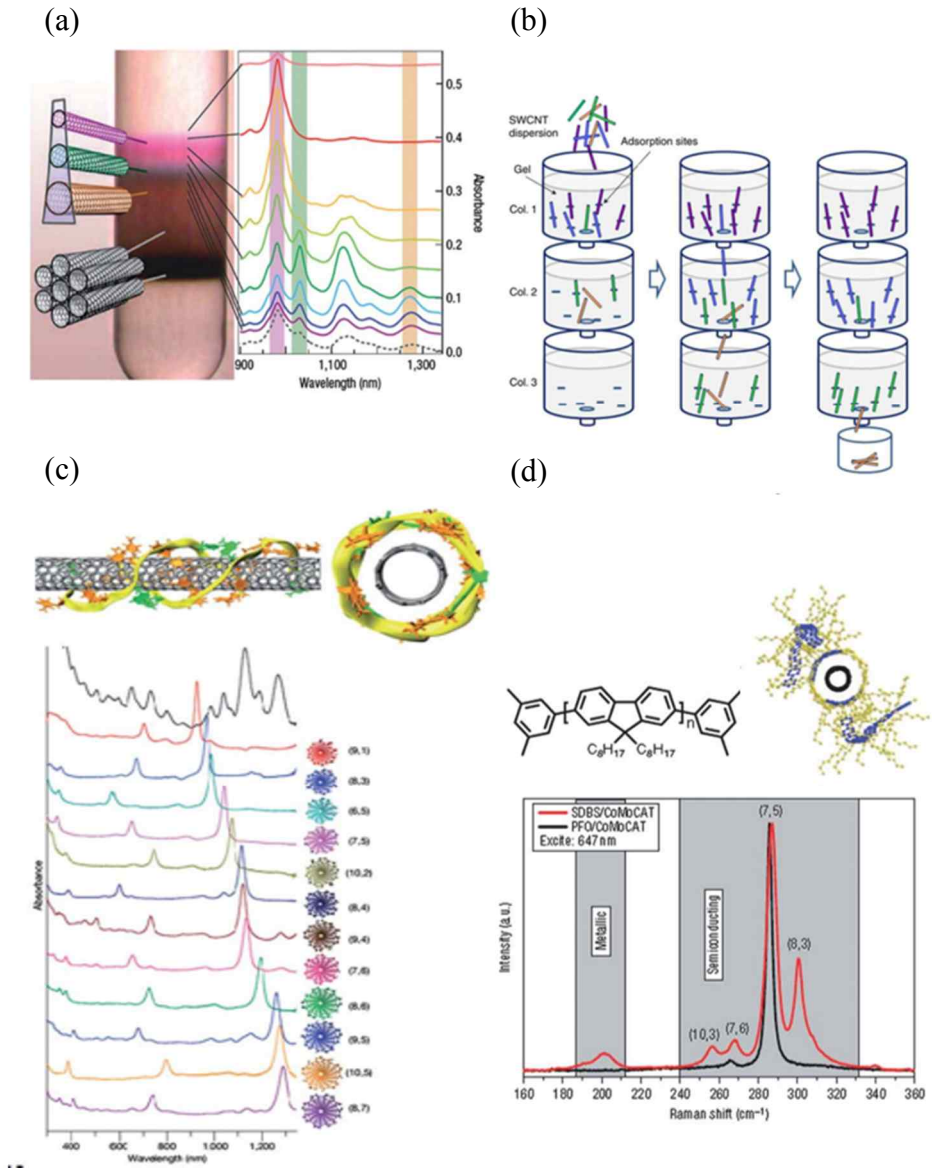

Fig.2. 1 Various sorting methods (a) DGU (b) GPC (c) DNA (d) polymer wrapping method [72-75]

Experimental

Preparation of the SWNT dispersion

The polymers used in this study were PFO (Lumtec, Mw≤20,000g/mol), PFDD (Lumtec, Mw≈15,000 - 200,000), and P3DDT (Leika metal 20,000 ≤Mn≤50,000 g/mol). SWNTs grown by HiPCO (diameter 0.8–1.2 nm, purified <13 wt % iron) and PD were purchased from Nanointegris Inc. Fig 2.2 shows process of polymer wrapping method. The toluene solutions of PFO (1 mg/ml), PFDD (1mg/ml) and P3DDT (1mg/ml) were prepared and heated at 80ºC for 2 hr for complete dissolution. After cooling, the solutions were prepared at 0.5mg/ml by adding the HiPCO powder to PFO and P3DDT and the PD powder to PFDD. The solutions were homogenized in an ultrasonic bath (Branson 5510) for 1hr. The solution was centrifuged at 85,000g for 1 hr (separation of s-SWNT), the supernatant was further at 199,000g for 1 hr and the supernatant was further ultra-centrifuged at 320,000g for 10 hr (removal of free polymer) (Vision scientific Inc VS-65 ultracentrifuge, V1308Ti fixed rotor). The following pellets were washed several times for remaining polymer and collected. Finally this enriched pellets were re-dispersed in toluene using bath sonication.

Characterizations

UV-Vis spectra were measured using carry 5000(varian). Atomic Force Microscope (AFM) topographic images were obtained in a PSIA XE-100 scanning probe

microscope with non-contact mode. The Raman measurements were done with LabRAM HV Evolution (HORIBA). Field effect scanning electron microscopy (FE-SEM) was obtained using a JSM-7600F (JEOL). Transmission electron microscopy (TEM) was obtained in JEM-3000F (JEOL).

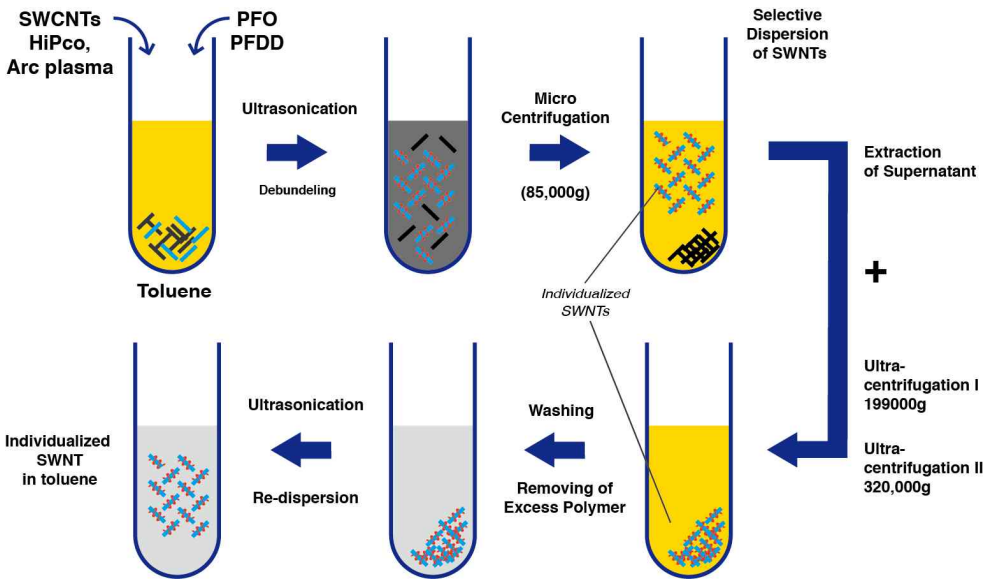

Fig.2. 2 Polymer wrapping s-SWNTs process

Result and discussion

UV-Vis-NIR absorption spectra of PFO-HiPCO and P3DDT-HiPCO

The UV-Vis-NIR absorption spectra has been used to conform the purity of s-SWNT[33]. In order to select the s-SWNT from HiPCO, we used two different polymer, PFO and P3DDT. Fig.2.3 displays the absorption spectrum of PFO and P3DDT solutions, we can see that the PFO only has crest peak at 400 nm while P3DDT shows a single peak at 600nm. The absorbance spectra of sorted SWNTs solution show HiPCO sorted using PFO and P3DDT (Fig 2. 4). PFO wrapped s-HiPCO (PFO-HiPCO) present two absorption bands in the regions of 1100-1400 nm for S_{11}, 700-800 nm for S_{22}, PFO can select five different semiconducting species[74], while absorption peak of P3DDT wrapped HiPCO (P3DDT-HiPCO) was appeared in the region of 1000-1500 nm. All these bands and the polymer peak are well resolved. The peak of absorbance show the P3DDT-HiPCO is higher than PFO-HiPCO. That means that the lengths of the conjugated polymer side chain was relative to the quantity and the type of s-SWNT[37]. In case of PFDD-PD, the metal absorption peak (440-600 nm) of P3DDT-HiPCO overlaps with the absorption wavelengths of the P3DDT polymer (600 nm). In order to check and confirm the existence of the metallic SWNT in our solution, we have also conducted Raman spectroscopy measurement

(a)

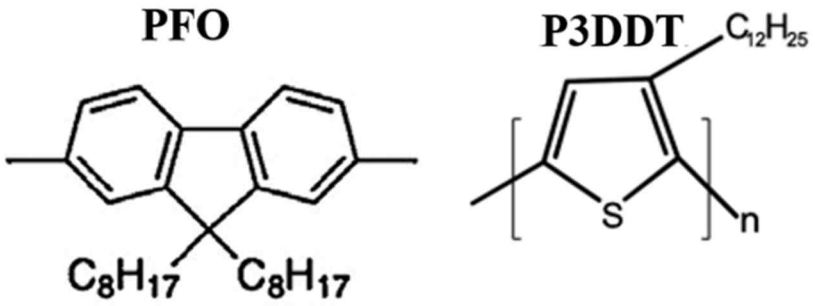

(b)

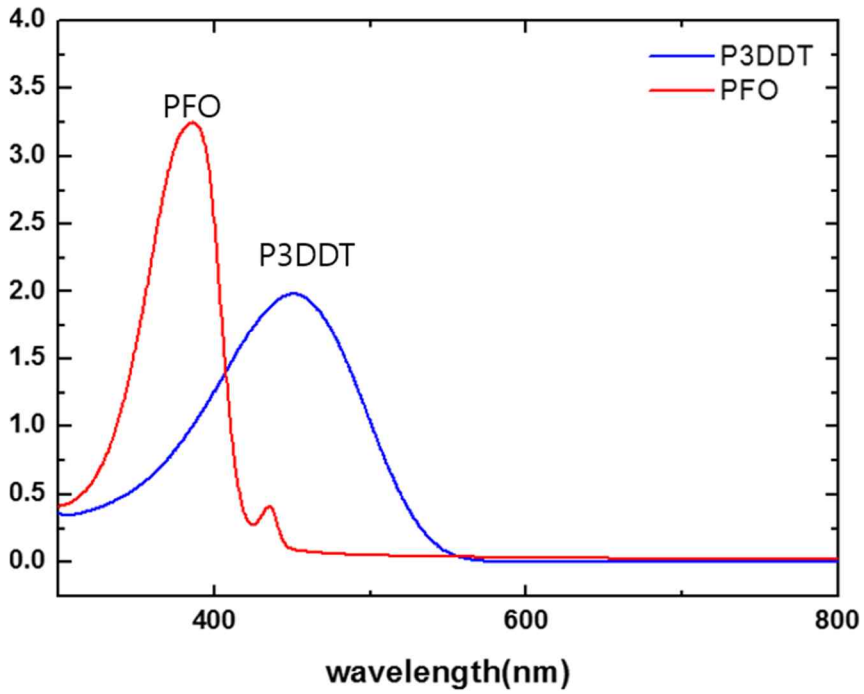

Fig.2. 3 Chemical structure PFO and P3DDT (a); UV-Vis-NIR absorption spectra of PFO (red line) and P3DDT (blue line) solutions (b)

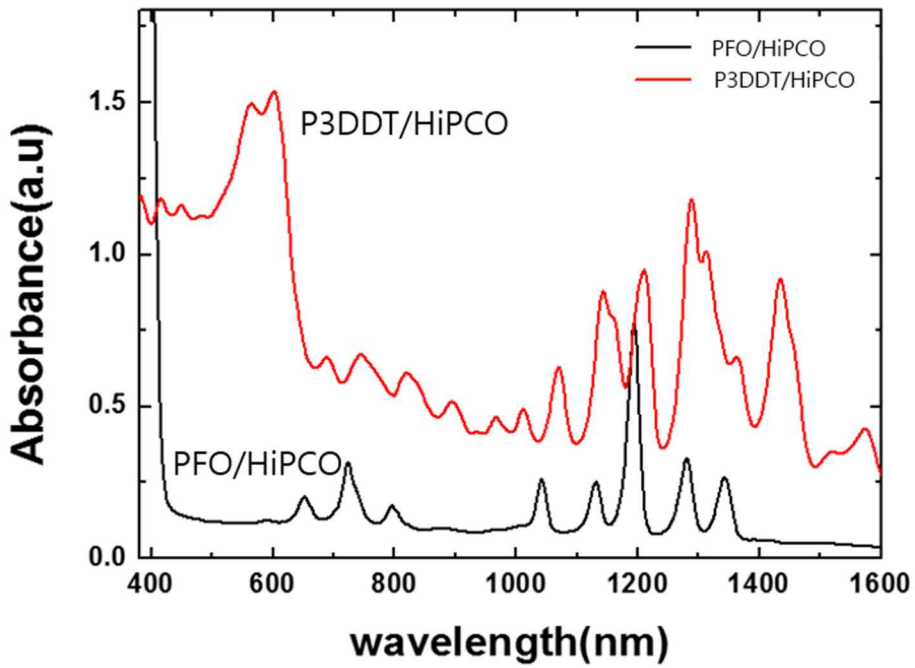

Fig.2. 4 UV-Vis-NIR absorption spectra of PFO-HiPCO SWNTs (black line) and P3DDT-HiPCO SWNTs (red line)

Raman spectroscopy is a useful tool for carbon nano phases. SWNT and Graphene. The three most prominent spectral features, the D, G, and radical breath mode (RBM), act as the 'fingerprint' for carbon materials[77], it is used to determine lengths, electronic type (metallic or semiconducting), and whether nanotubes are separated or in bundle. Due to the coupling between electrons and phonons under exited condition, phonons or lattice vibrations provide a sensitive probe of the electronic. structure of SWNTs[78] The G band is the most intense peak in the Raman spectrum of bulk graphite. The G-band of carbon nanotubes is composed of several peaks appearing from the quantum confinement of the wave vector along the SWNT circumferential direction, and the folding of the graphite Brillouin zone into the SWNT Brillouin zone[79]. The D-band appears due to the presence defects, it depends on the laser energy and diameter of the SWNTs. A high intensity D-band compared to the G-band means the existence of amorphous carbon. The RBM is an entirely symmetric vibrational mode associated with the vibration of carbon atoms in a radial direction in relation to the nanotube axis. Theoretical and experimental results show that the RBM frequency (ω_{RBM}) is inversely proportional to the nanotube diameter[79, 80]. $\omega_{RBM} = \alpha/d_t$, theoretical α value was 232 ± 10 cm^{-1} based on density functional theory [81, 82],while the experimental single nanotube spectroscopy studies for SWNTs on the Si/SiO2 substrate, α is experimentally was 248 ± 2 cm^{-1} nm by the measurement of the RBM on a large number of isolated

semiconducting and metallic SWNTs. The Raman spectroscopy of P3DDT-HiPCO show from Fig 2.5 to Fig 2.7 with different resonance conditions. The spectra were collected from thin film samples using 532nm, 633nm and 785 nm excitation wavelength. The s-SWNT has various chirality. 532nm laser intensity the overlaps with S_{33} absorption for SWNT with large diameter (from 1.3nm to 1.7)[83]. P3DDT-HiPCO diameter is from 0.8 to 1.2 nm. The intensity of peaks for P3DDT-HiPCO in 532 nm was weak compared to 633nm, 785nm. The 633 nm laser can be excited metallic SWNT in RBM region from 100 to 230 cm^{-1}. The RBM of the spectra exited at 785 nm shows that P3DDT-HiPCO has a flat base line in the metallic region from 135 to 175 cm^{-1}. The base on UV-Vis-NIR absorption spectra and Raman spectroscopy. The purity of P3DDT-HiPCO is estimated over 99% based on the absorption spectra, Raman spectroscopy.

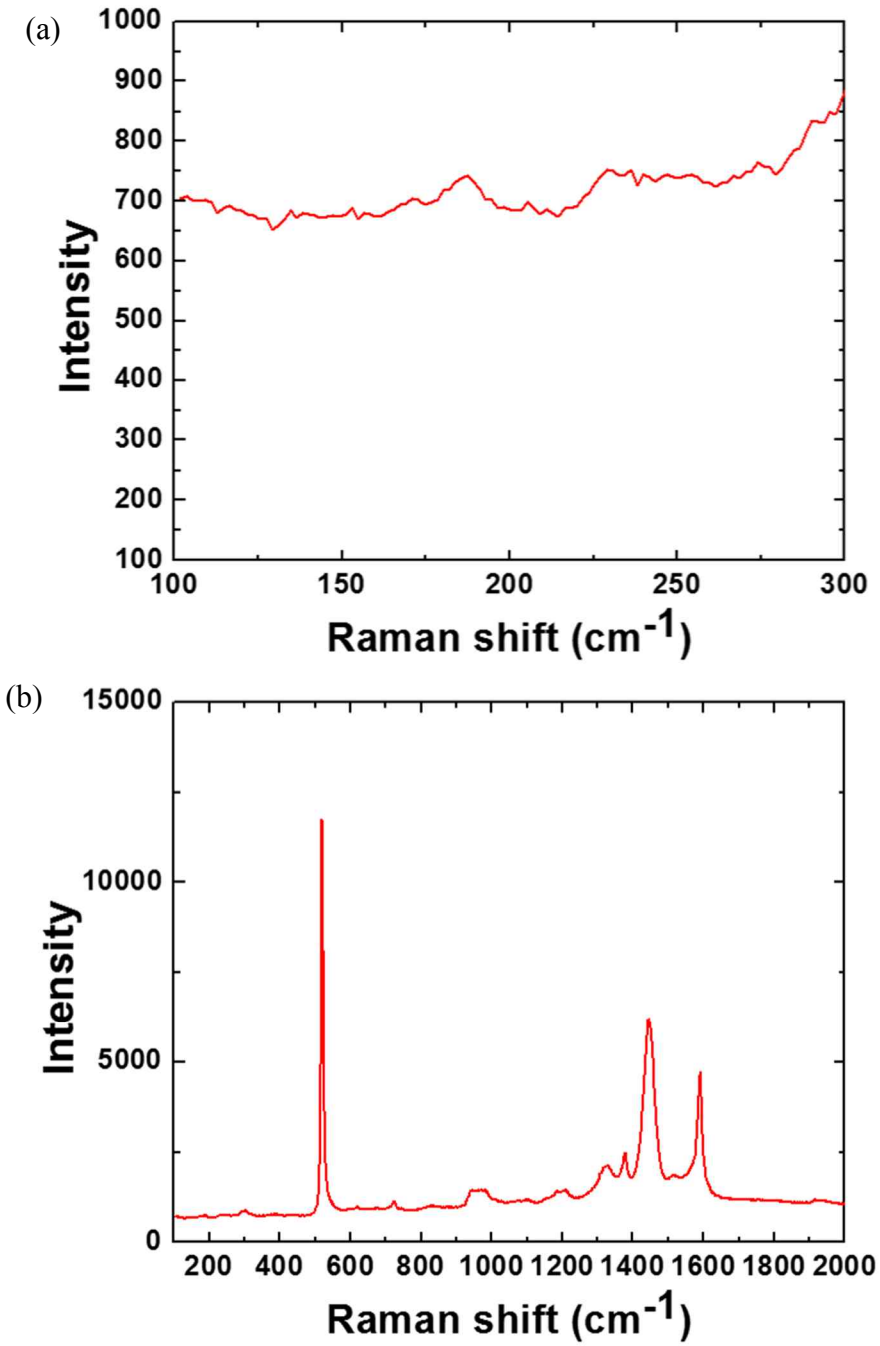

Fig.2. 5 Raman spectroscopy of P3DDT/HiPCO SWNT. RBM mode (a), G-mode (b) (excited at 532nm)

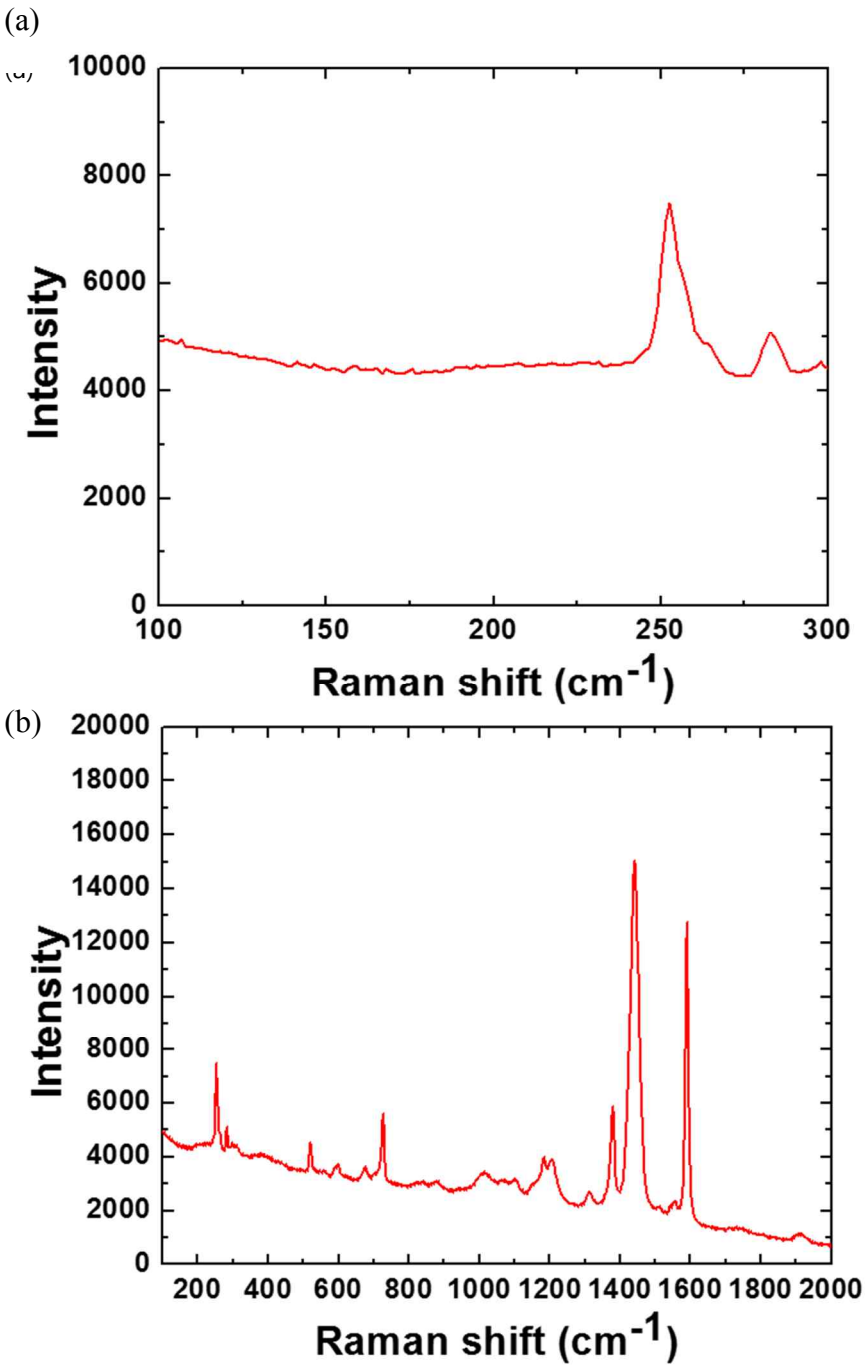

Fig.2. 6 Raman spectroscopy of P3DDT/HiPCO SWNT. RBM mode (a), G-mode (b) (excited at 633nm)

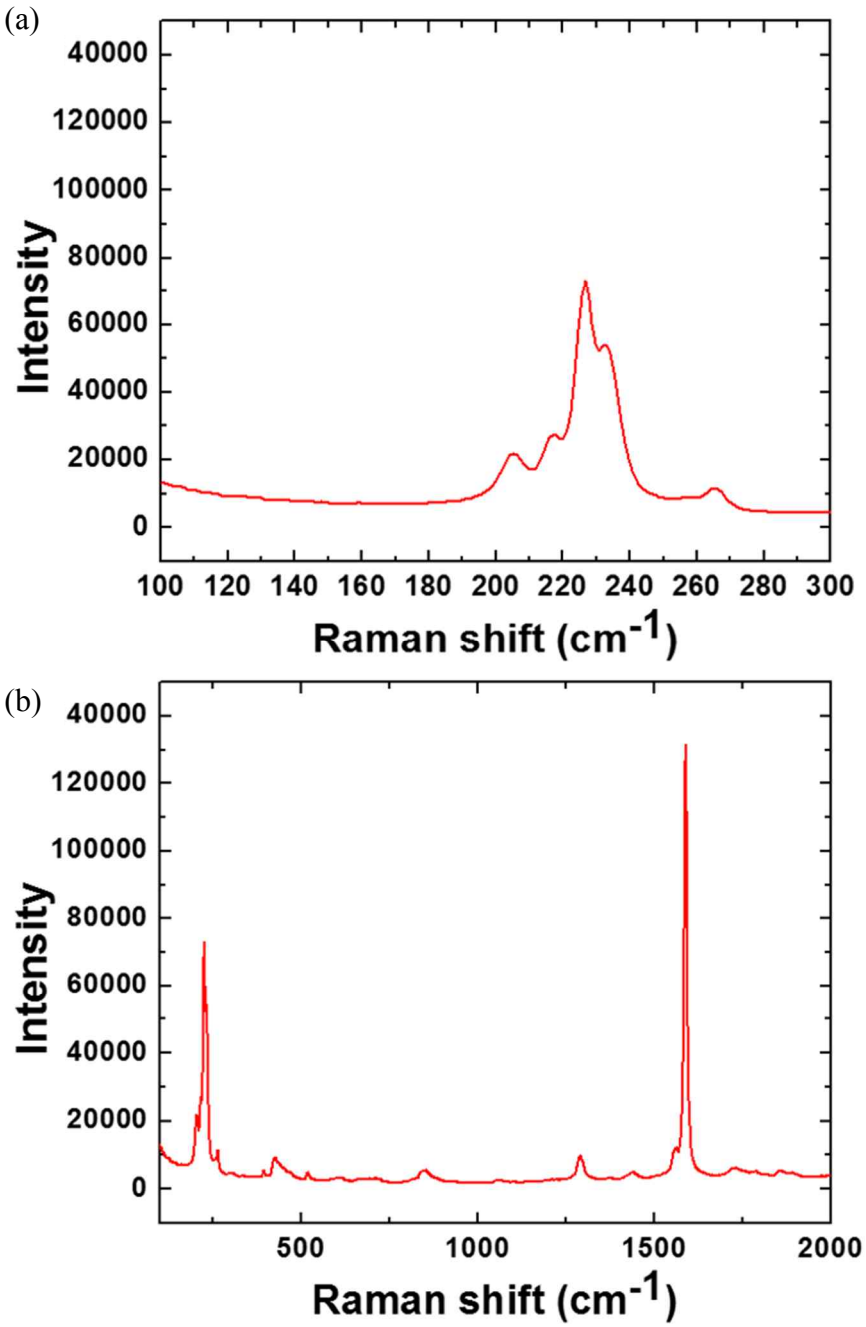

Fig.2. 7 Raman spectroscopy of P3DDT/HiPCO SWNT. RBM mode (a), G-mode (b) (excited at 785nm)

UV-Vis-NIR absorption spectra of PFDD-PD

Fig.2 8 shows the absorption spectrum of the PFDD-PD SWNTs, the absorption peak of PFDD appear strong crest at 380 nm, and s-SWNTs show three absorption bands in the regions of 1400-1900 nm for S11, 700-800 nm for S2, while P3DDT has a absorption peak in the region of 450-550 nm, These results are consistent with previously reported literatures[33]. We use the Beers-Lambert law (A=εlc) to correlate the peak absorbance (A) and the concentration of s-SWNTs (c in mg/mL) through the extinction coefficient (ε in mL/mg cm), where l is the path length in cm and is 1 cm in this work. The extinction coefficient of the PFDD-PD was 48 ml/mg cm[33]. PD type SWNTs concentration was 12.5ug/ml. The small crest at 646 nm and 699 nm in absorption spectrum of PFDD-PD solution indicate existence of metallic SWNT. In order to confirm the presence of the metallic SWNT, we have also conducted Raman spectroscopy measurement.

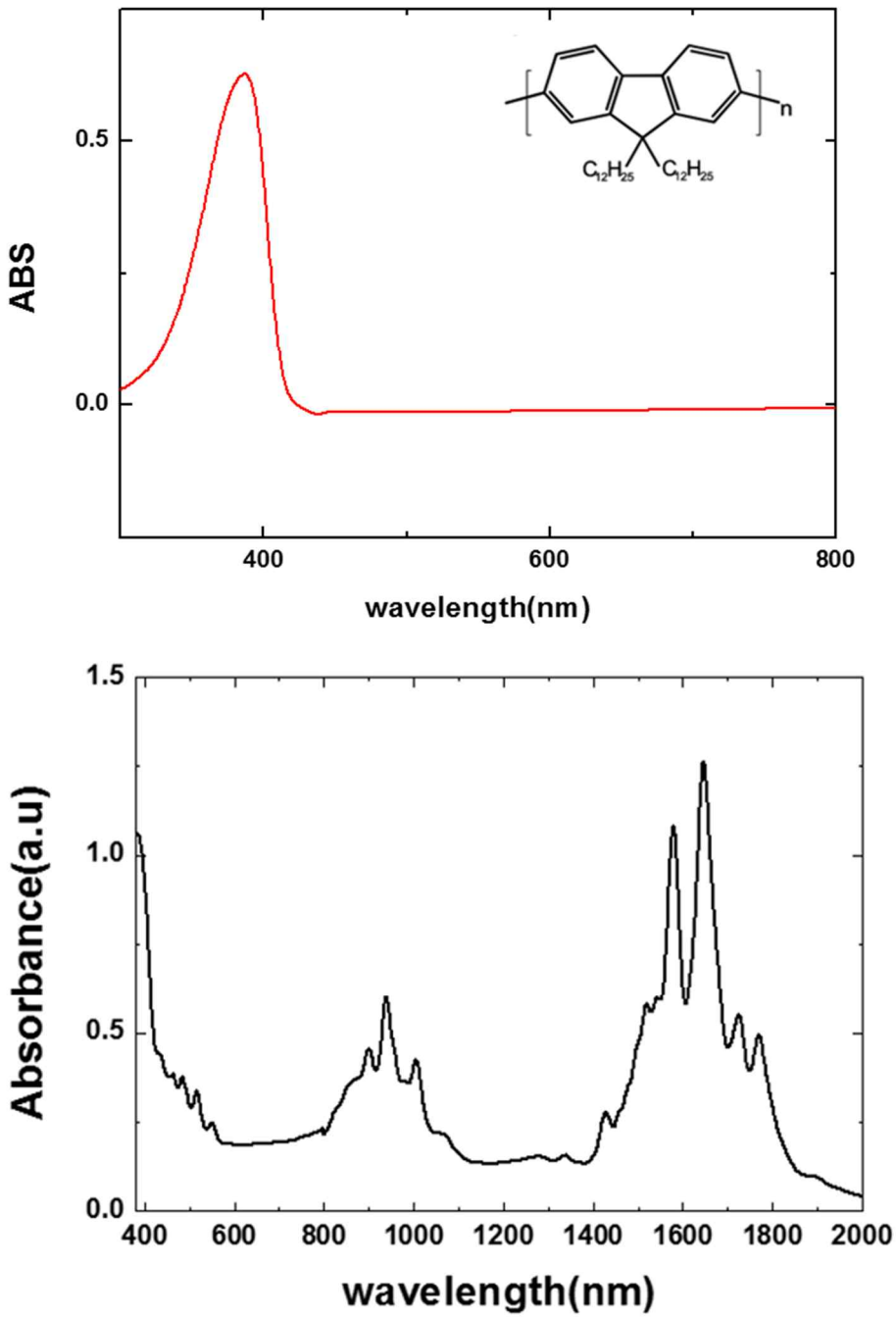

Fig.2. 8 Uv-vis spectroscopy of PFDD and PFDD/PD SWNT solutions

Raman spectroscopy of PFDD-PD

The Raman spectroscopy of PFDD-PD show from Fig 2.9 to Fig 2.11 with different resonance conditions. The spectra were collected from thin film samples using 532nm, 633nm and 785 nm excitation wavelength. The metallic SWNT peak appears at 135-170 cm^{-1}. We clearly observed crest in PFDD-PD solution in both of RBM mode. This result implies that PFDD-PD solution contains a certain amount of metallic SWNT after PFDD wrapping.

Semiconducting PFDD-PD purity evaluation by absorption peak ratio.

The s-SWNT purity is the important factor to determine the FET performance. The purity of PFDD-PD is evaluated by using comparison of the absorption peak ratio ($\phi = A_{CNT} / (A_{CNT}+A_B)$), A_{CNT} was the enveloping area of the M_{11} and S_{22} bands enclosed by the linear baseline in the region from 8400 to 16000 cm^{-1}, and A_B was the area covered by the linear baseline of the same region, which was suggested by previous papers. [33, 84, 85]. The absorption peak ratio for PFDD-PD was 0.396 indicating that estimated purity of s-SWNT in PFDD-PD ink was 98-99% [33].

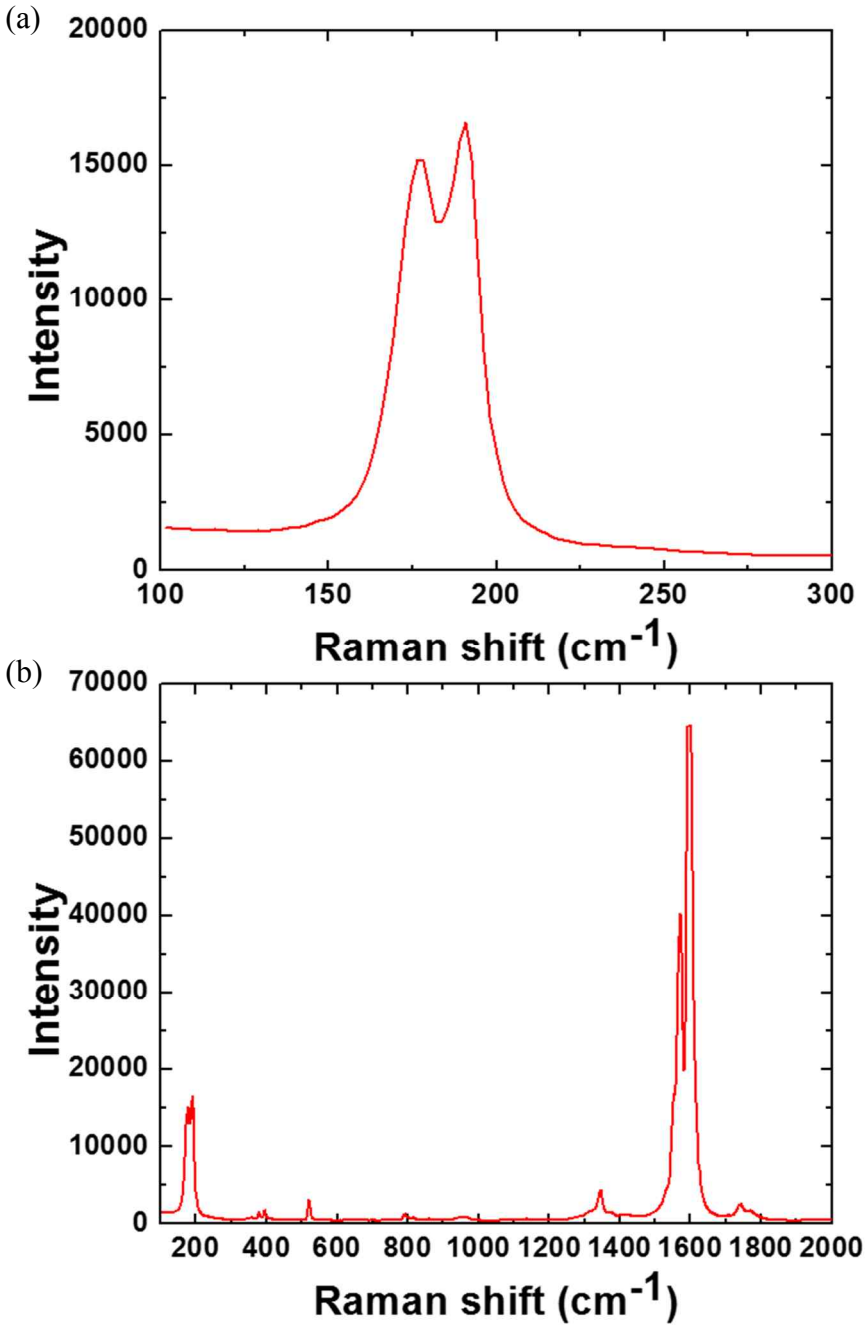

Fig.2. 9 Raman spectroscopy of PFDD/PD. RBM mode (a), G-mode (b) (excited at 532nm)

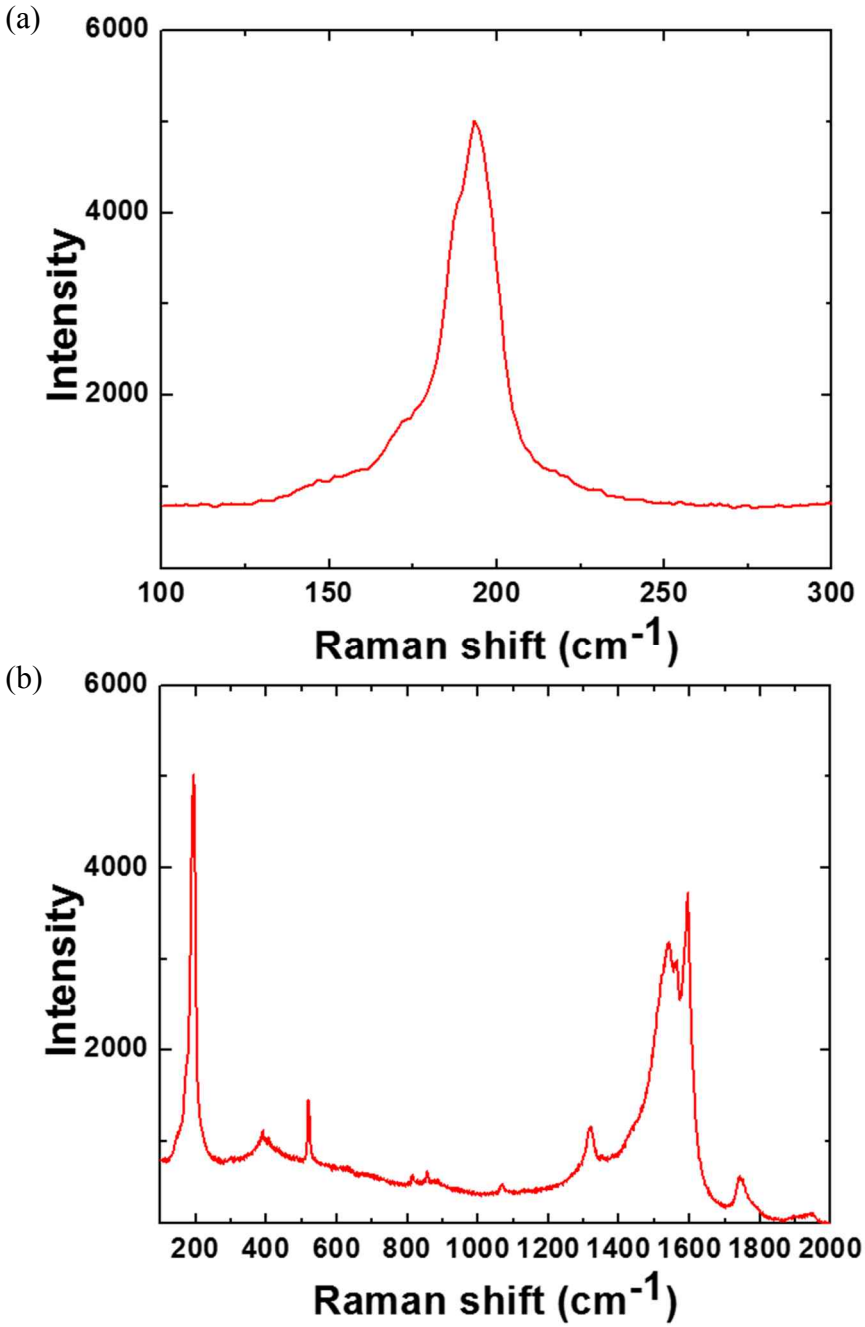

Fig.2. 10 Raman spectroscopy of PFDD/PD. RBM mode (a), G-mode (b) (excited at 633nm)

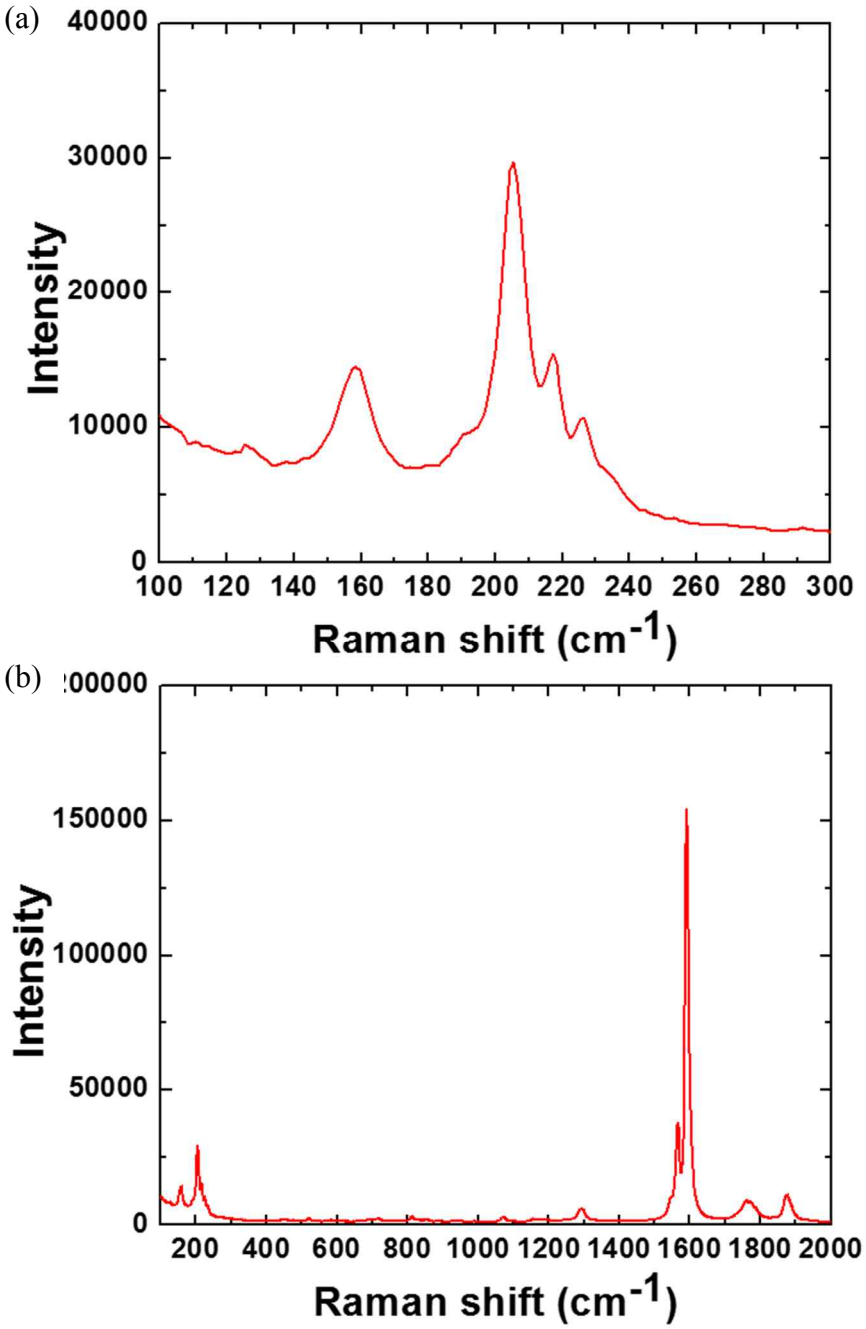

Fig.2. 11 Raman spectroscopy of PFDD/PD. RBM mode (a), G-mode (b) (excited at 785nm)

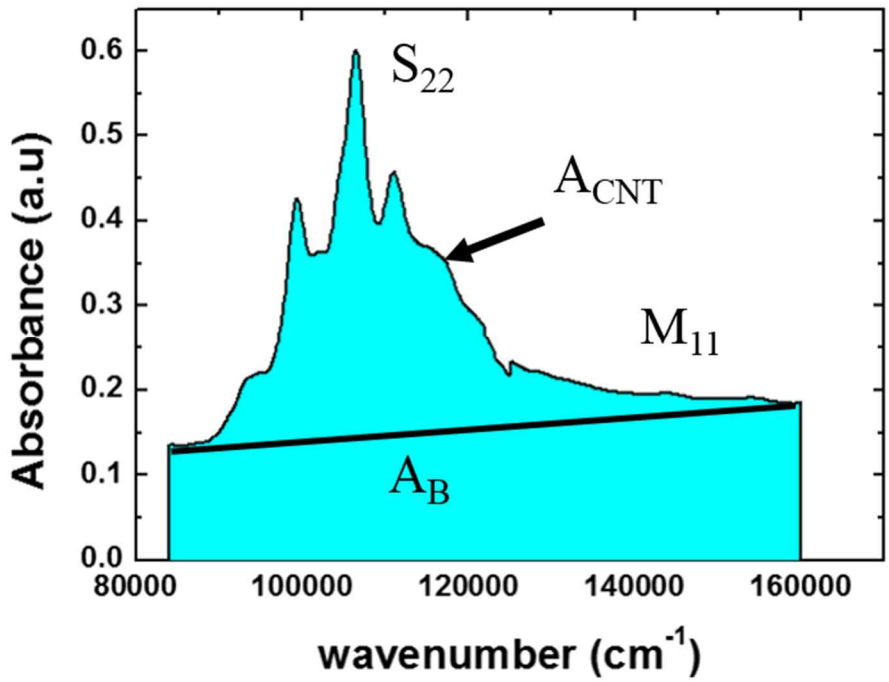

Fig.2. 12 Calculation of **Φ** values for PFDD-PD. (**Φ** $=A_{CNT}/ (A_{CNT}+A_B)$)

AFM and TEM of s- SWNT

Fig 2.13 illustrates the AFM morphology of the P3DDT-HiPCO, scanning region was 25 μm^2. The small particles are iron catalyst particles. The P3DDT-HiPCO was formed random network structure. The TEM (Fig 2.14) display h straight individual nanotubes. The length of the P3DDT-HiPCO is evaluated by AFM and TEM with the images. The length of the P3DDT-HiPCO was average 500 nm. AFM line profiles indicate that P3DDT-HiPCO height is 1-1.5 nm.

The AFM morphology of the PFDD-PD is shown in Fig 2.15, scanning region was 5 um ×5um. The PFDD-PD was also formed random network structure. The TEM (Fig 2.16) show straight individual nanotubes with few bundle. The length of the P3DDT-HiPCO is assessment by AFM and TEM with the images. The PFDD-PD length was average 2000 nm. AFM line profiles show that P3DDT-HiPCO height is 1.5-2 nm.

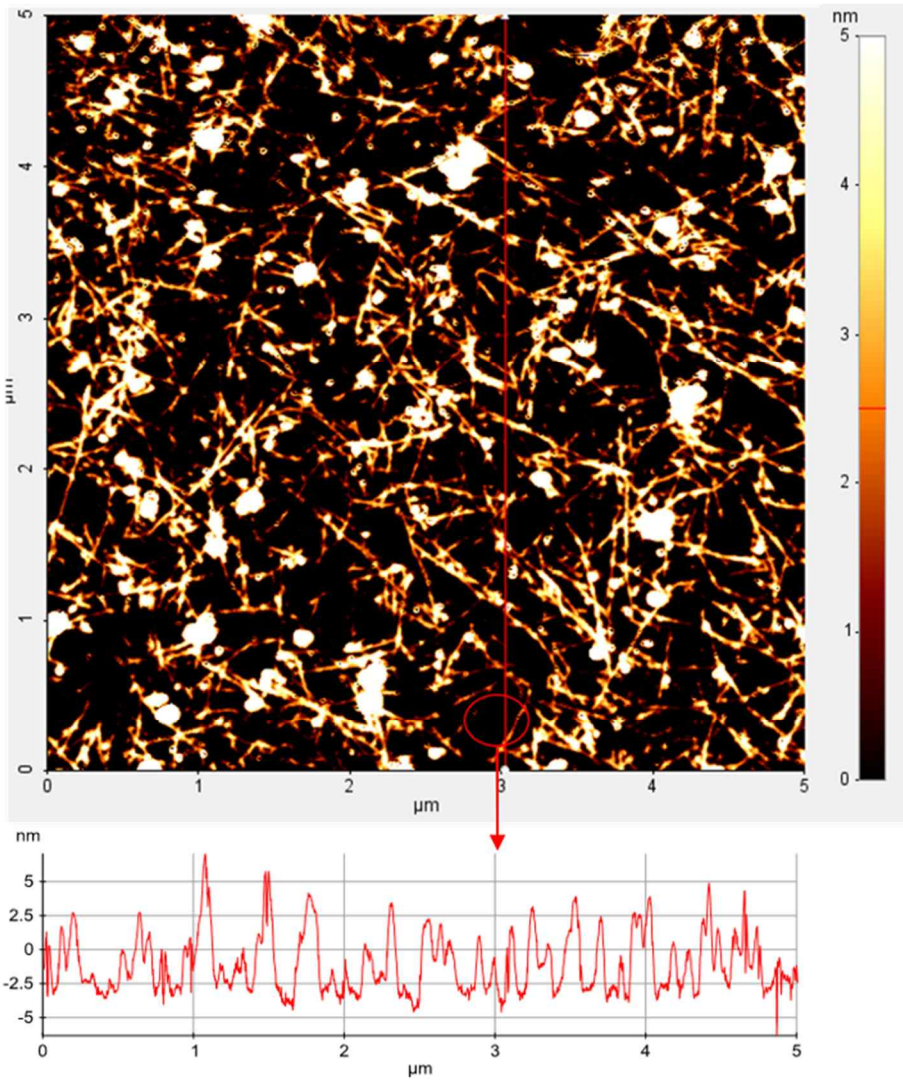

Fig.2. 13 AFM image and line profile of P3DDT-HiPCO

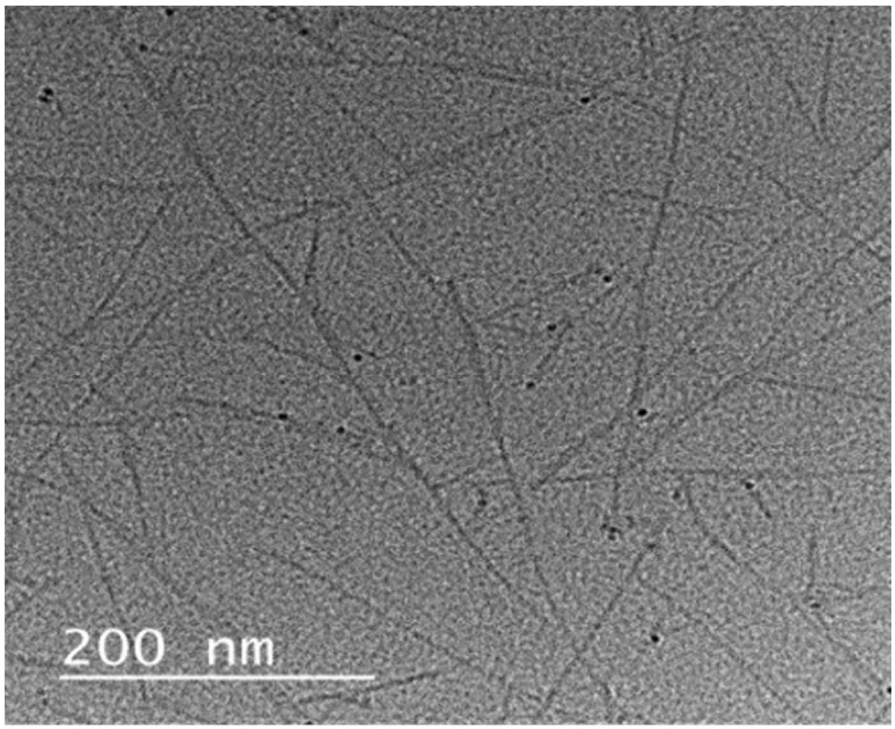

Fig.2. 14 TEM image of P3DDT-HiPCO (dropped on Cu grid)

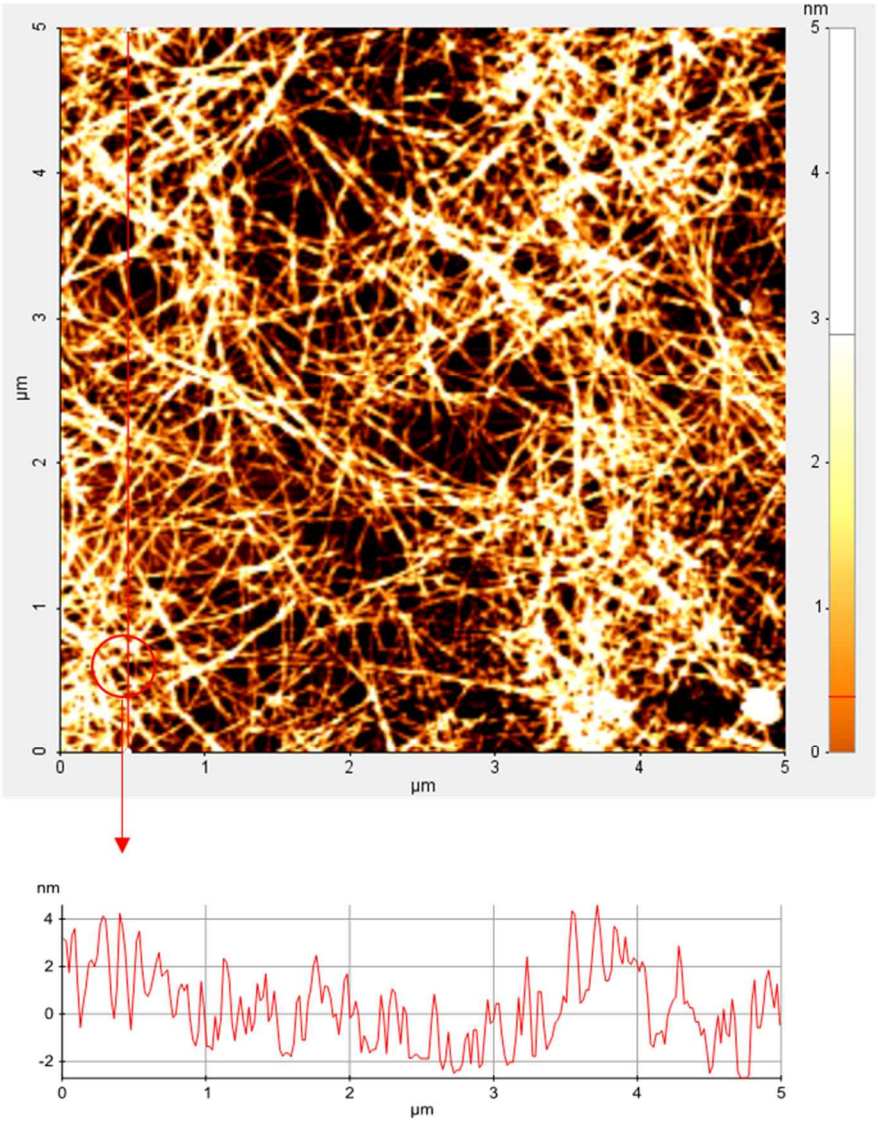

Fig.2. 15 AFM image and line profile of PFDD-PD

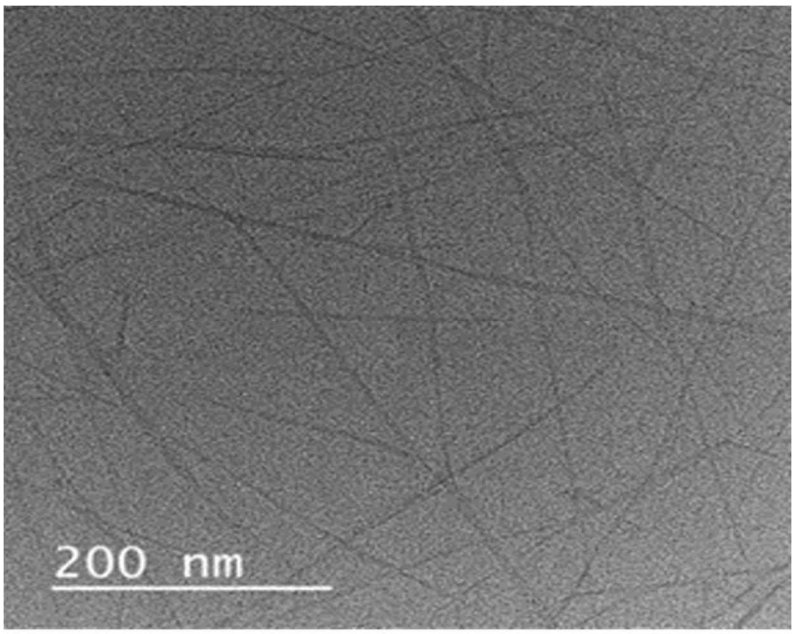

Fig.2. 16 TEM image of PFDD-PD SWNT solution

Summary

We have demonstrate the selection of s-SWNTs in SWNTs grown by HiPCO for PFO and P3DDT and PD for PFDD. The UV-vis-NIR absorption spectra of PFO-HiPCO and P3DDT-HiPCO show the intensity of the peaks s-SWNTs increases in the range between 1000 nm and 1500 nm. The purity of s-SWNTs in PFO-HiPCO, P3DDT-HiPCO sample is estimated over 99% based on the UV-vis-NIR absorption spectra, Raman spectroscopy and electrical parameters. UV-vis-NIR absorption spectra display the reduction of the polymer peaks under 400 nm (PFDD) for PFDD-PD. Raman spectra illustrates PFDD-PD contains a small amount of metallic SWNTs. The purity of PFDD-PD is evaluated by using comparison of the absorption peak ratio (98-99%). AFM morphology exhibits that the both s-SWNTs networks form well-percolated morphology.

Chapter 3 Semiconducting SWNTs Transistors

Introduction

Semiconducting single walled carbon nanotubes (s-SWNT) are one of most promising materials as active layer for various flexible and transparent optoelectronics and electronic devices such as field-effect transistors (FETs), infra-red light emitting diode [86], and photo sensors [87] because s-SWNTs are known to have high charge carrier mobility, robust chemical stability, excellent mechanical flexibility and transparency. [88-90] However, SWNTs have intrinsically a statistical mixture of about 1/3 metallic and 2/3 semiconducting nanotubes with a variety of diameters during synthesis process [91]. In order to apply s-SWNTs in the devices, a high purity and large scale sorting method of s-SWNT should be developed. There have been tremendous efforts to separate s-SWNTs from raw SWNT and recently a few methods such as density gradient ultracentrifugation (DGU) [92], gel chromatography [75], selective dispersion with DNA [93], and selective dispersion using conjugated polymers [37] showed high possibility. Among them, the method of wrapping a specific conjugated polymers on s-SWNTs is considered as the most commercially effective

method since s-SWNTs with a high purity can be easily separated at a high yield with potentially low manufacturing cost [33]. There are a few challenges to realize high performance FETs by using s-SWNTs including (1) analysis tools that can quantify the purity of s-SWNTs more than 99% should be developed; (2) A reliable printing or coating method should be developed to achieve optimal semiconducting film morphology with a high reproducibility for both high field-effect mobility and current on/off ratio.

We fabricated s-SWNTs thin film transistors by using high purity HiPCO and PD SWNT ink[94, 95]. The devices showed different electrical characteristic due to different physical properties (diameter, length). The P3DDT-HiPCO transistor shows high on/off ratio but low mobility, meanwhile the PFDD-PD exhibit high mobility with high off current level. A $FeCl_3$-doping hetero structure system was adopted to solve these challenges.

Experimental

Active layer patterning method

The s-SWNT TFT devices have a top-contact and bottom gate structure. The devices were fabricated on the thermally grown 100nm-thick SiO_2 on a heavily doped silicon wafer which works as the common gate electrode (Fig. 3.1(e)). The SiO_2 substrates were sequentially cleaned in an ultra-sonic bath with deionized water, acetone, and isopropanol for 10 min each. They were made with photo crosslinking polyimide meanwhile the gate dielectric material was synthesized in KRICK[27].

Polyimide (6mg/ml in cyclohexanone) dielectric layers were formed by spin-coating on SiO_2 substrate. The spin-coated films were then baked at 90 °C for 6 min and exposed to 365 nm UV light for cross-linked. Subsequently, the films were annealed on a hot plate at 90 °C for 10 min and 110 °C for 30 min.

Device fabrication

The s-SWNTs were then deposited by spin coating at 2000 rpm for 60s and the resulting films were annealed in glove box at 90°C for 30 min. The exposed polyimide was developed with cyclohexanone, acetone, and isopropyl alcohol for 10 sec and annealed on a hot plate at 110 °C for 30 min to remove residual solvent

and moisture. S/D electrodes were patterned on the films using a metal shadow mask.

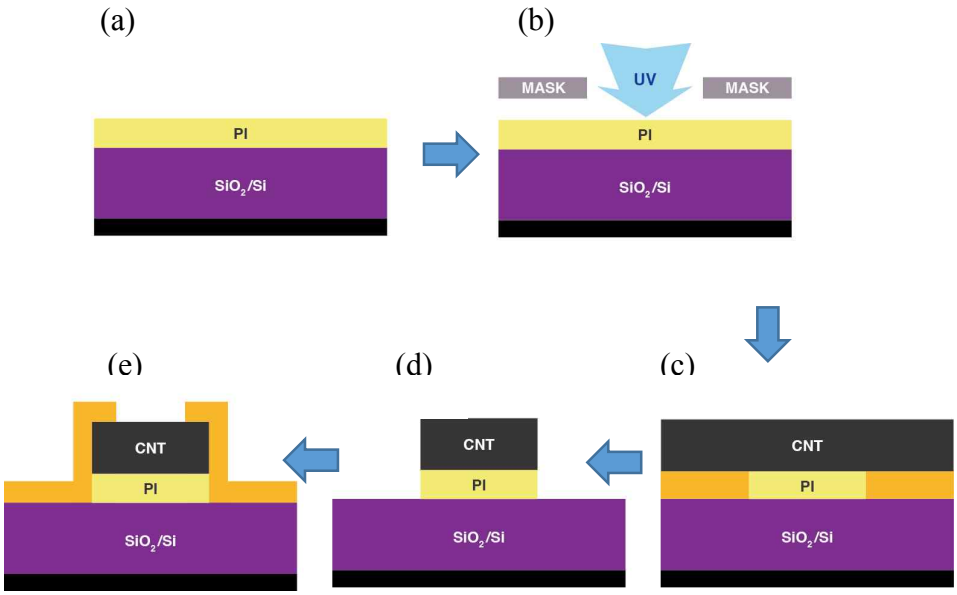

Fig. 3. 1 Process of active layer patterning (a) PI spin coating (b) mask aligning (c) SWNT coating (d) developing (e) Au electrode deposition

Au source and drain electrode were deposited by thermal evaporation under a pressure of 4.0 x 10^{-6} torr with the deposition rate of 0.5 Å/s. Fig.3.1 shows process of active layer patterning, we used parallel structure dielectric layer of PI and SiO_2/Si.

Characterization

To obtain the precise dielectric capacitance per unit area of the bilayer dielectrics, to measure dielectric constant, capacitance–voltage (C–V) measurements on the metal–insulator–metal (MIM) structure were performed, Polyimide (6mg/ml in cyclohexanone) dielectric layers were formed by spin-coating on SiO_2 substrate. (Fig.3.2) The capacitance values of the dielectrics were measured utilizing a Keithley 4200-SCS connected with an Agilent 4284A LCR meter. Electrical measurements were performed using a Keithley 4200-SCS instrument in a nitrogen-filled glove box

(a)

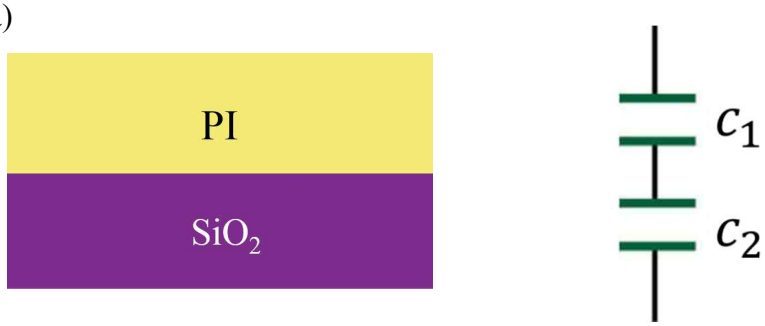

(b)

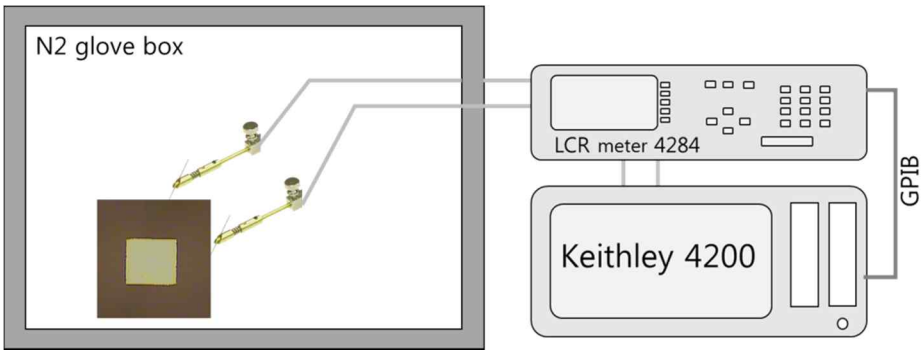

Fig. 3. 2 (a) Parallel structure of bilayer dielectric with the capacitance values of the dielectrics measured using a (b) Keithley 4200-SCS connected with an Agilent 4284A LCR in a glove box

Result and discussion

Dielectrics characterization

To obtain the precise dielectric capacitance per unit area of the bilayer dielectrics, to measure dielectric constant, capacitance–voltage (C–V) measurements on the metal–insulator–metal (MIM) structure were performed, Polyimide (6mg/ml in cyclohexanone) dielectric layers were formed by spin-coating on SiO_2 substrate. (Fig.3.2). Fig. 3.3 show result of the capacitance-voltage. The measured capacitance was 5.8 nF/cm^2 at 10 kHz. We used the equation

$$C = \epsilon_r \epsilon_0 / d$$

Where C is capacitance value evaluated by capacitance-voltage (C-V) measurements. ϵ_0 is the permittivity of a vacuum (≈ 8.854×10^{-12} Fm), ϵ_r is material's dielectric constant, Polyimide's dielectric constant is 2.8, SiO_2 is 3.9, d is dielectric layer's thickness, PI is 350 nm, SiO_2 is 100nm

$$\frac{1}{c} = \frac{1}{c_1} + \frac{1}{c_2}$$

ε_0=8.854x10^{-12} F/m $\quad$ $\varepsilon_{r\text{-polyimide}}$=2.8 $\quad$ $\varepsilon_{r\text{-SiO2}}$=3.9

$$\frac{1}{5.8} = \frac{1}{7} + \frac{1}{34.5}$$

the calculated results match the existing data for this device.

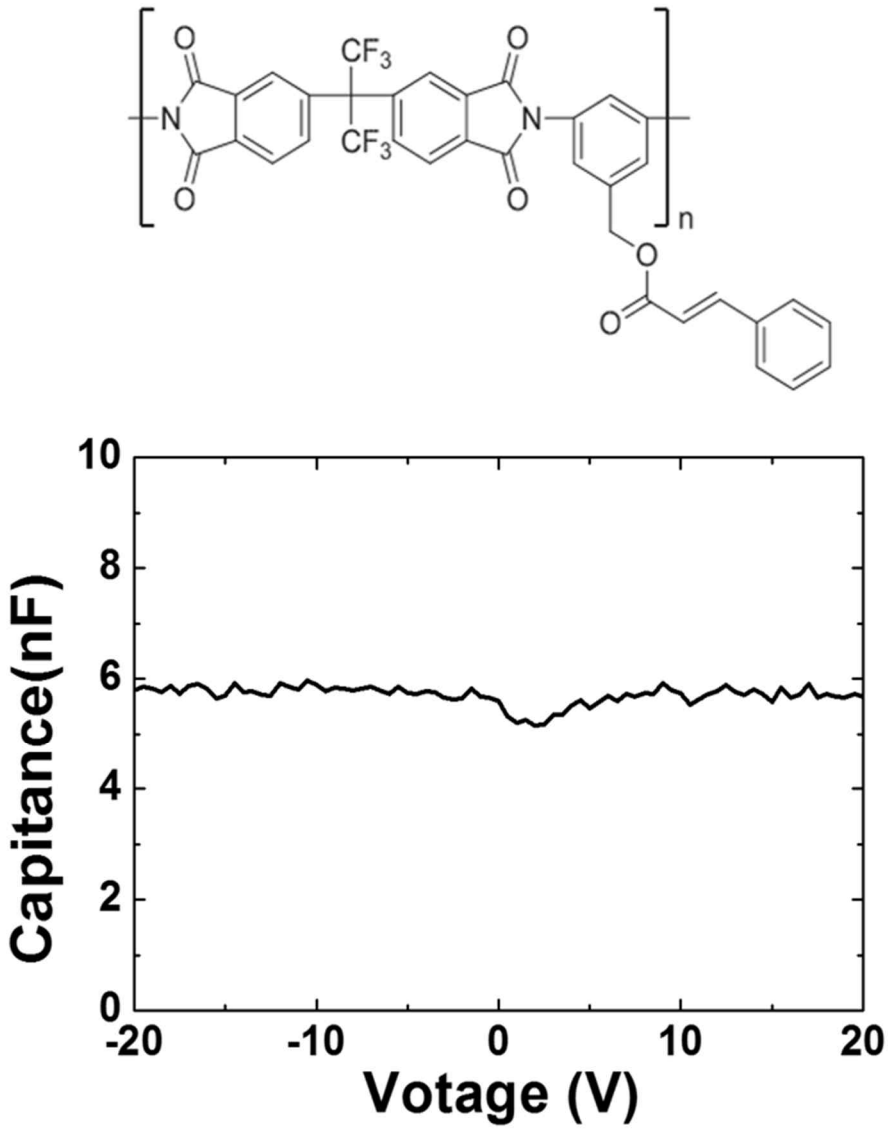

Fig. 3. 3 The chemical structure of the photo sensitive polyimide (K-PSPI-6F) [96], the capacitance-voltage characteristics of parallel-structured dielectric layer (PI and SiO_2).

In order to confirm the channel length and width, we use SEM image as shown in Fig 3.4. The channel length is 97 um and width is 1002um. We use magnetic pad to hold the substrate on the mask, but as there's small Au diffusion, the length becomes 3% shorter. Fig. 3.5 shows the transfer curves of the SWNT transistor with and without active layer pattern. When measuring the current- voltage sweep, we noticed a high leakage (black line) in the non-patterned device, meanwhile for the patterned one the leakage was under 10^{-11} A level. In order to device reliability, the active layer patterning is essential.

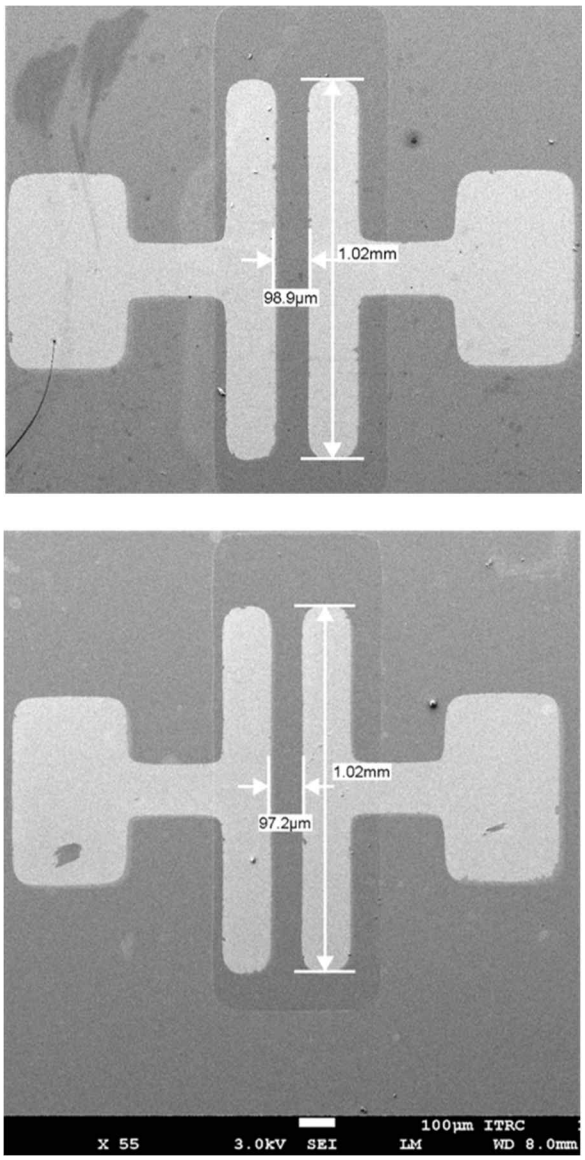

Fig. 3. 4 SEM image of the patterned device.

(a)

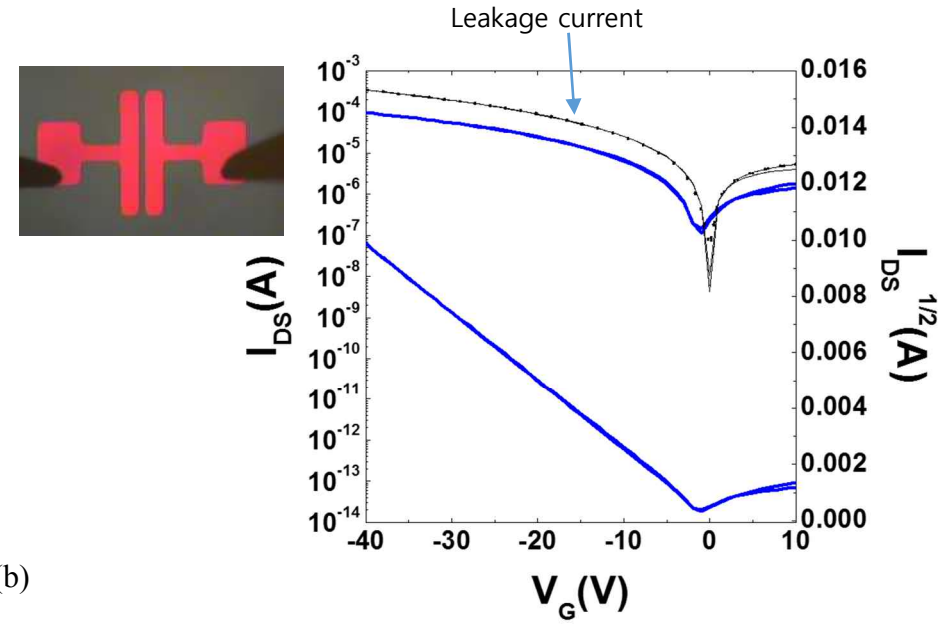

(b)

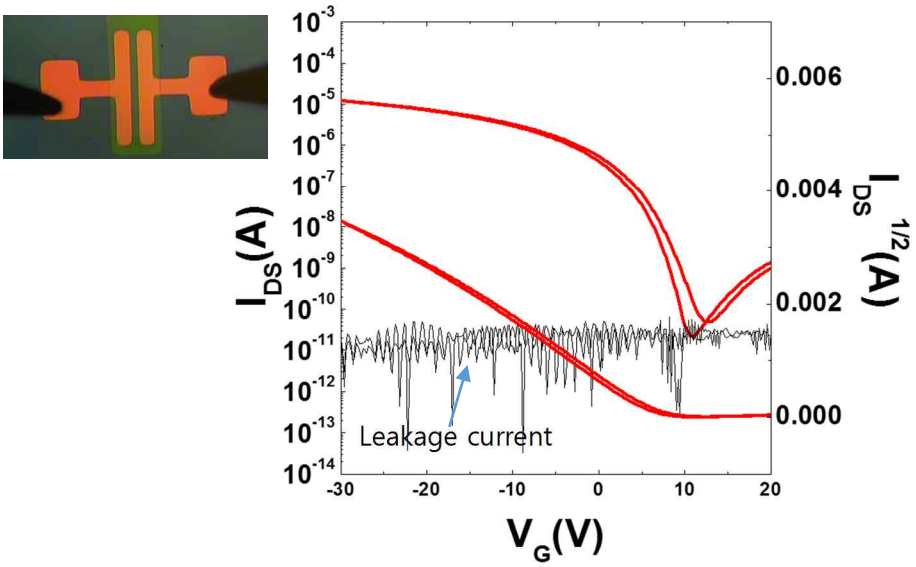

Fig. 3. 5 Transfer curves of unpattern (a) and patterned device (b). The Black line means leakage current.

Electrical characteristics of P3DDT-HiPCO and PFDD-PD.

To investigate the difference in the electrical characteristics of the FET according to purity, a single layer P3DDT-HiPCO and PFDD-PD was fabricated by spin coating method. Transfer characteristics of the SWNT FETs are shown in Figure 3.6. The FETs with P3DDT-HiPCO single layer showed the field effect mobility of $0.173\pm0.027 cm^2V^{-1}s^{-1}$, on/off ratio of 1.4×10^6 and off state current of 2×10^{-12} A, whereas PFDD-PD FETs exhibited a relatively high hole mobility of 6.7 ± 0.8 cm^2 $V^{-1}s^{-1}$, low on/off ratio of 2.4×10^4 and high off state current of 2.3×10^{-9} A. The transfer curve of P3DDT-HiPCO exhibit unipolar hole transport in this study. According to previously reported literatures, SWNT transistors shows ambipolar behavior[42, 97], or unipolar behavior depending on the dielectric materials used[98]. PI has 6 fluorine atoms per monomer. The fluorine is a strong electron-withdrawing atom [99]. Presumably PI acts as electron trap site at the interface with SWNT as shown in Figure 3.7. The device based on high purity P3DDT-HiPCO has long channel length (100 um). That's why the off current in P3DDT-HIPCO transistors is much lower. PFDD-PD has longer length than P3DDT-HiPCO. The length of the SWNT is important parameter in the efficiency of charge transport through the network [100]. The longer SWNTs show better optoelectronic performances [101].

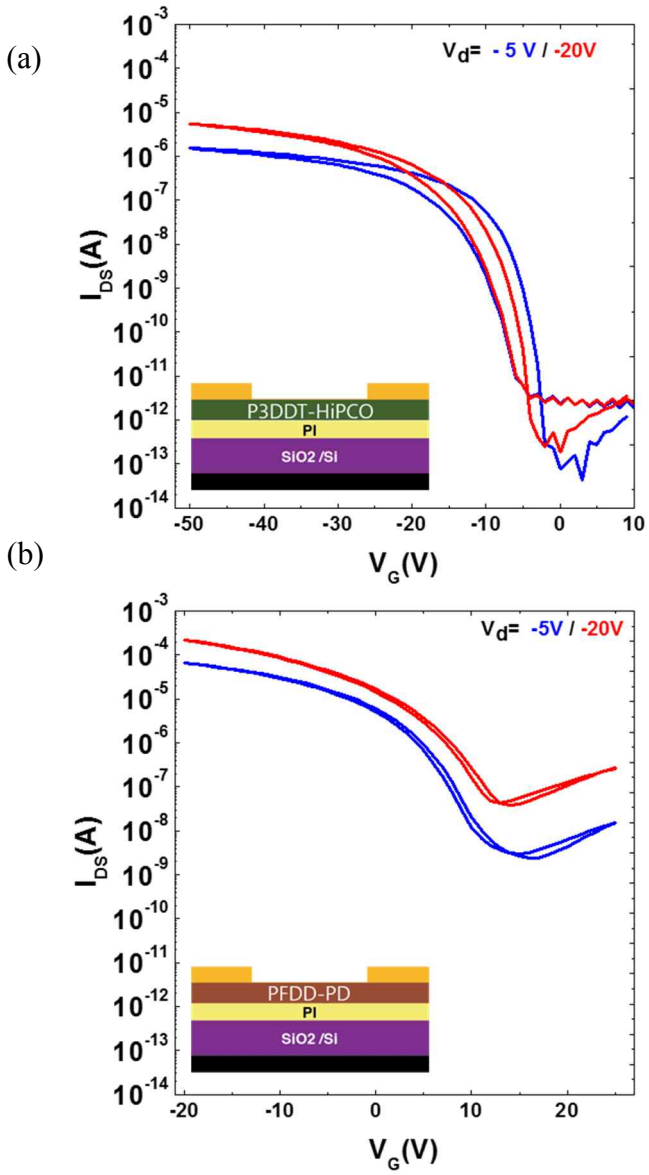

Fig. 3. 6 Transfer curves of P3DDT-HiPCO transistors (a) and PFDD-PD transistors (b), the insets depict the transistors' structures (100um channel length and 1mm channel width)

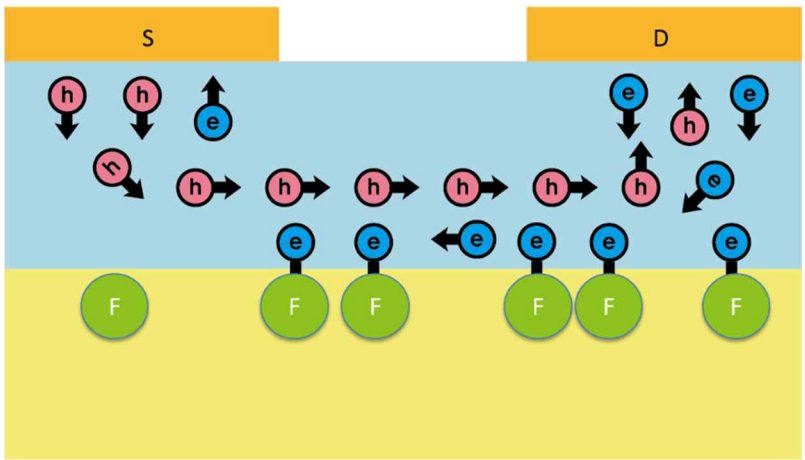

Fig. 3. 7 Schematic of charge trap mechanism

Figure 3. 8 show AFM of P3DDT-HiPCO and PFDD-PF in channel region. The P3DDT-HiPCO length was average 500 nm whereas he PFDD-PD length The PFDD-PD length was average 2000 nm. They show SWNTs networks form well-percolated image. White spots indicate the metal catalysts. AFM analysis program showed that P3DDT-HiPCO film height is under 1.5nm and PFDD-PD is 2nm

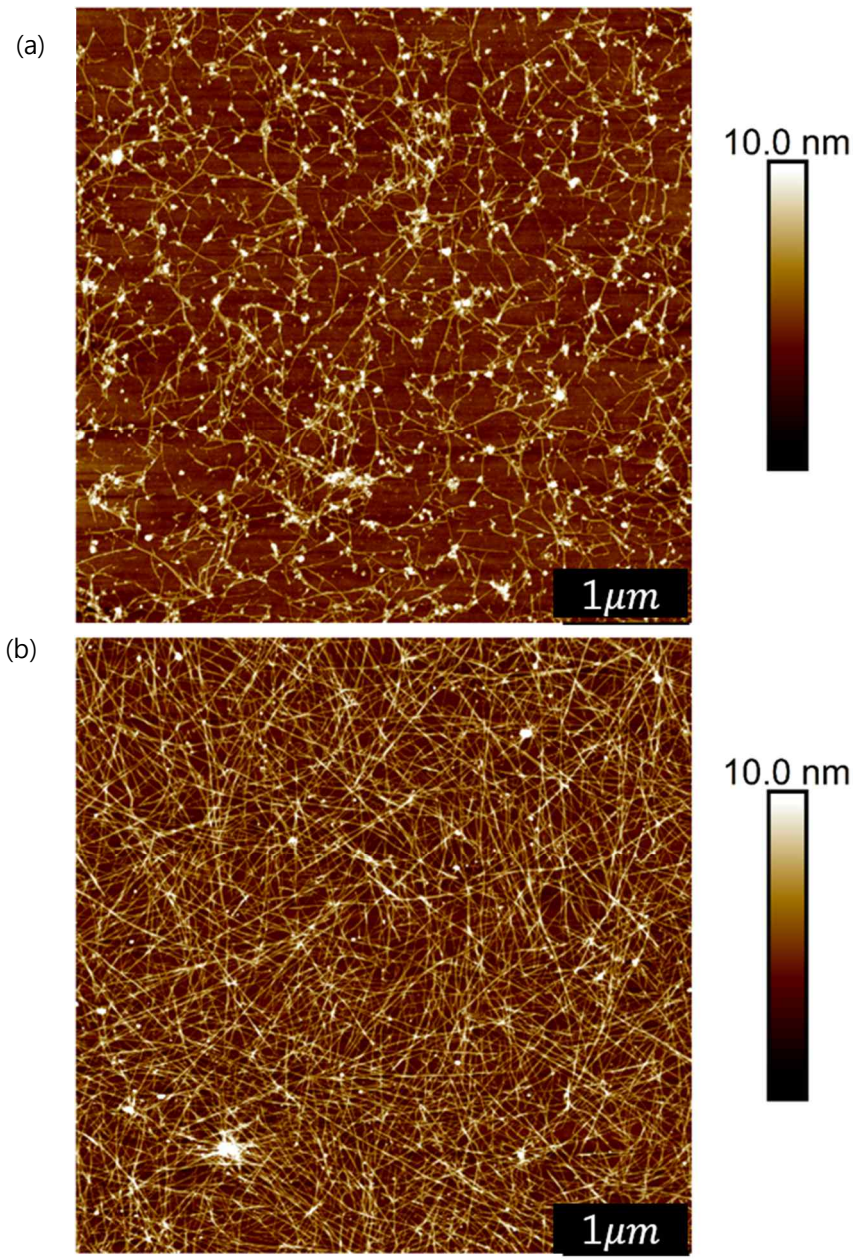

Fig. 3. 8 AFM images of P3DDT-HiPCO (a) and PFDD-PD (b)

Output characteristics of P3DDT-HiPCO is shown in Fig 3.9. There is no current clouding at the low drain voltages, indicating good ohmic behavior, contact resistance was calculated 20 kΩcm the Y-function method[102]. Figure 3.10 show ambipolar characteristics for PFDD-PD. Larger diameter SWNTs show a larger on state current and large off state current due to the smaller band gap [34].Since the band gap is so small, holes and electrons can be injected into the channel simultaneously. Also, the high mobility and low on/off ratio of PFDD-PD device is due to the less SWNT purity in PFDD-PD. The residual metallic nanotubes of PFDD-PD can form pathways across the channel leading to high mobility and low on/off current ratios [39, 40, 103]. The residual metallic nanotubes in PFDD-PD has high conductivity (R_c = 1 kΩcm) and high off state current so it is not to suitable to apply as an active layer whereas high purity P3DDT-HiPCO shows low off current state current but has relatively high contact resistance.

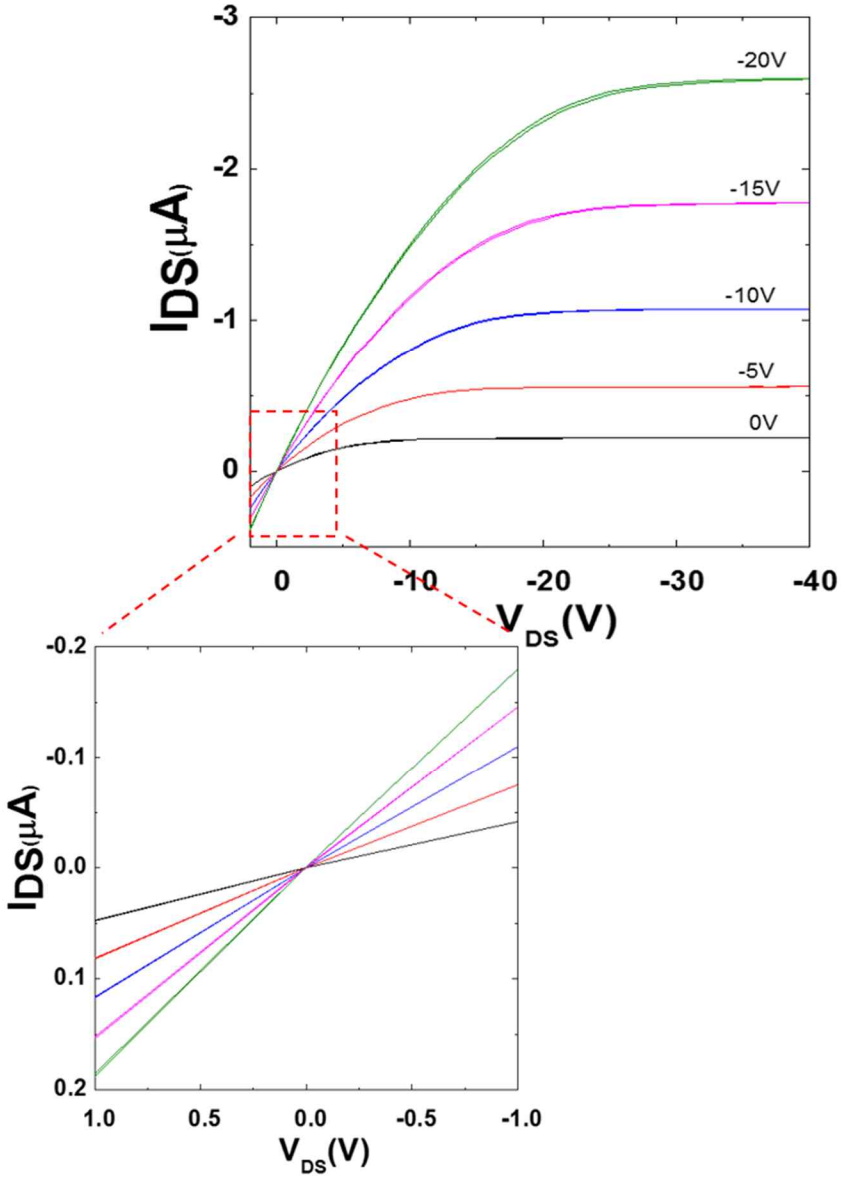

Fig. 3. 9 Output characteristics of P3DDT-HiPCO transistors.

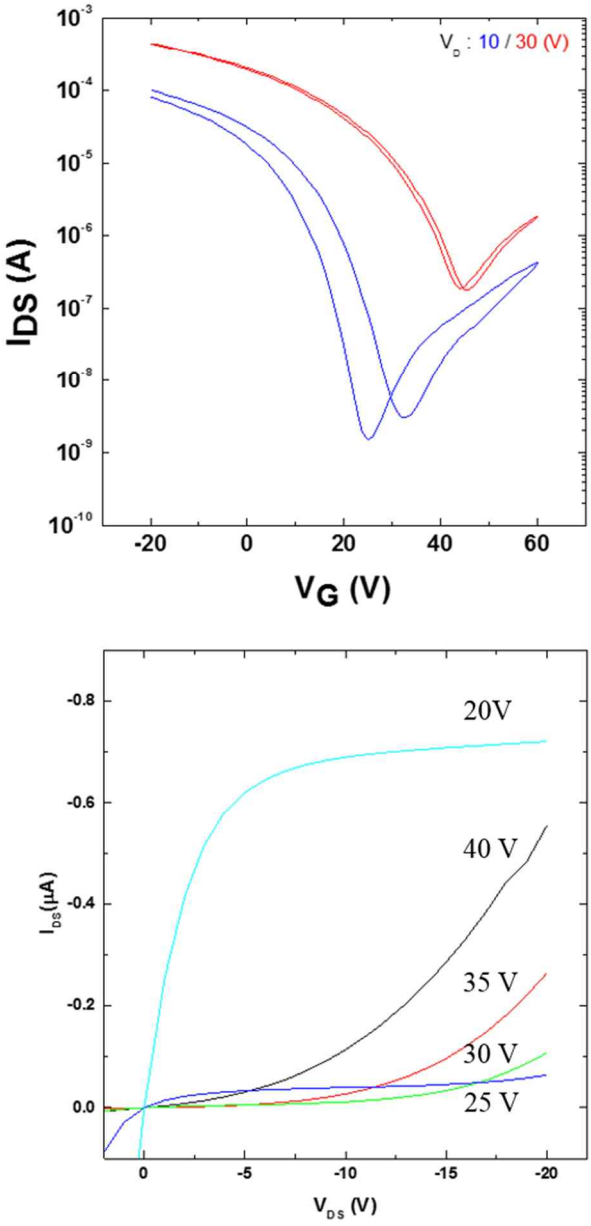

Fig. 3. 10 Ambipolar characteristics of PFDD-PD transistors. (100um channel length and 1mm channel width)

From a point of view of FET application, it's necessary to get high mobility with high on-off ratio. Yet, in the field of SWNT research, high mobility always compromises on/off ratio. To combine the advantage of the two SWNTs, the low off state current of P3DDT-HIPCO and the high conductivity of PFDD-PD, we applied P3DDT-HiPCO as a channel layer and PFDD-PD as injection layer to obtain optimal charge injection and transport property using solution process. Bilayer can provide this functionality in top gate bottom contact geometry. In Figure 3.11 exhibits transfer characteristics of the two different type hetero structure transistors. P3DDT-HIPCO/PFDD-PD/PI transistors exhibit the hole mobility of 1.75 ± 0.55 $cm^2/ V^{-1}s^{-1}$, on/off ratio of 4.4×10^4 and off state current of 1.15×10^{-9} A. PFDD-PD/P3DDT-HiPCO/PI transistors show the hole mobility of 6.18 ± 0.87 $cm^2/ V^{-1}s^{-1}$, on/off ratio of 1.4×10^7 and off state current of 3.4×10^{-12} A. The hetero structure (PFDD-PD/P3DDT-HiPCO/PI dielectric) transistors exhibit high mobility similar to that of PFDD-PD device and low off current similar to that of P3DDT-HiPCO devices. PFDD-PD layers act as charge injection layer to enhance injection of holes and electrons. Meanwhile, P3DDT-HiPCO layers act as a charge transport layer. The hetero structure (PFDD-PD/P3DDT-HiPCO/PI dielectric) exhibit high mobility with high on/off ratio.

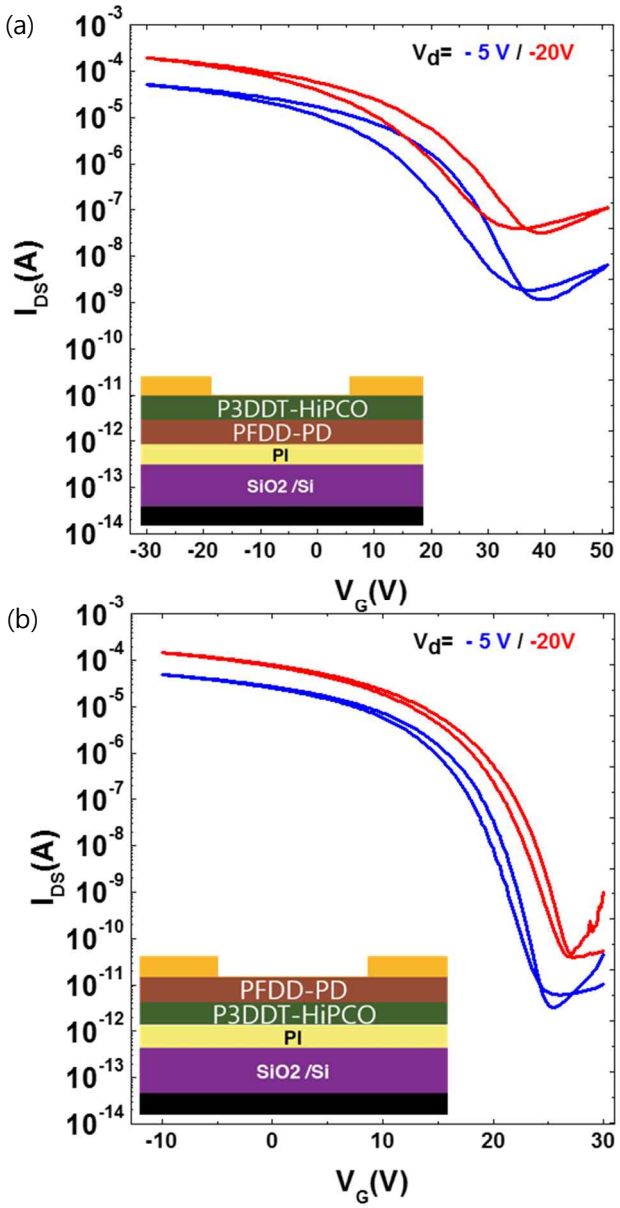

Fig. 3. 11 Transfer curves of P3DDT-HiPCO/PFDD-PD/PI transistors (a) and P3DDT-HiPCO/PFDD-PD/PI transistors (b), the insets depict the transistors' structures (100um channel length and 1mm channel width)

The mobility and off state current properties of hetero structure FETs were governed by top and bottom layers, respectively. The off state current is different depending on the SWNTs type deposited on the dielectric layer.

Fig 3.12 shows AFM image of P3DDT-HiPCO/PFDD-PD/PI and PFDD-PD/P3DDT-HiPCO/PI SWNT. Both SWNTs film form random network. To confirm dispersion quality of the SWNT film, we conducted Raman mapping measurement in which a laser beam (785nm source) spot was scanned 56μm×56μm in the channel region. Figure 3.13 shows raw data image of PFDD-PD and P3DDT-HiPCO (blue) obtained from Raman mapping measurement. The results show both SWNTs are well dispersed in the channel region and highly connected. Table 1 and Fig 3.14 summarizes electrical parameters for the four differently structured transistors.

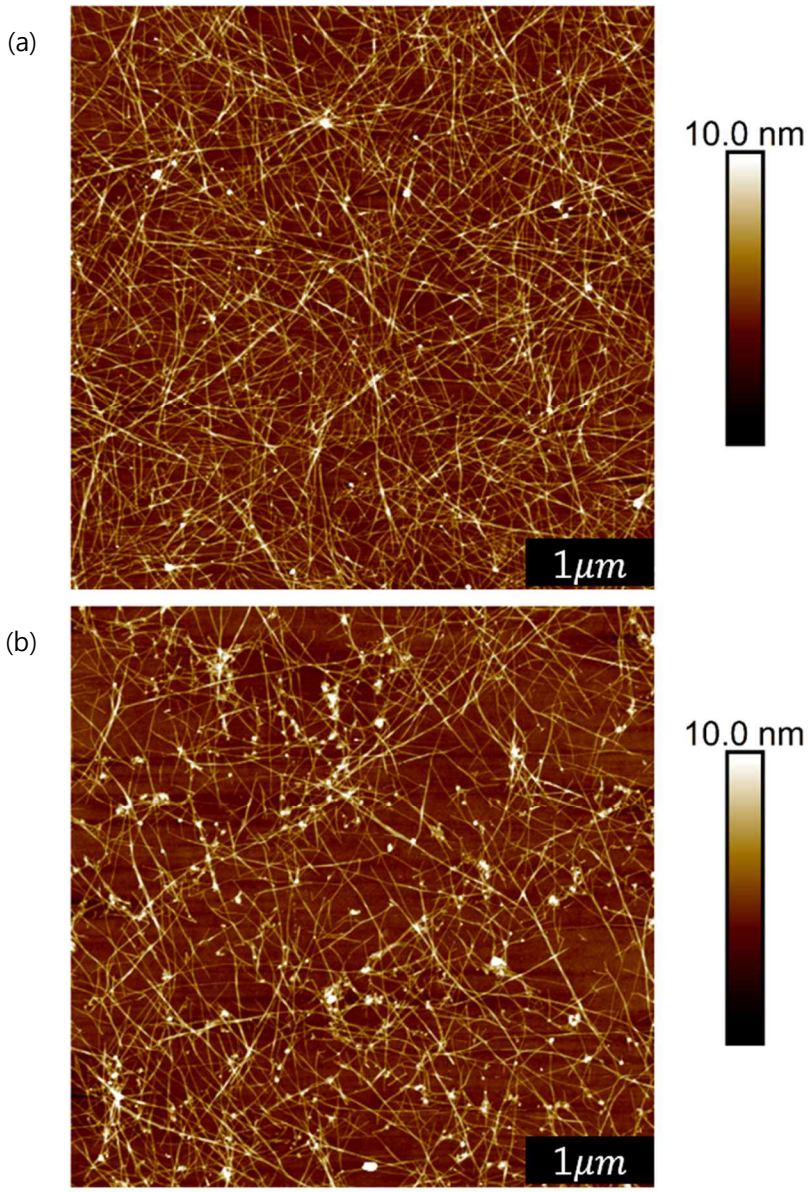

Fig. 3. 12 AFM images of P3DDT-HiPCO/PFDD-PD (a) and PFDD-PD/P3DDT-HiPCO (b)

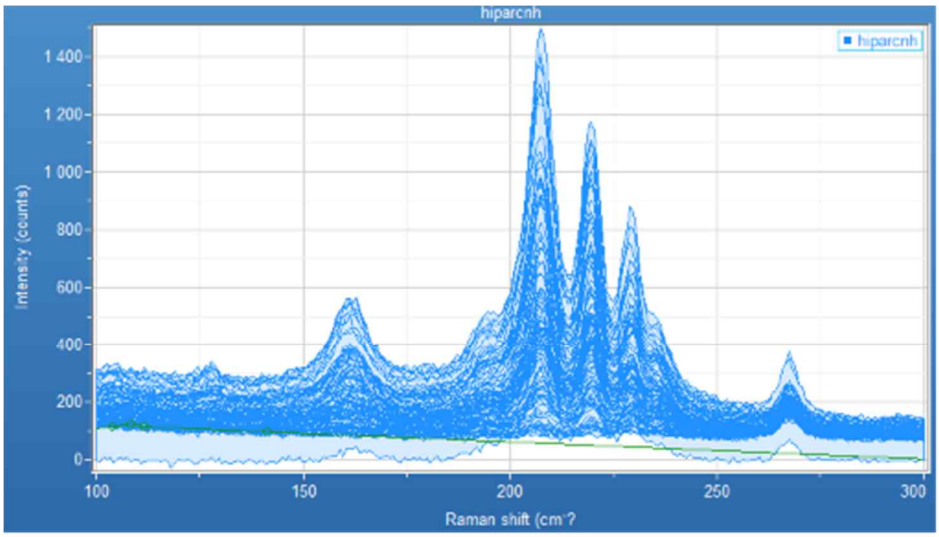

(a) (b)

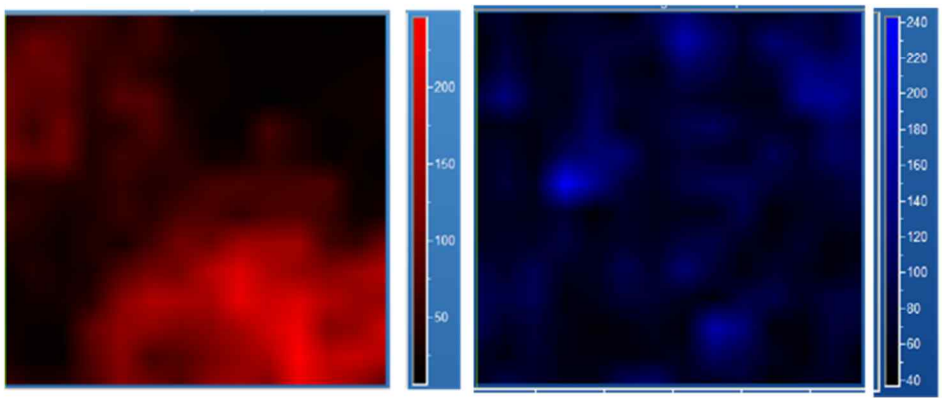

Fig. 3. 13 Raw data images of PFDD-PD (a) P3DDT-HiPCO (b) from Raman mapping measurement (56μm × 56μm)

Table 1. Eelectrical parameters of the SWNT FETs. The mobility were calculated by the standard formulation in linear (V_d = -5V) and saturation region (V_d= -20V). The contact resistance (R_c) is evaluated by the Y-function method[102]

Structure	Saturation		Linear				
	μ ($cm^2V^{-1}s^{-1}$)	V_{th} (V)	μ ($cm^2V^{-1}s^{-1}$)	V_{th} (V)	Off state current (A)	On/off ratio	R_c (kΩcm)
P3DD-HiPCO	Max 0.2 0.173±0.027	-10 (-6)	Max 0.08 0.045±0.035	-5 (-11)	2×10^{-12} $\sim10^{-12}$	1.4×10^{6} $\sim10^{-6}$	20
PFDD-PD	Max 7.5 6.7±0.8	8 (12)	Max 2.3 1.725±0.575	6 (8)	2.3×10^{-9} (10^{-8}~10^{-9})	2.4×10^{4} $\sim10^{-4}$	1.0
P3DDT-HiPCO /PFDD-PD/PI	Max 2.3 1.75±0.55	25 (30)	Max 0.4 0.25±0.15	18 (22)	1.15×10^{-9} (10^{-8}~10^{-9})	4.4×10^{4} $\sim10^{-4}$	1.5
PFDD-PD /P3DDT-HiPCO/PI	Max 7.08 6.18±0.87	9 (16)	Max 0.6 0.415±0.145	7 (15)	3.4×10^{-12} $\sim10^{-12}$	1.4×10^{7} $\sim10^{7}$	1.6

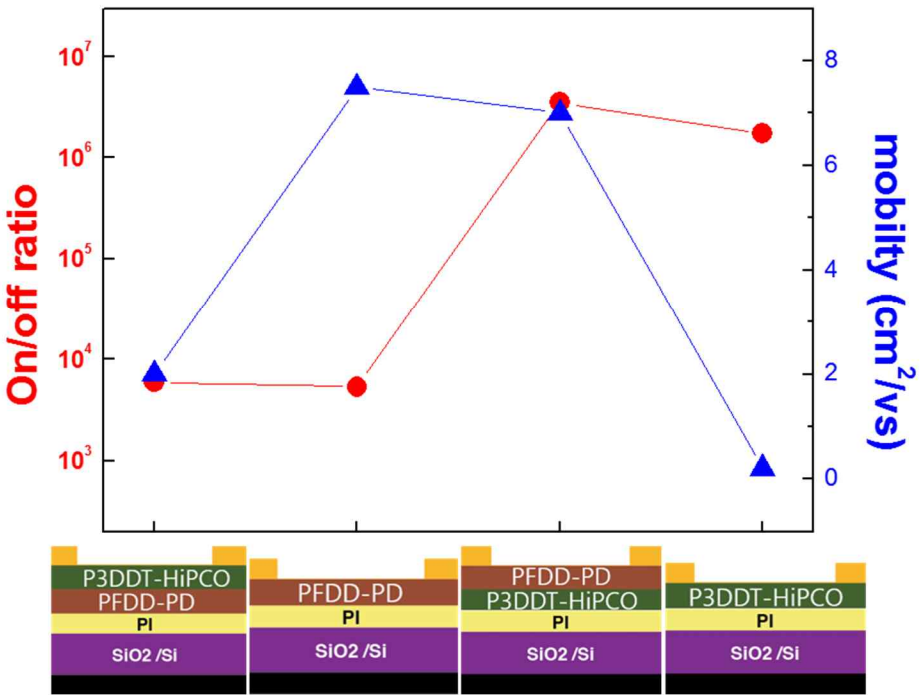

Fig. 3. 14 On/off ratio (linear region Vg=-5V) and mobility values (saturation region Vg= -20) of the four different SWNT transistors.

The PFDD-PD with good conductivity mentioned in the previous chapter was deposited in the interface with metal contacts. The contact resistance between the metal contact and semiconductor is an issue to be solved not only for SWNT transistor but also for OTFTs. To solve this problem, several method, such as chemical doping, has been used[104]. It is shown that using $FeCl_3$ and molybdenum oxide (Mo oxide) as interlayers between metal and semiconductor improves contact resistance, resulting in high performance[104, 105]. Several research group have succeeded to increase conductivity through chemical doping in Graphene and SWNTs[106, 107].

$FeCl_3$ is a strong acceptor p type dopant material. It is used as a 2 nm-layer thermally deposited a though a metal mask PFDD-PD structure. Au is sequentially deposited. Thickness was controlled using a thickness monitor. $FeCl_3$ doped PFDD-PD transistors exhibit the hole mobility of 19.8 $cm^2/ V^{-1}s^{-1}$, on/off ratio of 2.7×10^4 and off state current of 1.51×10^{-8} A as shown in Fig 3.15. Due to $FeCl_3$ doping, on current increased, but the off current too increased and the V_{TH} also shifted towards positive values.

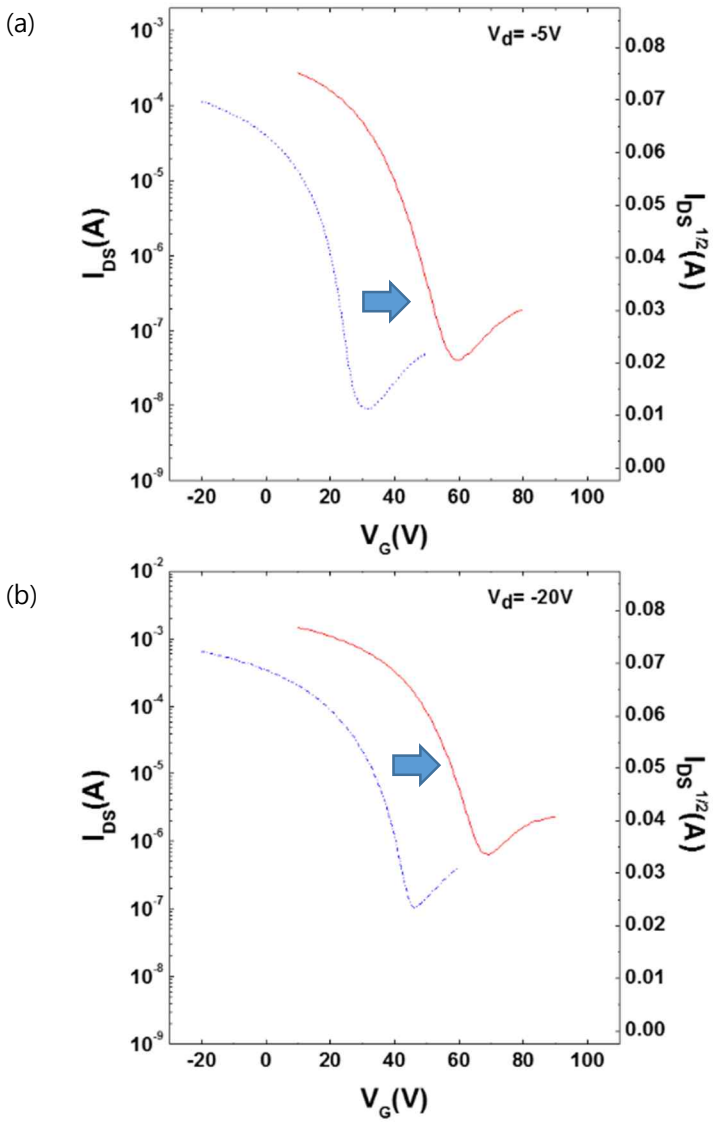

Fig. 3. 15 Linear (a) and saturation (b) transfer curves of the pristine (dot) and $FeCl_3$ doped PFDD-PD (line) transistors

The PFDD-PD / P3DDT-HiPCO / PI structure was doped with $FeCl_3$ for increasing conductivity while lowering the off current. Fig 3.16 shows the morphology of $FeCl_3$ doped PFDD-PD / P3DDT-HiPCO / PI. The thickness of the deposition $FeCl_3$ layer was in the range of 1-5nm. As the thickness of the doping layer increase to for 1 and 5 nm, the number of the white domains increase and the network become denser in the doped SWNT compared to pristine SWNT film. Figure 3.17 shows transfer characteristics of the $FeCl_3$-doped PFDD-PD/P3DDT-HiPCO/PI. 1 nm-$FeCl_3$ incorporated SWNT transistors exhibit the hole mobility of 10.8 ± 3.7 $cm^2/ V^{-1}s^{-1}$, on/off ratio of 4×10^5 and off state current of 1.7 pA. 2 nm-$FeCl_3$ incorporated SWNT transistors show the hole mobility of 116 ± 15.16 $cm^2/ V^{-1}s^{-1}$, on/off ratio of 1.67×10^5 and off state current of 7.47×10^{-11} A. 2.5 nm-$FeCl_3$ incorporated SWNT transistors show the hole mobility of 177 ± 13.2 $cm^2/ V^{-1}s^{-1}$, on/off ratio of 7.4×10^3 and off state current of 1.2×10^{-9} A. Due to the reduced depletion layer thickness and field emission occurrence in the thin Schottky barrier as the result of $FeCl_3$ doping, contact resistance was also reduced and due to the increase of charge density and decrease of the trap states in the access region though the acceptor level formation by contact doping, the access resistance decreased, too[108]. The bias stability of the transistors depends on the gate insulator. Fig 3.18 shows the result of the bias stability test. Cycle test operation was conducted at V_d = -5V and swept from 40 to -30V. The result indicate stable

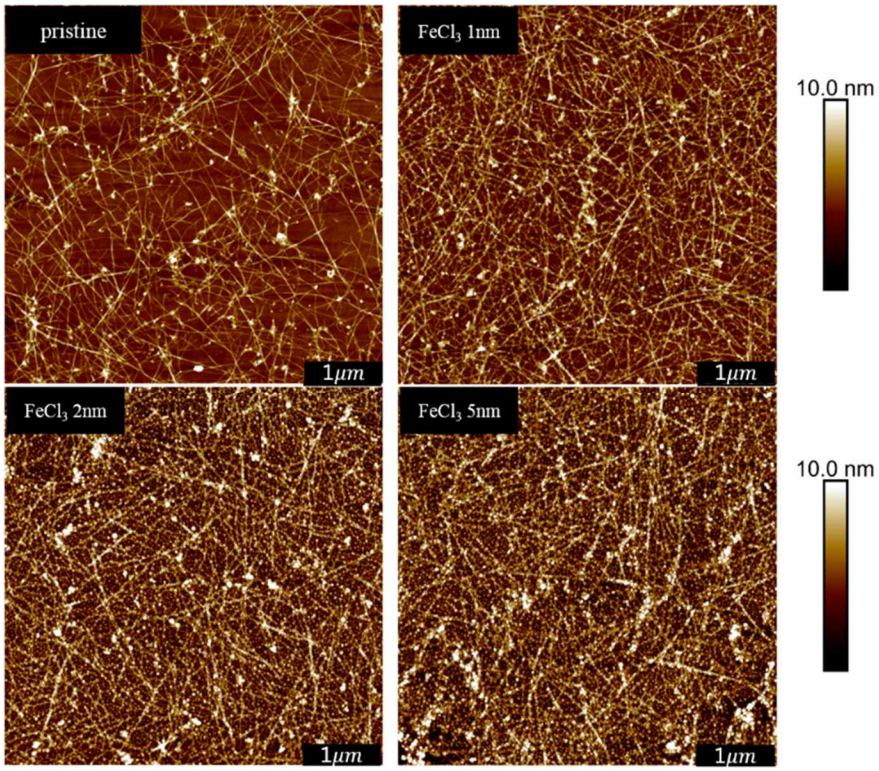

Fig. 3. 16 The morphology of $FeCl_3$ doped PFDD-PD / P3DDT-HiPCO / PI

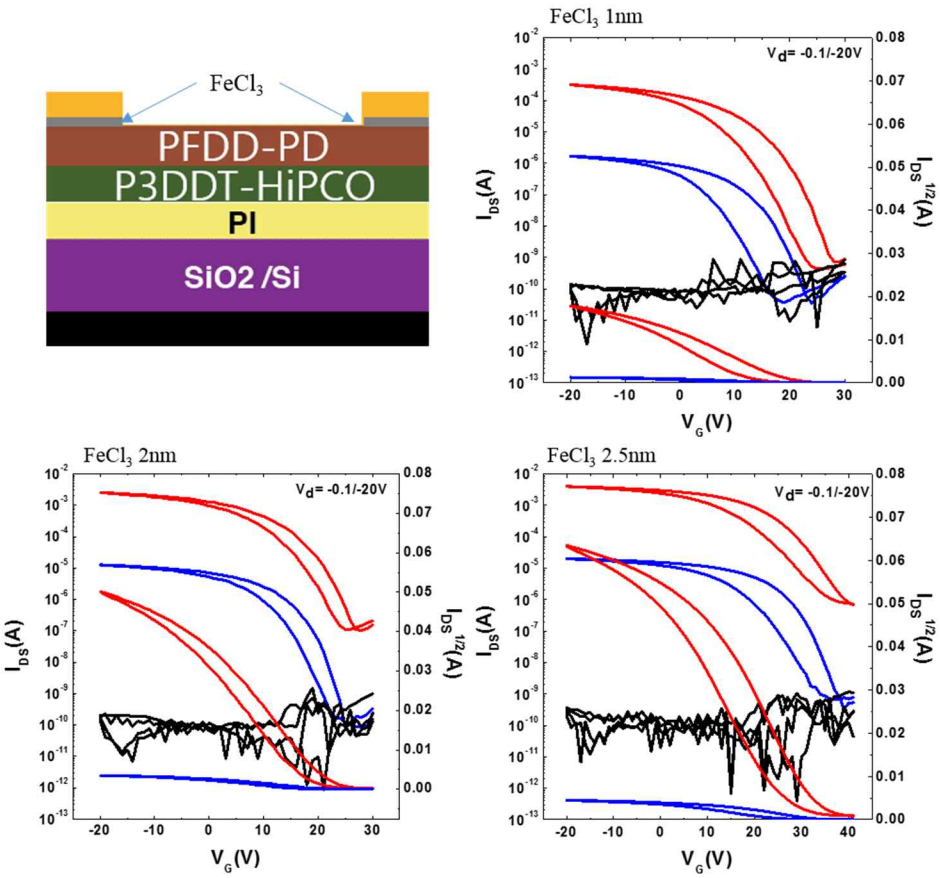

Fig. 3. 17 Transistor structure and transfer curves of $FeCl_3$ incorporated PFDD-PD/P3DDT-HiPCO/PI transistors

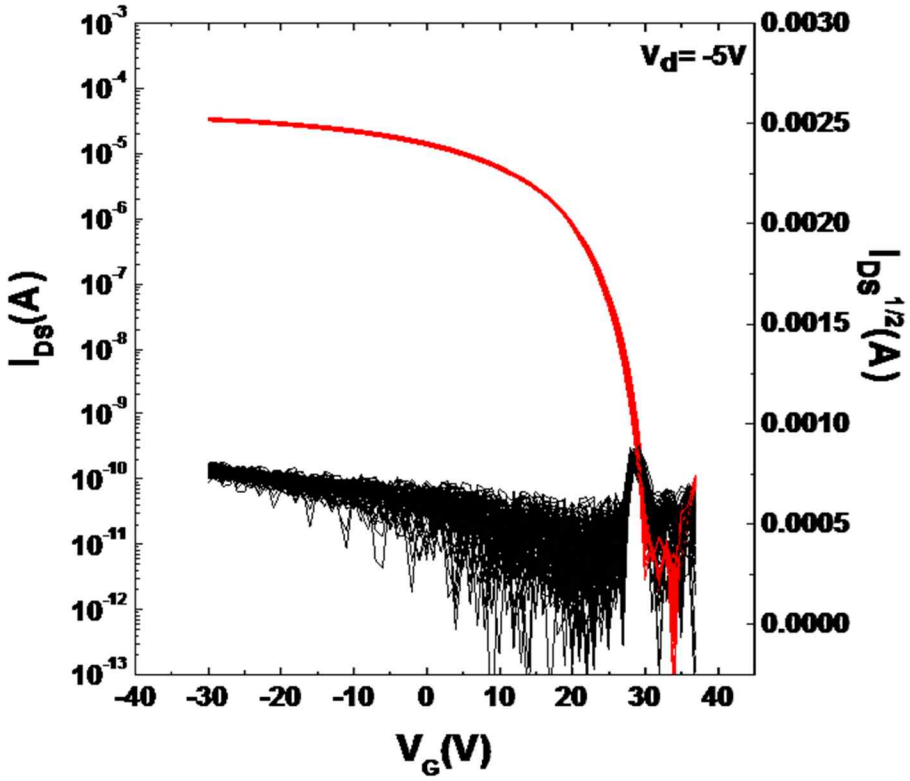

Fig. 3. 18 Cycle test (100 cycles) of 2nm $FeCl_3$ incorporated PFDD-PD/P3DDT-HiPCO/PI transistor.

Electronic properties of SWNT can be changed by doping. They were characterized by several method including UV-Vis-NIR absorption spectra, XPS, UPS Raman spectroscopy, etc.

Figure 3.19 shows the XPS spectra of $FeCl_3$ doped SWNT films deposited on 15 nm-thick gold covered glass substrate. The spectra of double layer SWNT films contain not only C 1s peaks but also additional Au peaks arising from the gold-covered substrate. The binding energy C 1s is 284 eV. Au peaks appear at 333, 355 and 641 eV. The spectra of the doped SWNT shows Fe 2p3 and Cl 2p peaks corresponding to the dopant. The binding energies of Fe 2p3 and Cl 2p are 715 and 199 eV, respectively.

Fig 3.20 show on/off ratio versus mobility for SWNT TFTs compare to other research group. A simple and effective method to simultaneously achieve high mobility and low off current in $FeCl_3$ doping hetero structured SWNT transistors.

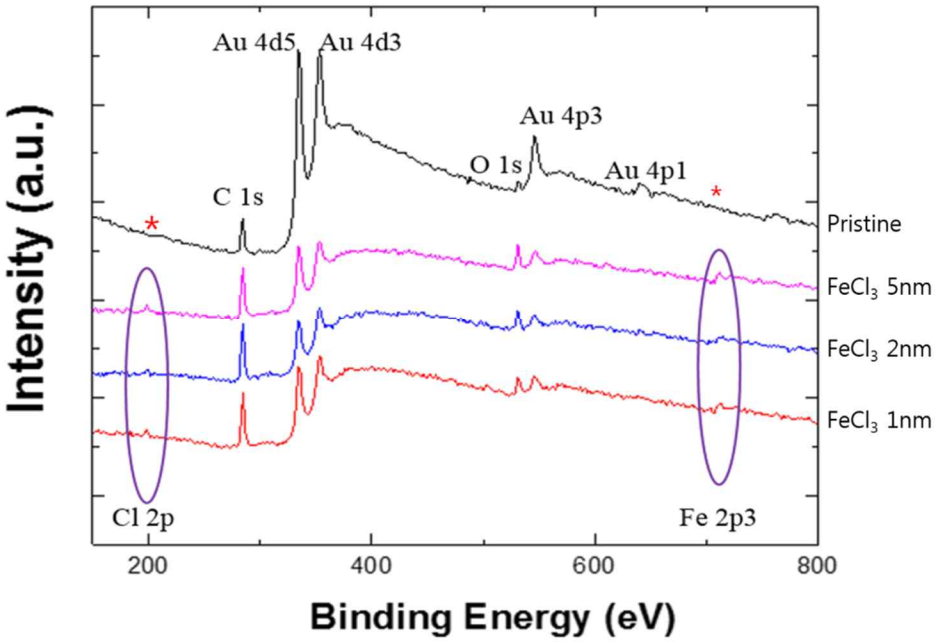

Fig. 3. 19 XPS spectra of the pristine and $FeCl_3$ interpolated PFDD-PD/P3DDT-HiPCO/PI

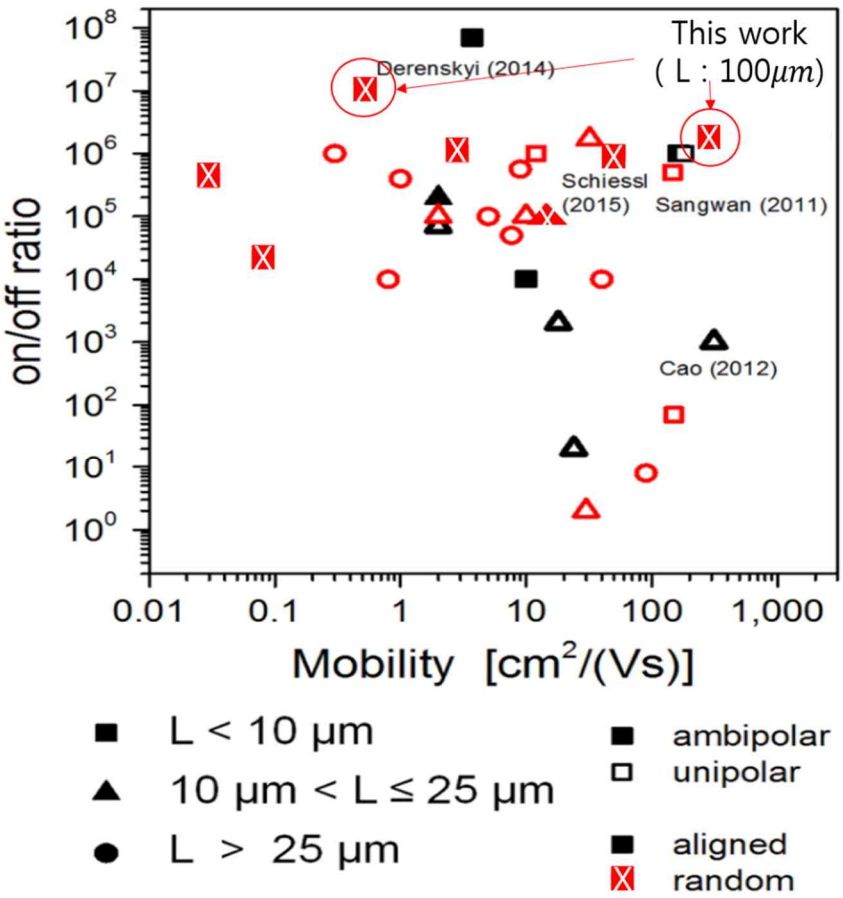

Fig. 3. 20 Comparative diagram of the research works conducted for SWNT transistors.

Summary

We fabricated s-SWNTs thin film transistors by using high purity HiPCO and PD SWNT ink. The non-patterned device shows a high leakage current, meanwhile for the patterned one the leakage was low. For the capacitance-voltage measurement, the calculated results match the existing data for this device for a thickness of PI 350nm and SiO_2/Si 100nm in a parallel contact. The P3DDT-HiPCO transistor show high on/off ratio with low mobility while the PFDD-PD transistor exhibit high mobility with high off current level. To combine the advantage of the two SWNTs, the low off state current of P3DDT-HIPCO and the high conductivity of PFDD-PD, we applied P3DDT-HiPCO as a channel layer and PFDD-PD as injection layer to obtain optimal charge injection and transport property using solution process. PFDD-PD layers serve more as charge injection layer to enhance injection of holes and electrons. Meanwhile, P3DDT-HiPCO layers act more as a charge transport layer and PI dielectric suppresses the electron transport (i.e. less ambipolar transport and lower off-current). PFDD-PD/P3DDT-HiPCO/PI transistors show the hole mobility of 6.18 ± 0.87 $cm^2/ V^{-1}s^{-1}$, on/off ratio of 1.4×10^7 and off state current of 3.4×10^{-12} A. The PFDD-PD / P3DDT-HiPCO / PI structure was doped with $FeCl_3$ for increasing conductivity while lowering the off current. . 2 nm-$FeCl_3$ incorporated SWNT transistors show the hole mobility of 116 ± 15.16 $cm^2/ V^{-1}s^{-1}$, on/off ratio of 1.67×10^5 and off state current of 7.47×10^{-11} A. As the result of $FeCl_3$ doping, the depletion layer thickness was reduced

and field emission occurrence in the thin Schottky barrier, contact resistance was also reduced and due to the increase of charge density and decrease of the trap states in the access region though the acceptor level formation by contact doping, the access resistance decreased, too.

We believed that it is attributed to two interfaces; top doped-SWNT /electrodes of charge injection properties and bottom SWNT/dielectrics of charge accumulation properties.

Chapter 4 Conclusion

A conjugated polymers were used to sort SWNTs form HiPCO and PD. We have demonstrate the selection of s-SWNTs in SWNTs grown by HiPCO for P3DDT and PD for PFDD. The UV-vis-NIR absorption spectra of P3DDT-HiPCO show the intensity of the peaks s-SWNTs increases in the range between 1000 nm and 1500 nm. The purity of s-SWNTs in P3DDT-HiPCO sample is estimated over 99% based on the UV-vis-NIR absorption spectra, Raman spectroscopy and electrical parameters. UV-vis-NIR absorption spectra display the reduction of the polymer peaks under 400 nm (PFDD) for PFDD-PD. Raman spectra illustrates PFDD-PD contains a small amount of metallic SWNTs. The purity of PFDD-PD is evaluated by using comparison of the absorption peak ratio (98-99%). AFM morphology exhibits that the both s-SWNTs networks form well-percolated morphology.

We fabricated s-SWNTs thin film transistors by using high purity HiPCO and PD SWNT ink. The non-patterned device shows a high leakage current, meanwhile for the patterned one the leakage was low. The P3DDT-HiPCO transistor show high on/off ratio with low mobility while the PFDD-PD transistor exhibit high mobility with high off current level. To combine the advantage of the two SWNTs, the low off state current of P3DDT-HIPCO and the high conductivity of PFDD-PD, we applied P3DDT-HiPCO as a channel layer and PFDD-PD as injection layer to obtain optimal charge injection and transport property using solution process. PFDD-PD layers serve more as charge injection layer to enhance injection of holes and electrons. Meanwhile, P3DDT-HiPCO layers act more as a

charge transport layer and PI dielectric suppresses the electron transport (i.e. less ambipolar transport and lower off-current). PFDD-PD/P3DDT-HiPCO/PI transistors show the hole mobility of 6.18±0.87 $cm^2/ V^{-1}s^{-1}$, on/off ratio of 1.4×10^7 and off state current of 3.4×10^{-12} A. The PFDD-PD / P3DDT-HiPCO / PI structure was doped with $FeCl_3$ for increasing conductivity while lowering the off current. 2 nm-$FeCl_3$ incorporated SWNT transistors show the hole mobility of 116±15.16 $cm^2/ V^{-1}s^{-1}$, on/off ratio of 1.67×10^5 and off state current of 7.47×10^{-11} A. As the result of $FeCl_3$ doping, the depletion layer thickness was reduced and field emission occurrence in the thin Schottky barrier, contact resistance was also reduced and due to the increase of charge density and decrease of the trap states in the access region though the acceptor level formation by contact doping, the access resistance decreased, too. A simple and effective method to simultaneously achieve high mobility and low off current in $FeCl_3$ doping hetero structured SWNT transistors.

Bibliography

[1] S. Jung, S. Lee, M. Song, D.G. Kim, D.S. You, J.K. Kim, C.S. Kim, T.M. Kim, K.H. Kim, J.J. Kim, Extremely flexible transparent conducting electrodes for organic devices, Advanced Energy Materials, 4 (2014).
[2] J.-D. You, S.-R. Tseng, H.-F. Meng, F.-W. Yen, I.-F. Lin, S.-F. Horng, All-solution-processed blue small molecular organic light-emitting diodes with multilayer device structure, Organic Electronics, 10 (2009) 1610-1614.
[3] H. Sirringhaus, 25th Anniversary Article: Organic field-effect transistors: the path beyond amorphous silicon, Advanced materials, 26 (2014) 1319-1335.
[4] H.P. Gelinck G, Nomoto K and Anthopoulos T D. , Organic transistors in optical displays and microelectronic applications, Adv. Mater, 22 (2010) 3778–3798.
[5] P.K. Weimer, The TFT a new thin-film transistor, Proceedings of the IRE, 50 (1962) 1462-1469.
[6] P. Le Comber, W. Spear, A. Ghaith, Amorphous-silicon field-effect device and possible application, Electronics Letters, 15 (1979) 179-181.
[7] K. Kudo, M. Yamashina, T. Moriizumi, Field effect measurement of organic dye films, Japanese Journal of Applied Physics, 23 (1984) 130.
[8] Y. Taur, T.H. Ning, Fundamentals of modern VLSI devices, Cambridge university press2013.
[9] K. Nomura, H. Ohta, A. Takagi, T. Kamiya, M. Hirano, H. Hosono, Room-temperature fabrication of transparent flexible thin-film transistors using amorphous oxide semiconductors, Nature, 432 (2004) 488-492.
[10] J. Zaumseil, H. Sirringhaus, Electron and ambipolar transport in organic field-effect transistors, Chemical reviews, 107 (2007) 1296-1323.
[11] M. Kano, T. Minari, K. Tsukagoshi, H. Maeda, Control of device parameters by active layer thickness in organic field-effect transistors, Applied Physics Letters, 98 (2011) 36.
[12] H. Sirringhaus, R. Friend, X. Li, S. Moratti, A. Holmes, N. Feeder, Bis (dithienothiophene) organic field-effect transistors with a high ON/OFF ratio, Applied physics letters, 71 (1997) 3871-3873.
[13] P. Cosseddu, A. Bonfiglio, A comparison between bottom contact and top contact all organic field effect transistors assembled by soft lithography, Thin Solid Films, 515 (2007) 7551-7555.
[14] T.-J. Ha, D. Sparrowe, A. Dodabalapur, Device architectures for improved amorphous polymer semiconductor thin-film transistors, Organic Electronics, 12 (2011) 1846-1851.
[15] B. Stannowski, Silicon-based thin-film transistors with a high stability, 2002.
[16] M. Powell, C. Van Berkel, A. Franklin, S. Deane, W. Milne, Defect pool in amorphous-silicon thin-film transistors, Physical Review B, 45 (1992) 4160.
[17] L. Zhang, J. Li, X. Zhang, X. Jiang, Z. Zhang, High performance ZnO-thin-film transistor with Ta 2 O 5 dielectrics fabricated at room temperature, Applied

Physics Letters, 95 (2009) 072112.
[18] J.-S. Park, J.K. Jeong, H.-J. Chung, Y.-G. Mo, H.D. Kim, Electronic transport properties of amorphous indium-gallium-zinc oxide semiconductor upon exposure to water, Applied Physics Letters, 92 (2008) 072104.
[19] J.Y. Choi, S.Y. Lee, Comprehensive review on the development of high mobility in oxide thin film transistors, Journal of the Korean Physical Society, 71 (2017) 516-527.
[20] D. Gundlach, L. Zhou, J. Nichols, T. Jackson, P. Necliudov, M. Shur, An experimental study of contact effects in organic thin film transistors, Journal of Applied Physics, 100 (2006) 024509.
[21] V. Podzorov, 2.1 Charge Carrier Transport in Single-Crystal Organic Field-Effect Transistors, Organic Field-Effect Transistors, (2007) 27.
[22] R.D. McCullough, R.D. Lowe, M. Jayaraman, D.L. Anderson, Design, synthesis, and control of conducting polymer architectures: structurally homogeneous poly (3-alkylthiophenes), The Journal of Organic Chemistry, 58 (1993) 904-912.
[23] K. Tanaka, H. Arai, S. Kohda, Characteristics of offset-structure polycrystalline-silicon thin-film transistors, IEEE electron device letters, 9 (1988) 23-25.
[24] D.X. Long, E.-Y. Choi, Y.-Y. Noh, High performance and stable naphthalene diimide based n-channel organic field-effect transistors by polyethylenimine doping, Dyes and Pigments, 142 (2017) 323-329.
[25] S.-K. Kim, B. Yang, Y. Ma, J.-H. Lee, J.-W. Park, Exceedingly efficient deep-blue electroluminescence from new anthracenes obtained using rational molecular design, Journal of Materials Chemistry, 18 (2008) 3376-3384.
[26] A. Facchetti, J. Letizia, M.-H. Yoon, M. Mushrush, H.E. Katz, T.J. Marks, Synthesis and Characterization of Diperfluorooctyl-Substituted Phenylene− Thiophene Oligomers as n-Type Semiconductors. Molecular Structure− Film Microstructure− Mobility Relationships, Organic Field-Effect Transistors, and Transistor Nonvolatile Memory Elements, Chemistry of materials, 16 (2004) 4715-4727.
[27] S. Yoo, Y.H. Kim, J.-W. Ka, Y.S. Kim, M.H. Yi, K.-S. Jang, Polyimide/polyvinyl alcohol bilayer gate insulator for low-voltage organic thin-film transistors, Organic Electronics, 23 (2015) 213-218.
[28] Y. Yuan, G. Giri, A.L. Ayzner, A.P. Zoombelt, S.C. Mannsfeld, J. Chen, D. Nordlund, M.F. Toney, J. Huang, Z. Bao, Ultra-high mobility transparent organic thin film transistors grown by an off-centre spin-coating method, Nature communications, 5 (2014) 3005.
[29] S.J. Tans, A.R. Verschueren, C. Dekker, Room-temperature transistor based on a single carbon nanotube, Nature, 393 (1998) 49-52.
[30] A.D. Franklin, M. Luisier, S.-J. Han, G. Tulevski, C.M. Breslin, L. Gignac, M.S. Lundstrom, W. Haensch, Sub-10 nm carbon nanotube transistor, Nano letters, 12 (2012) 758-762.
[31] C. Kocabas, N. Pimparkar, O. Yesilyurt, S. Kang, M.A. Alam, Rogers, JA,

Experimental and theoretical studies of transport through large scale, partially aligned arrays of single-walled carbon nanotubes in thin film type transistors, Nano letters, 7 (2007) 1195-1202.
[32] B. Kumar, B.K. Kaushik, Y.S. Negi, Organic thin film transistors: structures, models, materials, fabrication, and applications: a review, Polymer Reviews, 54 (2014) 33-111.
[33] J. Ding, Z. Li, J. Lefebvre, F. Cheng, G. Dubey, S. Zou, P. Finnie, A. Hrdina, L. Scoles, G.P. Lopinski, Enrichment of large-diameter semiconducting SWCNTs by polyfluorene extraction for high network density thin film transistors, Nanoscale, 6 (2014) supplementary information.
[34] A. Chortos, I. Pochorovski, P. Lin, G. Pitner, X. Yan, T.Z. Gao, J.W. To, T. Lei, J.W. Will, H.-S.P. Wong, Universal Selective Dispersion of Semiconducting Carbon Nanotubes from Commercial Sources Using a Supramolecular Polymer, ACS nano, (2017).
[35] J. Zaumseil, Single-walled carbon nanotube networks for flexible and printed electronics, Semiconductor Science and Technology, 30 (2015) 074001.
[36] Y. Miyata, K. Shiozawa, Y. Asada, Y. Ohno, R. Kitaura, T. Mizutani, H. Shinohara, Length-sorted semiconducting carbon nanotubes for high-mobility thin film transistors, Nano Research, 4 (2011) 963-970.
[37] W. Gomulya, G.D. Costanzo, E.J.F. de Carvalho, S.Z. Bisri, V. Derenskyi, M. Fritsch, N. Fröhlich, S. Allard, P. Gordiichuk, A. Herrmann, Semiconducting Single-Walled Carbon Nanotubes on Demand by Polymer Wrapping, Advanced Materials, 25 (2013) 2948-2956.
[38] H.W. Lee, Y. Yoon, S. Park, J.H. Oh, S. Hong, L.S. Liyanage, H. Wang, S. Morishita, N. Patil, Y.J. Park, Selective dispersion of high purity semiconducting single-walled carbon nanotubes with regioregular poly (3-alkylthiophene) s, Nature communications, 2 (2011) 541.
[39] S.P. Schießl, N. Fröhlich, M. Held, F. Gannott, M. Schweiger, M. Forster, U. Scherf, J. Zaumseil, Polymer-sorted semiconducting carbon nanotube networks for high-performance ambipolar field-effect transistors, ACS applied materials & interfaces, 7 (2014) 682-689.
[40] N. Rouhi, D. Jain, K. Zand, P.J. Burke, Fundamental Limits on the Mobility of Nanotube-Based Semiconducting Inks, Advanced Materials, 23 (2011) 94-99.
[41] P.H. Lau, K. Takei, C. Wang, Y. Ju, J. Kim, Z. Yu, T. Takahashi, G. Cho, A. Javey, Fully printed, high performance carbon nanotube thin-film transistors on flexible substrates, Nano letters, 13 (2013) 3864-3869.
[42] V. Derenskyi, W. Gomulya, J.M.S. Rios, M. Fritsch, N. Fröhlich, S. Jung, S. Allard, S.Z. Bisri, P. Gordiichuk, A. Herrmann, Carbon Nanotube Network Ambipolar Field-Effect Transistors with 108 On/Off Ratio, Advanced Materials, 26 (2014) 5969-5975.
[43] N. Izard, S. Kazaoui, K. Hata, T. Okazaki, T. Saito, S. Iijima, N. Minami, Semiconductor-enriched single wall carbon nanotube networks applied to field effect transistors, Applied Physics Letters, 92 (2008) 243112.
[44] M. Engel, J.P. Small, M. Steiner, M. Freitag, A.A. Green, M.C. Hersam, P.

Avouris, Thin film nanotube transistors based on self-assembled, aligned, semiconducting carbon nanotube arrays, ACS nano, 2 (2008) 2445-2452.
[45] Q. Cao, S.-j. Han, G.S. Tulevski, Y. Zhu, D.D. Lu, W. Haensch, Arrays of single-walled carbon nanotubes with full surface coverage for high-performance electronics, Nature Nanotechnology, 8 (2013) 180-186.
[46] V.K. Sangwan, R.P. Ortiz, J.M. Alaboson, J.D. Emery, M.J. Bedzyk, L.J. Lauhon, T.J. Marks, M.C. Hersam, Fundamental performance limits of carbon nanotube thin-film transistors achieved using hybrid molecular dielectrics, Acs Nano, 6 (2012) 7480-7488.
[47] G.J. Brady, Y. Joo, M.-Y. Wu, M.J. Shea, P. Gopalan, M.S. Arnold, Polyfluorene-sorted, carbon nanotube array field-effect transistors with increased current density and high on/off ratio, ACS nano, 8 (2014) 11614-11621.
[48] J. Ding, Z. Li, J. Lefebvre, F. Cheng, G. Dubey, S. Zou, P. Finnie, A. Hrdina, L. Scoles, G.P. Lopinski, Enrichment of large-diameter semiconducting SWCNTs by polyfluorene extraction for high network density thin film transistors, Nanoscale, 6 (2014) 2328-2339.
[49] H. Wang, P. Wei, Y. Li, J. Han, H.R. Lee, B.D. Naab, N. Liu, C. Wang, E. Adijanto, B.C.-K. Tee, Tuning the threshold voltage of carbon nanotube transistors by n-type molecular doping for robust and flexible complementary circuits, Proceedings of the National Academy of Sciences, 111 (2014) 4776-4781.
[50] S.Z. Bisri, J. Gao, V. Derenskyi, W. Gomulya, I. Iezhokin, P. Gordiichuk, A. Herrmann, M.A. Loi, High Performance Ambipolar Field-Effect Transistor of Random Network Carbon Nanotubes, Advanced Materials, 24 (2012) 6147-6152.
[51] Q. Cao, S.-J. Han, G.S. Tulevski, A.D. Franklin, W. Haensch, Evaluation of field-effect mobility and contact resistance of transistors that use solution-processed single-walled carbon nanotubes, ACS nano, 6 (2012) 6471-6477.
[52] Y. Asada, Y. Miyata, Y. Ohno, R. Kitaura, T. Sugai, T. Mizutani, H. Shinohara, High-Performance Thin-Film Transistors with DNA-Assisted Solution Processing of Isolated Single-Walled Carbon Nanotubes, Advanced Materials, 22 (2010) 2698-2701.
[53] E. Snow, P. Campbell, M. Ancona, J. Novak, High-mobility carbon-nanotube thin-film transistors on a polymeric substrate, Applied Physics Letters, 86 (2005) 033105.
[54] E. Snow, J. Novak, P. Campbell, D. Park, Random networks of carbon nanotubes as an electronic material, Applied Physics Letters, 82 (2003) 2145-2147.
[55] H.-P. Boehm, A. Clauss, G. Fischer, U. Hofmann, Das adsorptionsverhalten sehr dünner kohlenstoff-folien, Zeitschrift für anorganische und allgemeine Chemie, 316 (1962) 119-127.
[56] E. Osawa, Superaromaticity, Kagaku, 25 (1970) 101.
[57] C. Biswas, Y.H. Lee, Graphene versus carbon nanotubes in electronic devices, Advanced Functional Materials, 21 (2011) 3806-3826.
[58] C. Rao, R. Voggu, A. Govindaraj, Selective generation of single-walled carbon nanotubes with metallic, semiconducting and other unique electronic properties, Nanoscale, 1 (2009) 96-105.

[59] M.S. Dresselhaus, G. Dresselhaus, P.C. Eklund, Science of fullerenes and carbon nanotubes: their properties and applications, Academic press1996.
[60] J.-Y. Park, Band structure and electron transport physics of one-dimensional SWNTs, Carbon Nanotube Electronics, Springer2009, pp. 1-42.
[61] A. Kleiner, S. Eggert, Curvature, hybridization, and STM images of carbon nanotubes, Physical Review B, 64 (2001) 113402.
[62] A. Javey, J. Kong, Carbon nanotube electronics, Springer Science & Business Media2009.
[63] C. Kane, E. Mele, R. Lee, J. Fischer, P. Petit, H. Dai, A. Thess, R. Smalley, A. Verschueren, S. Tans, Temperature-dependent resistivity of single-wall carbon nanotubes, EPL (Europhysics Letters), 41 (1998) 683.
[64] E.F. Schubert, Doping in III-V semiconductors, E. Fred Schubert2015.
[65] P. Avouris, Z. Chen, V. Perebeinos, Carbon-based electronics, Nanoscience And Technology: A Collection of Reviews from Nature Journals, World Scientific2010, pp. 174-184.
[66] P. Avouris, Z. Chen, V. Perebeinos, Carbon-based electronics, Nature nanotechnology, 2 (2007) 605-615.
[67] D.M. Hulbert, A. Anders, D.V. Dudina, J. Andersson, D. Jiang, C. Unuvar, U. Anselmi-Tamburini, E.J. Lavernia, A.K. Mukherjee, The absence of plasma in "spark plasma sintering", Journal of Applied Physics, 104 (2008) 033305.
[68] S. Iijima, Direct observation of the tetrahedral bonding in graphitized carbon black by high resolution electron microscopy, Journal of Crystal Growth, 50 (1980) 675-683.
[69] P. Nikolaev, A. Thess, A.G. Rinzler, D.T. Colbert, R.E. Smalley, Diameter doubling of single-wall nanotubes, Chemical physics letters, 266 (1997) 422-426.
[70] B.I. Yakobson, R.E. Smalley, Fullerene nanotubes: C 1,000,000 and beyond: Some unusual new molecules—long, hollow fibers with tantalizing electronic and mechanical properties—have joined diamonds and graphite in the carbon family, American Scientist, 85 (1997) 324-337.
[71] M.I. Keun Su Kim, Ali Shahverdi, Yasaman Alinejad and Gervais Soucy, Single-Walled Carbon Nanotubes Prepared by Large-Scale Induction Thermal Plasma Process: Synthesis, Characterization, and Purification, The Journal of physcal review C, 113 (2009) 4340-4348.
[72] M.S. Arnold, A.A. Green, J.F. Hulvat, S.I. Stupp, M.C. Hersam, Sorting carbon nanotubes by electronic structure using density differentiation, Nature nanotechnology, 1 (2006) 60-65.
[73] X. Tu, S. Manohar, A. Jagota, M. Zheng, DNA sequence motifs for structure-specific recognition and separation of carbon nanotubes, Nature, 460 (2009) 250-253.
[74] A. Nish, J.-Y. Hwang, J. Doig, R.J. Nicholas, Highly selective dispersion of single-walled carbon nanotubes using aromatic polymers, Nature nanotechnology, 2 (2007) 640-646.
[75] H. Liu, D. Nishide, T. Tanaka, H. Kataura, Large-scale single-chirality separation of single-wall carbon nanotubes by simple gel chromatography, Nature

communications, 2 (2011) 309.
[76] H.W. Lee, Y. Yoon, S. Park, J.H. Oh, S. Hong, L.S. Liyanage, H. Wang, S. Morishita, N. Patil, Y.J. Park, Selective dispersion of high purity semiconducting single-walled carbon nanotubes with regioregular poly (3-alkylthiophene) s, Nature communications, 2 (2011) ncomms1545.
[77] M. Dresselhaus, G. Dresselhaus, A. Jorio, A. Souza Filho, M. Pimenta, R. Saito, Single nanotube Raman spectroscopy, Accounts of Chemical Research, 35 (2002) 1070-1078.
[78] Z. Li, J. Ding, P. Finnie, J. Lefebvre, F. Cheng, C.T. Kingston, P.R. Malenfant, Raman microscopy mapping for the purity assessment of chirality enriched carbon nanotube networks in thin-film transistors, Nano Research, 8 (2015) 2179-2187.
[79] R. Saito, G. Dresselhaus, M.S. Dresselhaus, Physical properties of carbon nanotubes, World Scientific1998.
[80] M. Dresselhaus, P. Eklund, Phonons in carbon nanotubes, Advances in Physics, 49 (2000) 705-814.
[81] J. Kürti, G. Kresse, H. Kuzmany, First-principles calculations of the radial breathing mode of single-wall carbon nanotubes, Physical Review B, 58 (1998) R8869.
[82] D. Sánchez-Portal, E. Artacho, J.M. Soler, A. Rubio, P. Ordejón, Ab initio structural, elastic, and vibrational properties of carbon nanotubes, Physical Review B, 59 (1999) 12678.
[83] D. Chattopadhyay, I. Galeska, F. Papadimitrakopoulos, A route for bulk separation of semiconducting from metallic single-wall carbon nanotubes, Journal of the American Chemical Society, 125 (2003) 3370-3375.
[84] T. Lei, X. Chen, G. Pitner, H.-S.P. Wong, Z. Bao, Removable and recyclable conjugated polymers for highly selective and high-yield dispersion and release of low-cost carbon nanotubes, J. Am. Chem. Soc, 138 (2016) 802-805.
[85] I. Pochorovski, H. Wang, J.I. Feldblyum, X. Zhang, A.L. Antaris, Z. Bao, H-bonded supramolecular polymer for the selective dispersion and subsequent release of large-diameter semiconducting single-walled carbon nanotubes, Journal of the American Chemical Society, 137 (2015) 4328-4331.
[86] N. Tessler, V. Medvedev, M. Kazes, S. Kan, U. Banin, Efficient near-infrared polymer nanocrystal light-emitting diodes, Science, 295 (2002) 1506-1508.
[87] K. Sawada, T. Ohshina, T. Hizawa, H. Takao, M. Ishida, A novel fused sensor for photo-and ion-sensing, Sensors and Actuators B: Chemical, 106 (2005) 614-618.
[88] Z. Jana, Single-walled carbon nanotube networks for flexible and printed electronics, Semiconductor Science and Technology, 30 (2015) 074001.
[89] Q. Cao, J.A. Rogers, Ultrathin films of single-walled carbon nanotubes for electronics and sensors: a review of fundamental and applied aspects, Advanced Materials, 21 (2009) 29-53.
[90] C. Wang, J. Zhang, C. Zhou, Macroelectronic integrated circuits using high-performance separated carbon nanotube thin-film transistors, ACS nano, 4 (2010) 7123-7132.

[91] Z.Y. Chen Y, Hu Y, Kang L, Zhang S, Xie H, Liu D, Zhao Q, Li Q and Zhang J 2014 State of the art of single-walled carbon nanotube synthesis on surfaces Adv. Mater. 26 5898–922.
[92] M.S. Arnold, S.I. Stupp, M.C. Hersam, Enrichment of single-walled carbon nanotubes by diameter in density gradients, Nano Letters, 5 (2005) 713-718.
[93] Y. Asada, Y. Miyata, K. Shiozawa, Y. Ohno, R. Kitaura, T. Mizutani, H. Shinohara, Thin-film transistors with length-sorted DNA-wrapped single-wall carbon nanotubes, The Journal of Physical Chemistry C, 115 (2010) 270-273.
[94] A.A. Green, M.C. Hersam, Nearly Single-Chirality Single-Walled Carbon Nanotubes Produced via Orthogonal Iterative Density Gradient Ultracentrifugation, Advanced Materials, 23 (2011) 2185-2190.
[95] J. Zhang, H. Gui, B. Liu, J. Liu, C. Zhou, Comparative study of gel-based separated arcdischarge, HiPCO, and CoMoCAT carbon nanotubes for macroelectronic applications, Nano Research, 6 (2013) 906-920.
[96] J.-M. Won, H.J. Suk, D. Wee, Y.H. Kim, J.-W. Ka, J. Kim, T. Ahn, M.H. Yi, K.-S. Jang, Photo-patternable polyimide gate insulator with fluorine groups for improving performance of 2, 7-didecyl [1] benzothieno [3, 2-b][1] benzothiopene (C 10-BTBT) thin-film transistors, Organic Electronics, 14 (2013) 1777-1786.
[97] S.-H. Lee, D.-Y. Kim, Y.-Y. Noh, Improved ambipolar charge injection in organic field-effect transistors with low cost metal electrode using polymer sorted semiconducting carbon nanotubes, Organic Electronics, 46 (2017) 28-34.
[98] A. Javey, J. Guo, D.B. Farmer, Q. Wang, D. Wang, R.G. Gordon, M. Lundstrom, H. Dai, Carbon nanotube field-effect transistors with integrated ohmic contacts and high-κ gate dielectrics, Nano Letters, 4 (2004) 447-450.
[99] Y. Huang, L. Huo, S. Zhang, X. Guo, C.C. Han, Y. Li, J. Hou, Sulfonyl: a new application of electron-withdrawing substituent in highly efficient photovoltaic polymer, Chemical Communications, 47 (2011) 8904-8906.
[100] C. Yeom, K. Chen, D. Kiriya, Z. Yu, G. Cho, A. Javey, Large-Area Compliant Tactile Sensors Using Printed Carbon Nanotube Active-Matrix Backplanes, Advanced Materials, 27 (2015) 1561-1566.
[101] R. Shvartzman-Cohen, E. Nativ-Roth, E. Baskaran, Y. Levi-Kalisman, I. Szleifer, R. Yerushalmi-Rozen, Selective dispersion of single-walled carbon nanotubes in the presence of polymers: the role of molecular and colloidal length scales, Journal of the American Chemical Society, 126 (2004) 14850-14857.
[102] G. Ghibaudo, New method for the extraction of MOSFET parameters, Electronics Letters, 24 (1988) 543-545.
[103] N. Rouhi, D. Jain, P.J. Burke, High-performance semiconducting nanotube inks: Progress and prospects, ACS nano, 5 (2011) 8471-8487.
[104] Y. Chen, I. Shih, S. Xiao, Effects of FeCl 3 doping on polymer-based thin film transistors, Journal of applied physics, 96 (2004) 454-458.
[105] M. Kano, T. Minari, K. Tsukagoshi, Improvement of subthreshold current transport by contact interface modification in p-type organic field-effect transistors, Applied Physics Letters, 94 (2009) 101.
[106] W. Liu, J. Kang, K. Banerjee, Characterization of FeCl 3 intercalation doped

CVD few-layer graphene, IEEE Electron Device Letters, 37 (2016) 1246-1249.
[107] X. Liu, T. Pichler, M. Knupfer, J. Fink, H. Kataura, Electronic properties of FeCl 3-intercalated single-wall carbon nanotubes, Physical Review B, 70 (2004) 205405.
[108] T. Minari, P. Darmawan, C. Liu, Y. Li, Y. Xu, K. Tsukagoshi, Highly enhanced charge injection in thienoacene-based organic field-effect transistors with chemically doped contact, Applied Physics Letters, 100 (2012) 59.

초록

최근에 스마트폰 및 웨어러블 장치와 같은 모바일 디바이스의 급속한 확산은 유연하고 신축성 있는 디바이스 대한 요구를 증가시켰다. 신축성을 갖는 디바이스의 반도체 층은 우수한 전하 캐리어 이동성을 가지는 것은 물론 기계적 특성이 우수한 랜덤 네트워크 구조를 가져야 한다. 또한 대 면적 및 저비용 디바이스를 위해 용액 공정이 필수적이다. 단일벽 탄소나노튜브는 용액 공정이 가능하고, 필름을 형성 할 때 랜덤 네트워크 구조를 가지며, 높은 캐리어 이동성 및 우수한 기계적 특성을 나타내기 때문에 신축성 디바이스의 반도체 물질로 적합한 재료이다. 그러나, 단일벽 탄소나노튜브의 합성 과정에서 금속성 및 반도체 성질을 모두 가지므로 반도체 성질만을 분리하는 과정이 필수적이다. 이것을 분리하는 방법으로 DNA를 이용 방법, 밀도차를 이용하는 방법 등이 있지만 얻어지는 반도체성질의 순도와 수율이 낮다. 이러한 문제를 해결하려고 공액 고분자를 이용하여 분리하는 방법을 연구하였다. .

1 장에서는 트랜지스터의 역사, 동작 원리, 트랜지스터 특성, 트랜지스터의 종류와 같은 기본적인 트랜지스터 지식을 소개 할 것이다. 또한 탄소 동소체, 단일벽 탄소나노튜브의 전기 밴드 구조, 단일벽 탄소

나노튜브의 합성 방법 등의 기본 지식을 소개한다.

2 장에서는 고순도 반도체성질 단일벽 탄소나노튜브를 고분자로 감싸는 방법으로 분리하였다. 우리는 poly-9,9-di-n-octyl-fluorenyl-2,7-diyl (PFO)와 poly (3-dodecylthiophene-2, 5-diyl) (P3DDT)을 사용한 HiPCO공정으로 성장한 단일벽 탄소나노튜브(P3DDT-HiPCO)에서 반도체성 단일벽 탄소나노튜브를 분리하였고 poly (9, 9-di-n-dodecylfluorene) (PFDD)를 사용하여 PD 공정에서 성장한 단일벽 탄소나노튜브(PFDD-PD)에서 반도체성 단일벽 탄소나노튜브를 분리하였다. 분리한 반도체성 단일벽 탄소나노튜브는 자외선 가시 분광법, 라만 분광법, 원자 힘 현미경, 전계 방출 주사 전자 현미경 및 투과 전자 현미경 등을 이용하여 순도, 농도 표면을 분석. P3DDT-HiPCO에서 분리한 반도체성 단일벽 탄소나노튜브의 순도는> 99 %로 추정되며 PFDD-PD의 반도체성 단일벽 탄소나노튜브순도는 98-99 %로 추정됩니다.

3 장에서는 고순도 반도체성 단일벽 탄소나노튜브 잉크를 사용하여 트랜지스터를 제작했다. 포토 공정이 가능한 폴리이미드 물질을 사용하여 새로운 방법의 단일벽 탄소나노튜브 패터닝 공정을 개발하여 전압에서 흐르는 누설 전류를 피코 수준으로 낮추었다. 하나의 종류만의 반도체성 단일벽 탄소나노튜브를 용액공정을 이용하여 전계효과 트랜

지스터를 제작하였을 때, P3DDT-HiPCO 트랜지스터 경우는 높은 점멸비를 갖지만 이동도가 낮다. 반면 PFDD-PD는 낮은 점멸비에 높은 이동성을 보인다. 이종구조를 도입함으로써 높은 점멸비와 높은 이동도를 동시에 얻을 수 있었다. 절연체/P3DDT-HiPCO/PFDD-PD 이종구조에서 10^7의 높은 점멸비와 홀 이동도 7 cm^2/Vs을 달성했습니다. 또한 $FeCl_3$ 도판트를 이종구조 단일벽 탄소나노튜브에 적용하여 용액공정 전계효과 트랜지스터를 제작하였고 점멸비 10^6 (V_d = -5V)과 홀 이동도 100 cm^2 / Vs (V_d = -20V) 이상의 고성능을 보였다.